AD NUMBER

AD867243

NEW LIMITATION CHANGE

TO

Approved for public release, distribution unlimited

FROM

Distribution authorized to DoD only; Administrative/Operational Use; DEC 1969. Other requests shall be referred to Defense Advanced Research Projects Agency, 1400 Wilson Blvd., Arlington, VA 22209-2308.

AUTHORITY

ARPA ltr, 13 Jul 1970

Institute for Defense Analyses

Determination of Winds and other Atmospheric parameters by Satellite – Etc. (U)

Grobecker,Alan J.

DAHC15-67-C-0011

IDA/HQ-69-9962

Dec.1969   S-341-Vol-3

STUDY S-341

DETERMINATION OF WINDS AND OTHER ATMOSPHERIC PARAMETERS BY SATELLITE TECHNIQUES

in four volumes

VOLUME III: Techniques for Determining Winds and Other Atmospheric Parameters

Alan J. Grobecker
Henry Hidalgo
John A. Laurmann

December 1969

IDA

INSTITUTE FOR DEFENSE ANALYSES
SCIENCE AND TECHNOLOGY DIVISION
400 Army-Navy Drive, Arlington, Virginia 22202

READER'S REFERENCE

This report is Volume III of IDA Study S-341 "Determination of Winds and Other Atmospheric Parameters by Satellite Techniques."

The volumes describing the study are the following:

ABSTRACT

Techniques which have potential use for explicit determination
of atmospheric parameters by observations from satellites are eval-
uated for inherent accuracy of measurement. The discussion describes
the instrumental techniques for measuring densities of air and its
constituents by atmospheric emission, atmospheric absorption of solar
radiation, deceleration of low altitude satellites, occultation satel-
lite to satellite microwave transmissions, backscatter by dust of
pulsed laser signals and wind by the motion of clouds determined by
time sequenced pictures from satellites and the displacement of bal-
loons tracked in position by satellites. The principle of operation,
uncertainty of measurement, coverage in volume, and status of develop-
ment of each of techniques considered are detailed.

In addition to the methods for explicit measurement of atmospheric
parameters, an implicit method of determining winds at all altitudes
by machine computation of the equations of continuity of momentum,
mass and energy, using satellite derived inputs of densities, tempera-
ture and heating, is suggested. Experience in application of the
method for purposes of numerical prediction of weather for more than
a day ahead is described. Special problems in extrapolating the ex-
perience in tropospheric simulation for the determination of winds
of the upper atmosphere, for which input data are potentially avail-
able by measurements from satellites, are named. Estimates are given
indicating that the upper atmosphere simulation is within the expected
capacity of next-generation computers such as ILLIAC IV.

CONTENTS

FIGURES

TABLES

INTRODUCTION

The primary objective of the Institute for Defense Analyses Study S-341, "Determination of Winds and Other Atmospheric Parameters from Satellites," is the review of various instrumentation techniques operated from satellites and the evaluation of their potential. This report undertakes to evaluate the most promising of these techniques for the determination of winds and other atmospheric parameters.

The nature of the atmosphere, which is the medium to be examined by the measurement techniques, is complic. .1. Its complexities and variabilities have been described in "Physics of the Atmosphere," Volume IV of this study. Requirements for knowledge of atmospheric parameters to which a number of Department of Defense potential missions are sensitive are described in "Potential Needs for the Determination of Atmospheric Parameters," Volume II of the study. These requirements of the potential missions are the standards for performance of the instrumentation schemes described herein.

Techniques which have potential use for explicit determination of atmospheric parameters from satellites are evaluated for inherent accuracy of measurement in this volume. In particular, the discussion describes the instrumentation techniques and the characteristic uncertainties of measurement for the determination of atmospheric parameters by inversion of atmospheric emission, by the atmospheric absorption of solar radiation, by the deceleration of low-altitude satellites, by the occultation of satellite-to-satellite transmissions, by the measurement of backscatter by dust of pulsed laser signals, by the motion of clouds determined from TV-type (APT) pictures from satellites, and by the motion of balloons tracked in position by satellites.

1

In summary, the ways to determine wind and density from satellites which have been considered are outlined in Table 1.

Of the several techniques, two ways of determining density, by measurement of atmospheric emissions and of the atmospheric absorption of solar radiation, and one way of determining wind, by the computational simulation of the atmosphere with density, temperature and heating inputs derived by satellite measurement, are of major importance to the success of military objectives and are unlikely to be accomplished by civil agencies. Two additional ways of determining density, microwave satellite-to-satellite occultation and satellite drag, are important to meet the needs of military objectives, but not as crucially. They represent significant backup potential for military needs. The first may not and the second probably will not be developed by civil agencies. One other way of determining density, laser backscatter, is still in an immature research phase which merits encouragement. Two other ways of determining wind include the determination from pictures of clouds, characterized by limited altitude coverage and marginal accuracy, and the determination from the motion of satellite tracked balloons, which have particular military vulnerability. Both of the latter ways may perhaps be adequately developed by civil agencies.

Also shown in Table 1 are the ranges of altitude and the uncertainty of determination for which the way may be effective, and the military mission for which knowledge of the atmospheric parameter is necessary. For each such military mission, the tolerable fractional uncertainty of the atmospheric parameter is also shown to be a number equal or greater than the uncertainty of determination.

2

TABLE 1.   WAYS OF DETERMINING WINDS AND DENSITY FROM SATELLITES

DETERMINATION OF DENSITIES					
TECHNIQUE	PARAMETER	RANGE OF ALTITUDES, km	DETERMINATION UNCERTAINTY, %	NEED (APPLICATION/TOLERABLE UNCERTAINTY)	
ATMOSPHERIC EMISSION	DENSITY	0-60	1	WEATHER PREDICTION BALL. MISS. TARGET	10% 10%
SOLAR ABSORPTION	DENSITY	90-300	10	SAT. ORBIT PRED.	10%
SATELLITE DRAG BY ACCELEROMETER	DENSITY	100-300	10	SAT. ORBIT PRED.	10%
MICROWAVE OCCULTATION	DENSITY, AIR	4-20	0.1*	WEATHER PREDICTION	10%
	DENSITY, WATER		1		
LASER BACKSCATTER	DENSITY, O_2 DENSITY, DUST	0-30	15-100 15-100	WEATHER PREDICTION	10%
	DENSITY, WATER		5		
DETERMINATION OF WINDS					
COMPUTATIONAL SIMULATION, WITH DENSITY, TEMPERA- TURE, HEATING, INPUTS	WIND	ALL ALTITUDES	25-100	... iHER PREDICTION BALL. MISS. TARGET BMD DISCRIMINATION	10% 30% 40%
PICTURES OF CLOUDS	WIND	1-18	25	WEATHER PREDICTION	10%
SATELLITE-TRACKED BALLOON	WIND	1 AND 10-15	3-25	WEATHER PREDICTION	10%

*BASED SOLELY ON THEORETICAL HYPOTHESES

Table 2 lists the characteristics of satellite vehicles and the orbits required for the application of the several measurement techniques. Comparisons, rough and tentative, with existing satellite systems are made in Table 2. Confirmation of the comparisons, and further elaboration of system details, together with cost effectiveness comparisons with competitive systems, are desirable objectives of a further study.

Table 3 summarizes the results of this review of measurement capability, expressed as a practical minimum fractional uncertainty of the capability for determining atmospheric parameters. Also shown for comparison is the tolerable maximum in the same altitude region required for the missions discussed in Volume II.

3

TABLE 2. TENTATIVE SATELLITE SYSTEMS TO DETERMINE ATMOSPHERIC PARAMETERS

MEASUREMENT TECHNIQUE*	ATMOSPHERIC PARAMETER	ALTITUDE RANGE (KM)	SATELLITE VEHICLE ORBIT	COMPARABLE SYSTEMS	REQUIRED SUPPLEMENT TO SATELLITES
ATMOSPHERIC EMISSION	TEMPERATURE, PRESSURE (TOTAL AND WATER) DENSITY (TOTAL O_3, O_2, AND N_2) ENERGY (SOLAR INPUT)	0-60	POLAR (900 KM) AND GEOSYNCHRONOUS	NIMBUS WITH POINTING CONTROLS (8 SATELLITES, MTBF LIMITED) ATS EXPANDED (4 SATELLITES, MTBF LIMITED)	EACH SYSTEM REQUIRES GROUND EQUIPMENT PECULIAR TO MISSION
SOLAR ABSORPTION AND MONITORING	TEMPERATURE, PRESSURE, DENSITY (TOTAL O_3, O_2, AND H_2) ENERGY (SOLAR INPUT)	90-300	LOW INCLINATION (600 KM)	COMBINATION OF SOLRAD, VELA (18 SATELLITES, MTBF LIMITED)	
MICROWAVE SATELLITE-TO-SATELLITE OCCULTATION	PRESSURE (TOTAL AND WATER) DENSITY (TOTAL AND WATER)	4-20	POLAR (900 KM)	B. LUSIGNAN PROPOSALS (21 SATELLITES, MTBF LIMITED)	
SATELLITE DRAG BY ACCELEROMETER	DENSITY	100-300	POLAR (150-200 KM)	OV 1-15, OV 1-16 AND DRAG-FREE SATELLITE (DRAG DECAY OR PROPULSION LIMITED)	
TV PICTURE OF CLOUDS	WIND	1-18	GEOSYNCHRONOUS	ATS (4 SATELLITES, MTBF LIMITED)	
SATELLITE-TRACKED BALLOONS	WIND	1 AND 10-15	POLAR (900 KM)	NIMBUS-D	

*PROVIDES DATA NEEDED FOR COMPUTER SIMULATION OF WIND.

4

TABLE 3. FRACTIONAL UNCERTAINTIES OF MEASUREMENT TECHNIQUES, COMPARED WITH
NEEDS FOR APPLICATIONS AND VARIABILITY OF CLIMATIC AVERAGES

FRACTIONAL UNCERTAINTIES OF ATMOSPHERIC PARAMETERS

MEASUREMENT OR APPLICATION	ALTITUDE RANGE (KM)	T	P	P_w	n_{TOT}	$n(O_3)$	$n(O_2)$	$n(O)$	$n(N_2)$	N_e	V	N	D	$q(\lambda)$	σ
MEASUREMENT TECHNIQUES															
ATMOSPHERIC EMISSION	0–60 KM	$\dfrac{(10)^{-2}}{(10)^{-1}}$	$\dfrac{(10)^{-2}}{3(10)^{-1}}$	$\dfrac{3(10)^{-1}}{10^0}$	$\dfrac{(10)^{-2}}{3(10)^0}$	✓	$\dfrac{(10)^{-2}}{3(10)^{-1}}$		$\dfrac{(10)^{-2}}{3(10)^{-1}}$					✓	
ATMOSPHERIC ABSORPTION	100–300 KM	✓	✓		$\dfrac{(10)^{-1}}{7(10)^0}$		$\dfrac{(10)^1}{10}$	$\dfrac{(10)^0}{(?)}$	$\dfrac{(10)^{-1}}{7(10)^0}$					✓	
SATELLITE DECELERATION	(125–200 KM)			$\dfrac{(10)^{-2}}{10^0}$	$\dfrac{3(10)^0}{3(10)^0}$										
MICROWAVE SAT TO SAT OCCULT	(25–70 KM)			$\dfrac{10^{-1}}{10^0}$	$\dfrac{(10)^{-3}}{2(10)^{-1}}$										
LASER BACKSCATTER BY DUST, O_2, H_2O	(14–30 KM)			$\dfrac{10^{-1}}{10^0}$	$\dfrac{(10)^{-1}}{2(10)^{-1}}$										
TV PIX OF CLOUDS	(1–18 KM)					✓									
APPLICATION															
WEATHER PREDICTION	(0–20 KM)	$\dfrac{(10)^{-2}}{2(10)^{-1}}$	$\dfrac{(10)^{-1}}{2(10)^{-1}}$	$\dfrac{(10)^{-1}}{10^0}$	$\dfrac{(10)^{-1}}{2(10)^{-1}}$						$\dfrac{(10)^{-1}}{10^0}$ HORIZ $\dfrac{(10)^0}{(10)^0}$ VERT				
RADIO COMMUNICATION	(7–320 KM)	$\dfrac{(10)^{-2}}{(10)^{-1}}$		$\dfrac{(10)^{-2}}{(10)^0}$	$\dfrac{(10)^{-2}}{(10)^0}$					$\dfrac{(10)^{-2}}{(10)^0}$	$\dfrac{(10)^{-3}}{(10)^0}$	✓	✓	✓	
BALLISTIC MISSILE TARGETING	(0–50 KM)		✓		$\dfrac{10^{-3}}{3(10)^{-1}}$						$\dfrac{3(10)^{-1}}{(10)^0}$			✓	
SATELLITE ORBIT PREDICTION	(125–200 KM)	✓	✓		$\dfrac{5(10)^{-2}}{3(10)^0}$						$\dfrac{(10)^{-1}}{(10)^0}$			✓	
DISCRIMINATION IN BMD	(50–130 KM)	$\dfrac{2(10)^0}{3(10)^{-1}}$			$\dfrac{(10)^0}{4(10)^{-1}}$					$\dfrac{4(10)^{-1}}{4(10)^{-1}}$				✓	

NOTE FIGURES WITH RESPECT TO APPLICATIONS ARE THE TOLERABLE FRACTIONAL UNCERTAINTIES EXPRESSED IN THE NUMERATORS.
UNCERTAINTIES OF THE CLIMATIC AVERAGES IN THE DENOMINATORS. FIGURES WITH RESPECT TO MEASUREMENT TECHNIQUES
ARE THE INSTRUMENTAL UNCERTAINTIES IN THE NUMERATORS, UNCERTAINTIES OF THE CLIMATIC AVERAGES IN THE
DENOMINATORS. CHECKS INDICATE THAT THE PARAMETER IS SIGNIFICANT OR MEASURABLE BUT THE RELEVANT UNCERTAINTIES
HAVE NOT BEEN EVALUATED.

The most significant conclusion drawn from the review of instrumentation techniques is that satellite-borne instrumentation may remotely measure all atmospheric parameters considered, with accuracy and coverage adequate to meet the needs of the important defense missions considered, with the exception of two parameters: winds, because of inadequacy in coverage and in accuracy; and electron density, because of inadequacy in coverage.

In addition to the explicit measurement of atmospheric winds, this report suggests that implicit determination of winds may be made by computational simulation for which the input data are the explicit measurements by satellite of atmospheric parameters other than winds. Justification for the suggestion is not, however, quantitatively shown.

6

INVERSION OF ATMOSPHERIC EMISSION

By inversion of satellite radiometer measurements of infrared emission, in the wing of a collision broadened spectral line, effective height profiles of temperature, density and pressure may be determined.

A characterization of the technique is given in Fig. 1, summarizing discussions given in the following descriptions, in turn, of the basic theory, temperature and height uncertainties, determination of ozone density by ultraviolet emission, determination of H_2O and O_2 density by microwave emission, and systems considerations.

PRINCIPLE

The principle of the technique was initially suggested by King (1958), elaborated by Kaplan (1959), and further described by Wark and Fleming (1966).

At a single frequency v, the radiative transfer equation is

$$d I(v, \theta) = \left[-I(v, \theta) - B(v, T(z)) \right] k(v) \rho(z) \sec\theta \, dz \qquad (1.1)$$

where $I(v,\theta)$ is the radiance at v in the direction θ from the local vertical, $k(v)$ is the mass absorption coefficient of the absorbing gas, $\rho(z)$ is the density of the gas, $B(v,T)$ is the Planck radiance at v and the temperature T, and z is the height in the local vertical.

Assuming that the instrument observes in a narrow cone in the local vertical so that everywhere in the cone $\sec\theta = 1$, and transforming the variable z to pressure p by means of the hydrostatic equation

$$\rho dz = -\frac{c}{g} \, dp \qquad (1.2)$$

7

PRINCIPLE OF OPERATION

- EMISSION = f(T, ρ, K, X) OF EMITTING GAS
- MASS ABSORPTION COEFFICIENT (K) KNOWN IN WINGS OF LINE (I.E., 15μ, CO_2)
- PATH LENGTH (X) KNOWN BY GEOMETRY
- TWO LINES OF CO_2 AND O_2 YIELD DENSITY (ρ) AND TEMPERATURE (T) AS FUNCTION OF ALTITUDE
- ADDITIONAL LINE OF H_2O YIELDS WATER VAPOR DENSITY

UNCERTAINTY OF MEASUREMENT

- DENSITY: 1%
- TEMPERATURE: 1%

COVERAGE IN VOLUME

- ALTITUDE: RANGE OF 0-30 KM BY NADIR OBSERVATIONS; 30-60 KM BY HORIZONTAL OBSERVATIONS
- HORIZONTAL GRID: 3-200 KM

STATUS OF DEVELOPMENT

- 15μ-LINE SENSORS OF 0-30 KM VERTICAL RANGE; 3-200 KM HORIZONTAL RESOLUTION BY NIMBUS
- DATA PROCESSING: NIMBUS
- DESIGN NOT YET OPTIMIZED

RECOMMENDATION

- INVESTIGATE FEASIBILITY OF HORIZONTAL VIEW EMISSION SATELLITE FOR T, ρ, AT 30-60 KM FOR NEEDS OF BALLISTIC WEAPON TARGETING.
- INVESTIGATE FEASIBILITY OF VERTICAL VIEW EMISSION SATELLITE FOR MEASURING 3 HR AND 300 KM AVERAGE VERTICAL EMISSION TO DETERMINE TOTAL DENSITY, TEMPERATURE AND WATER VAPOR DENSITY BY GEOSYNCHRONOUS SATELLITE FOR NEEDS OF NUMERICAL WEATHER ANALYSIS AND BALLISTIC WEAPON TARGETING IN ALTITUDE RANGE 0-30 KM. THIS MAY BE DEVELOPED ADEQUATELY BY CIVIL AGENCIES.

ATMOSPHERIC EMISSION
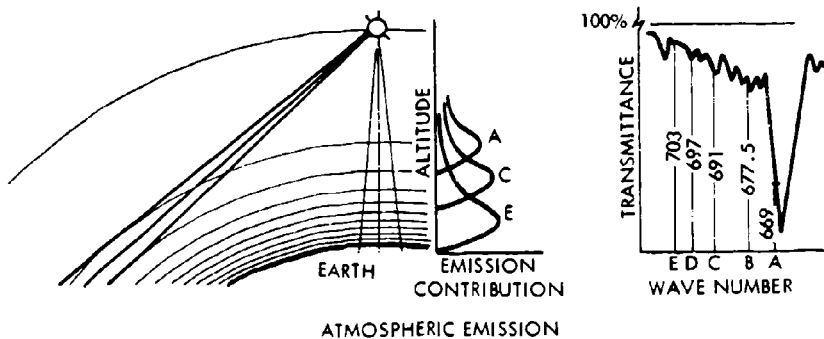
FIGURE 1. Measurement of Atmospheric Emission for Density at 0-60 km

where q is the mass mixing ratio of the absorbing gas and g is the gravitational acceleration, Eq. 1.1 may be written as

$$I(\nu,o) = \epsilon(\nu)\ B\left[\nu,T(p_o)\right] e^{-\frac{q}{g}\int_0^{p_o} k(\nu,p)dp}$$

$$+ \frac{q}{g}\int_0^{p_o} B(\nu,T(p))\ e^{-\frac{q}{g}\int_0^{p_o} k(\nu,p)dp}\ k(\nu,p)dp \qquad (1.3)$$

where $\epsilon(\nu)$ is the emissivity of the lower bound (i.e., at p_o) and the subscript denotes the lower boundary. The first term is the component of radiance arising from the surface, and the second term is that component arising from the atmosphere itself.

It is convenient to simplify by introducing the fractional transmittance

$$\tau(\nu,p) = e^{-\frac{q}{g}\int_0^p k(\nu,p)dp} \qquad (1.4)$$

of the beam between the level p and the effective top of the atmosphere, so that Eq. 1.3 becomes

$$I(\nu,o) = \epsilon(\nu)\ B(\nu,T(p_o))\tau(\nu,p_o)$$

$$-\int^{\tau(\nu,p_o)} B(\nu,T(p))\ d\tau(\nu,p) \qquad (1.5)$$

Equation 1.5 expresses radiance for a single wavelength. An instrument, however, distinguishes only finite bandwidths. The measured instrument radiance in normalized form for a spectrometer is the convolution product

$$I(\nu^*,o) = \int_{\nu_1}^{\nu_2} w(\nu^* - \nu)\, I(\nu,o)d\nu \Bigg/ \int_{\nu_1}^{\nu_2} w(\nu^* - \nu)d\nu$$

$$= \Bigg\{ \int_{\nu_1}^{\nu_2} w(\nu^* - \nu)\, B\Big[\nu,T(p_o)\Big]_\tau (\nu,p_o)d\nu \tag{1.6}$$

$$- \int_{\nu_1}^{\nu_2}\int_{o}^{p_o} w(\nu^* - \nu)\, B\Big[\nu,T(p)\Big]\frac{\partial \tau(\nu,p)}{\partial p}\, dp\, d\nu \Bigg\} \Bigg/ \int_{\nu_1}^{\nu_2} w(\nu^* - \nu)d\nu$$

where $w(\nu)$ is the spectrometer slit function and ν_1, ν_2 are its limiting frequencies.

A filter radiometer, on the other hand, involves an inner product rather than a convolution product.

Equation 1.6 is complicated. However, if the spectral interval ν_1 to ν_2 is small, then $B(\nu,T)$ varies little, is linear in the interval, and may be replaced by its value $B(\bar{\nu}, T)$ at a properly defined mean frequency $\bar{\nu}$, so that it may be factored out of the integral with respect to $\bar{\nu}$.

One may further define the mean effective transmittance and its partial derivative as

$$\tau(\nu^*, p) = \frac{\displaystyle\int_{\nu_1}^{\nu_2} w(\nu^* - \nu)\tau(\nu,p)d\nu}{\displaystyle\int_{\nu_1}^{\nu_2} w(\nu^* - \nu)d\nu} \tag{1.7a}$$

10

$$\frac{\partial \tau(\nu^*,p)}{\partial p} = \frac{\displaystyle\int_{\nu_1}^{\nu_2} w(\nu^* - \nu)\,\frac{\partial \tau(\nu,p)}{\partial p}\,d\nu}{\displaystyle\int_{\nu_1}^{\nu_2} w(\nu^* - \nu)\,d\nu} \qquad (1.7b)$$

In the spectrometers discussed the spectral intervals are narrow (5 cm^{-1} to 20 cm^{-1}) and the slit functions $w(\nu)$ are symmetrical and triangular, so that one may set ν^* equal to the mean frequency $\bar\nu$, rewriting Eq. 1.6 as

$$I(\bar\nu,o) = B(\bar\nu,T(p_o))\,\tau(\bar\nu,p_o)$$

$$-\int^{\tau(\bar\nu,p_o)} B(\bar\nu,T(p))\,d\tau(\bar\nu,p) \qquad (1.8)$$

The purpose of the inversion is to solve for the function $B(\nu,T(p))$, knowing the radiance $I(\nu,o)$ and the transmittance given by Eq. 1.7. The Planck radiance $B(\nu,T(p))$ has a different form at different frequencies. For example, in the microwave region the Rayleigh Jeans approximation holds

$$B(\nu,T) = 2\nu^2 ckT \quad ; \quad \text{Rayleigh Jeans, for microwave} \quad (1.9)$$

and in the region of the 4.3 micron carbon dioxide band Wien's law holds:

$$B(\nu,T) = 2h\nu^3 c^2 e^{-\frac{hc\nu}{kT}}; \text{Wein's Law, for } 4.3\mu \qquad (1.10)$$

In the vicinity of the 15 micron carbon dioxide band, Wark suggests the approximation

$$B(\nu,T(p)) = \alpha(\nu)\,B(\nu_r,T(p)) + \beta(\nu) \quad \text{for } 15\mu \text{ line} \quad (1.11)$$

11

where subscript r indicates a fixed reference frequency which is chosen near the middle of the range of frequencies. This approximation holds only over a limited part of the spectrum.

With the several limitations stated above, the Eq. 1.8 for the 15 micron band may be written as

$$\frac{I(\nu,o) - \beta(\nu)}{\alpha(\nu)} = -\int_{0}^{t_o} B(\nu_r, T(t)) \frac{d\tau(\nu,t)}{dt} dt \tag{1.12}$$

where $\bar{\nu}$ is written as ν for convenience, and t is a general independent variable to which pressure may be transformed, usually $t = \log p$.

Equation 1.12 is a Fredholm equation of the first kind

$$g(\nu) = \int_{t}^{t_o} k(\nu,t) f(t) dt$$

wherein

$$k(\nu,t) = \frac{d\tau}{dt}$$

$$f(t) = B(\nu_r, T(t)) \tag{1.13}$$

$$g(\nu) = \left[I(\nu,o) - \beta(\nu) \right] / \alpha(\nu)$$

In the atmosphere, the transmittance of Eqs. 1.4 and 1.7 is a determining factor in the radiance to be observed from a satellite at any frequency and depends upon the spectral interval observed. Through most of the atmosphere up to about 50 km the broadening of spectral lines is dominated by collisions; above that level Doppler broadening of the lines dominates. One finds in the meteorologically interesting, collision-broadened atmosphere that lines have Lorentz shapes for which

$$k(\nu) = \frac{\alpha}{\pi\left[(\nu - \nu_o)^2 + \alpha^2\right]} \int_{0}^{\infty} k(\nu) d\nu \tag{1.14}$$

12

where ν_o is the frequency of the line center and α is the halfwidth of the line. For an isothermal atmosphere, the halfwidth is

$$\alpha = \alpha_o \frac{p}{p_o} \left(\frac{T}{T^o}\right)^{\frac{1}{2}} \tag{1.15}$$

where subscript o denotes α, T and p at NTP.

Shown in Fig. 2 is a medium-high resolution spectrum of the 15 micron carbon dioxide band, obtained from a 10 cm path of pure carbon dioxide at 63 mb and 38 °C (After Wark and Fleming, 1966).
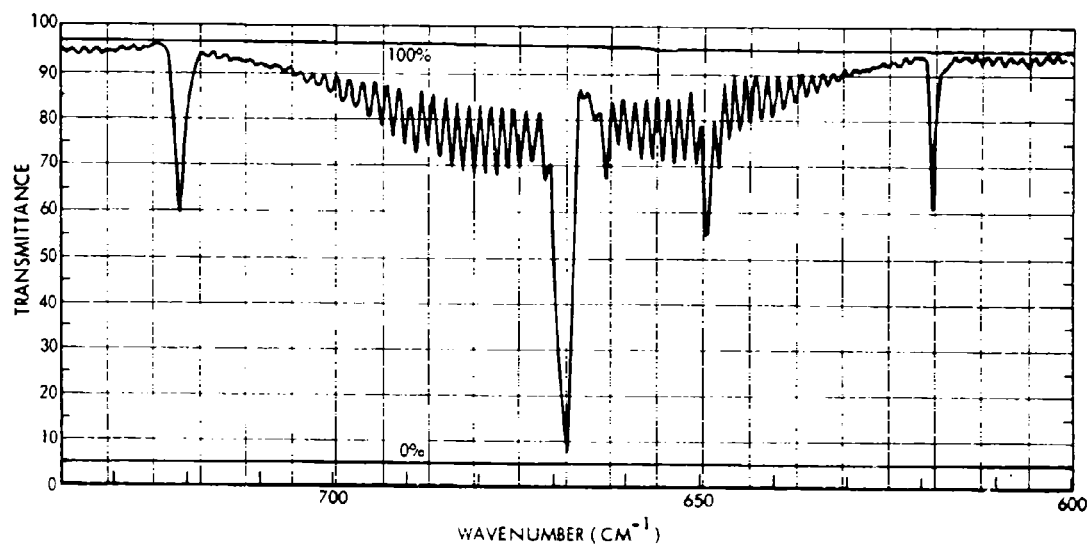
FIGURE 2. Spectrum of 15 Micron Carbon Dioxide Band
(After Wark and Fleming, 1966)

Shown in Fig. 3 are the six components of the kernel $d_T(\nu,p)/d$ log p versus log p, in the 15 micron carbon dioxide band at 669, 677.5, 691, 697, 703 and 709 cm^{-1}. These curves may be considered as weighting functions for the Planck radiance in Eq. 1.12. They show from what part of the atmosphere the outgoing radiance arises. It is

13
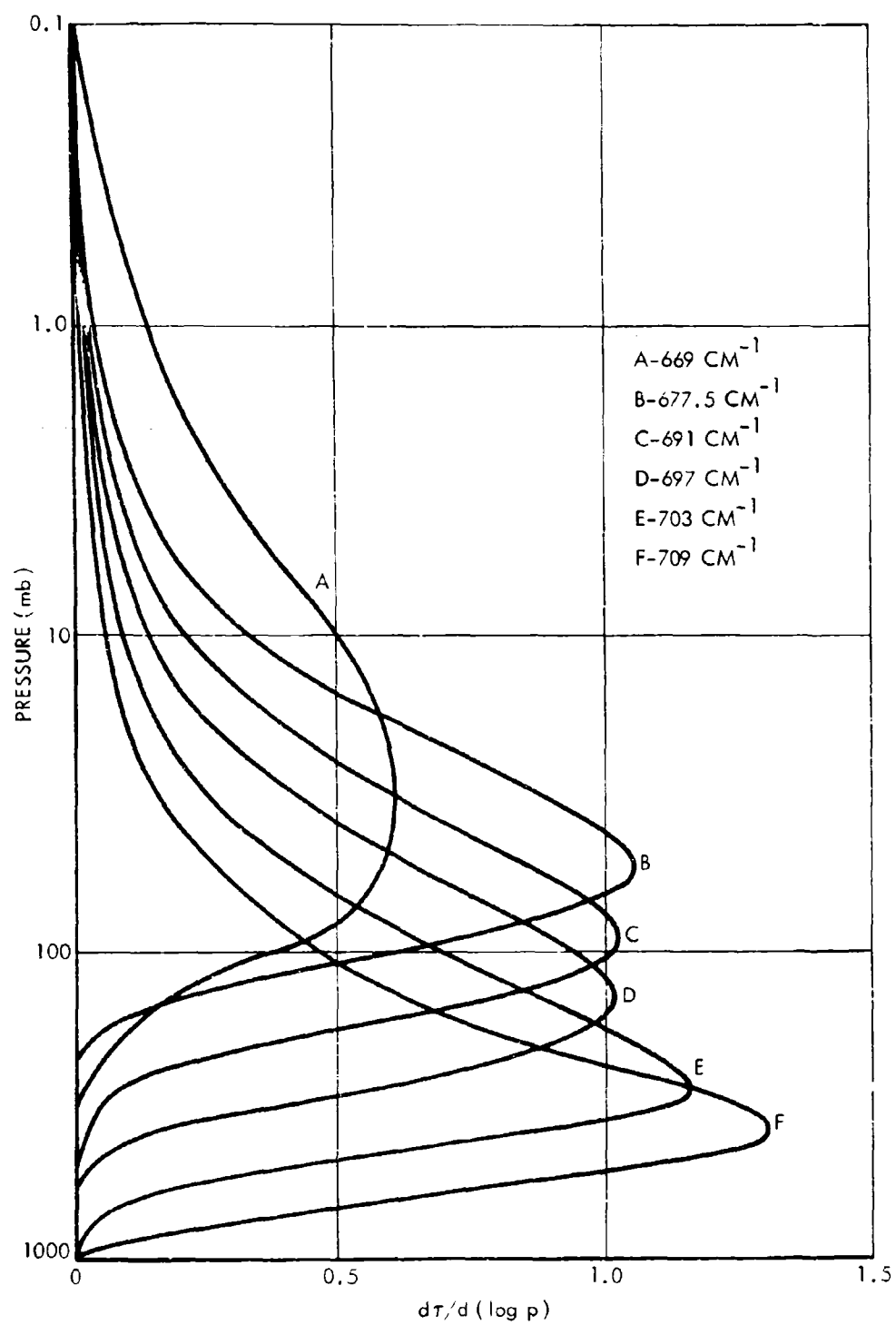
FIGURE 3. Kernel dτ/d (log p) (After Wark & Fleming, 1966)

The figure shows curves labeled A through F plotted as $d\tau/d(\log p)$ (horizontal axis, 0 to 1.5) versus PRESSURE (mb) on the vertical axis (logarithmic, 0.1 to 1000).

A-669 CM^{-1}
B-677.5 CM^{-1}
C-691 CM^{-1}
D-697 CM^{-1}
E-703 CM^{-1}
F-709 CM^{-1}

necessary that the weighting functions overlap a little, but not too much, in order to obtain enough data to make possible adequate definition of the temperature profile. With no overlap, the solution is meaningless except that it represents a mean weighted value of temperature over the whole atmosphere. With too much overlap, the errors of measurement may exceed the ability of the weighting functions to discriminate between the levels of the atmosphere from which the radiation is arising.

Once the form of the indicial function $f(t)$ has been determined (from the alternative Eqs. 1.9, 10 or 11), one may reduce the integral Eq. 1.13 to a system of linear algebraic equations by applying an appropriate numerical quadrature formula. If, for example, the indicial function is

$$f(t) = \sum_{j=1}^{n} c_j \, \varphi_j(t) \tag{1.16}$$

where $\varphi_j(t)$ are a set of orthogonal functions, then with Eq. 1.16, Eq. 1.12 becomes

$$g(\nu_\iota) = \sum_{j=1}^{n} c_j \int_{0}^{t_0} k(\nu_\iota, t) \, \varphi_j(t) \, dt \qquad \iota = 1, \ldots, n \tag{1.17}$$

or in matrix notation

$$\tilde{g} = \tilde{A} \, \tilde{c}$$

Inverting yields

$$\tilde{c} = \tilde{A}^{-1} \, \tilde{g} \tag{1.18}$$

where $\tilde{A}^{-1}$ is the inverse of the matrix $\tilde{A}$ whose elements are given by the integrals of 1.17, $\tilde{g}$ is the vector expression of the observed

15

quantities $g(v_t)$, and $\tilde{c}$ is the vector of undetermined coefficients, which then evaluated are used to determine $B(T) = f(t)$, and from thence temperature $T(t)$.

The solution of Eq. 1.18 is unstable if more than three equations are considered, due to the following sources of error: the approximation of the Planck function, the numerical quadrature process and roundoff.

The computational instability has been made tractable by use of the solution

$$\tilde{c} = (\tilde{A}^T \tilde{A} + \gamma \tilde{H})^{-1} (\tilde{A}^T \tilde{g} + \gamma \tilde{h}) \qquad (1.19)$$

where $\tilde{A}^T$ is the transpose of $\tilde{A}$, γ is the smoothing parameter, $\tilde{H}$ is the smoothing matrix and $\tilde{h}$ is a bias vector which is a gross estimate of the solution vector $\tilde{c}$. Fleming and Wark (1966) find that $\gamma = 10^{-5}$ is pragmatically effective.

TEMPERATURE UNCERTAINTY

Wark and Fleming (1966) have made estimates of error of temperature determinations of a six channel (of 5 cm^{-1} bandwidth) spectrometer measuring radiances of about 50 ergs sec^{-1} cm^{-2} $ster^{-1}$ cm^{-1}. For errors of $\frac{1}{2}$, 1, 2, and 4 percent in the measure of radiance, corresponding to $\sigma = 0.25$, 0.5, 1.0 and 2.0 ergs sec^{-1} cm^{-2} $ster^{-1}$ cm^{-1}, of a set of 110 random values, the errors of the computed Planck function B, and of the computed temperature T associated with B by the relation

$$\overline{\Delta T} = \frac{\overline{\Delta B}}{\overline{B}} \left[\frac{2v_r^2 \, ck\overline{T}^2}{2hv_r^3 \, c^2 + \overline{B}} \right] \qquad (1.20)$$

are given in Table 4. In the table, the columns marked "maximum" are for the fifth largest value, the units for σ, $\overline{B}$, $\Delta\overline{B}$ and Max ΔB are ergs sec^{-1} cm^{-2} $ster^{-1}$ cm^{-1} and the units for $\overline{T}$, $\Delta\overline{T}$, and Max ΔT are $^\circ K$.

16

TABLE 4. TEMPERATURE ERROR RESULTING FROM RANDOM ERROR OF OBSERVATION
(AFTER WARK AND FLEMING, 1966)

σ	γ	$\bar{B} \pm \overline{\Delta B}$	$\bar{T} \pm \overline{\Delta T}$	Max. ΔB	Max. ΔT
KEY WEST					
0	10^{-4}	47.59 ± 0.96	224.65 ± 1.01	0.96	1.01
0.25	0.025	47.59 ± 1.80	224.65 ± 1.90	2.50	2.63
0.5	0.050	47.60 ± 2.01	224.66 ± 2.12	2.85	3.00
1.0	0.150	47.61 ± 3.04	224.67 ± 3.20	4.63	4.88
2.0	0.400	47.63 ± 4.42	224.69 ± 4.66	6.36	6.70
LITTLE ROCK					
0	10^{-4}	47.39 ± 0.93	224.43 ± 0.98	0.93	0.98
0.25	0.025	47.39 ± 1.21	224.43 ± 1.28	1.69	1.79
0.5	0.050	47.40 ± 1.54	224.44 ± 1.63	2.55	2.69
1.0	0.150	47.41 ± 2.13	224.46 ± 2.25	3.62	3.82
2.0	0.400	47.43 ± 2.81	224.48 ± 2.97	4.38	4.63
SEATTLE					
0	10^{-4}	43.84 ± 0.69	220.60 ± 0.76	0.69	0.76
0.25	0.025	43.84 ± 1.60	220.60 ± 1.77	2.47	2.73
0.5	0.050	43.85 ± 1.89	220.61 ± 2.09	3.27	3.61
1.0	0.150	43.86 ± 2.45	220.62 ± 2.70	4.47	4.93
2.0	0.400	43.88 ± 3.05	220.64 ± 3.37	5.25	5.79
CHURCHILL					
0	10^{-4}	35.13 ± 0.86	210.36 ± 1.08	0.86	1.08
0.25	0.025	35.13 ± 1.71	210.36 ± 2.14	2.24	2.81
0.5	0.050	35.14 ± 1.96	210.38 ± 2.46	2.89	3.63
1.0	0.150	35.15 ± 2.79	210.39 ± 3.50	4.65	5.84
2.0	0.400	35.17 ± 4.14	210.41 ± 5.20	6.25	7.84

From the table it may be seen that errors of radiance equal to
or greater than about 1% or 0.5 erg sec^{-1} cm^{-2} ster^{-1} cm^{-1} lead to
results with temperature error greater than 1% or about 2 $^\circ$K.

17

W. L. Smith (1968) has made an estimate of the errors of the atmosphere's temperature versus pressure distribution as determined from satellite radiation measurements, using as an instrument the Satellite Infrared Radiation Spectrometer (SIRS) which has flown in the NIMBUS III meteorological satellite.

SIRS detects emissions in 5 cm^{-1} bands at the five CO_2 channels near 15 microns (669, 677.5, 692, 699, and 706 cm^{-1}) as well as two channels in the far wing (at 714 and 748 cm^{-1}) and an atmospheric window at 899 cm^{-1}. The uncertainty of temperature determination by SIRS is shown in Fig. 4 for the case of both clear and cloudy conditions, and for errors of 0.01 and 0.25 erg sec^{-1} cm^{-2} $ster^{-1}$ cm^{-1} in the determination of radiance values from 50 to 70 erg sec^{-1} cm^{-2} $ster^{-1}$ cm^{-1}. The temperature uncertainty is seen to be less than $3^O K$.
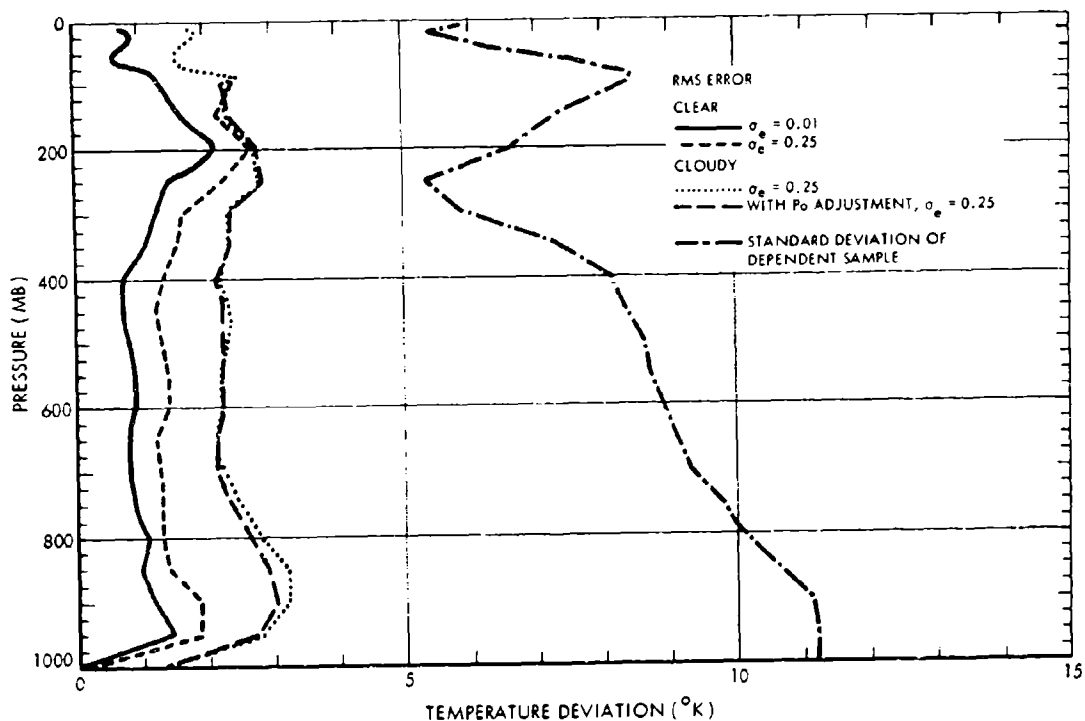
FIGURE 4. Uncertainty of Temperature Determination by SIRS (after W.L. Smith, 1968)

18

HEIGHT UNCERTAINTY

W. L. Smith (1968) also describes a method of estimating the pressure versus height relation from the radiometric measurements, employing empirical orthogonal functions developed by Holmstrom (1963). By the Holmstrom technique, the geopotential height is represented by the rapidly converging series

$$Z(p) = \sum_{k=1}^{k} c_r \, \varphi_R(p) \qquad (1.21)$$

Holmstrom's studies of eight days data indicate that for meteorological studies in the pressure range 100 to 1000 mb, the empirical orthogonal functions, $\varphi_R(p)$, are statistically stable in being nearly invariant with respect to geographical position and time, over the space and time intervals usually considered by numerical weather prediction. From the hydrostatic Eq. 1.2, and the gas law, used with Eq. 1.21, it follows

$$T(p) = -\frac{g}{R} \frac{\partial z(p)}{\partial \ell n p} = -\frac{g}{R} \sum_{k=1}^{k} c_R \frac{\partial \varphi_R(p)}{\partial \ell n p}$$

$$= \sum_{k=1}^{k} c_R \, x_R(p) \qquad (1.22)$$

In matrix notation, Eqs. 1.21 and 1.22 may be written

$$\vec{Z} = \tilde{\varphi} \, \vec{c}$$

$$\vec{T} = \tilde{X} \, \vec{c}$$

wherein

$$\tilde{\varphi} = (\varphi_{jk})$$

$$\tilde{X} = (x_{jk})$$

Combined, these yield

$$\tilde{T} = \tilde{X}(\tilde{\phi}^T \tilde{\phi})^{-1} \tilde{\phi}^T \vec{Z} = \tilde{D} \vec{Z} \tag{1.23}$$

which states the geopotential height profile is uniquely related to the temperature profile. Then, to the extent that Eq. 22 is valid, the height distribution can be specified solely from the temperature profile. W. L. Smith (1968) estimate of uncertainty of height determination by SIRS, for which the temperature uncertainty is given in Fig. 4, is shown for similar case in Fig. 5.

Assuming that the empirical orthogonal functions evaluated statistically at the time are invariant, the uncertainty of height due to the inversion computation alone is seen to be less than 60 meters, or expressed fractionally less than 0.002 to 0.01.
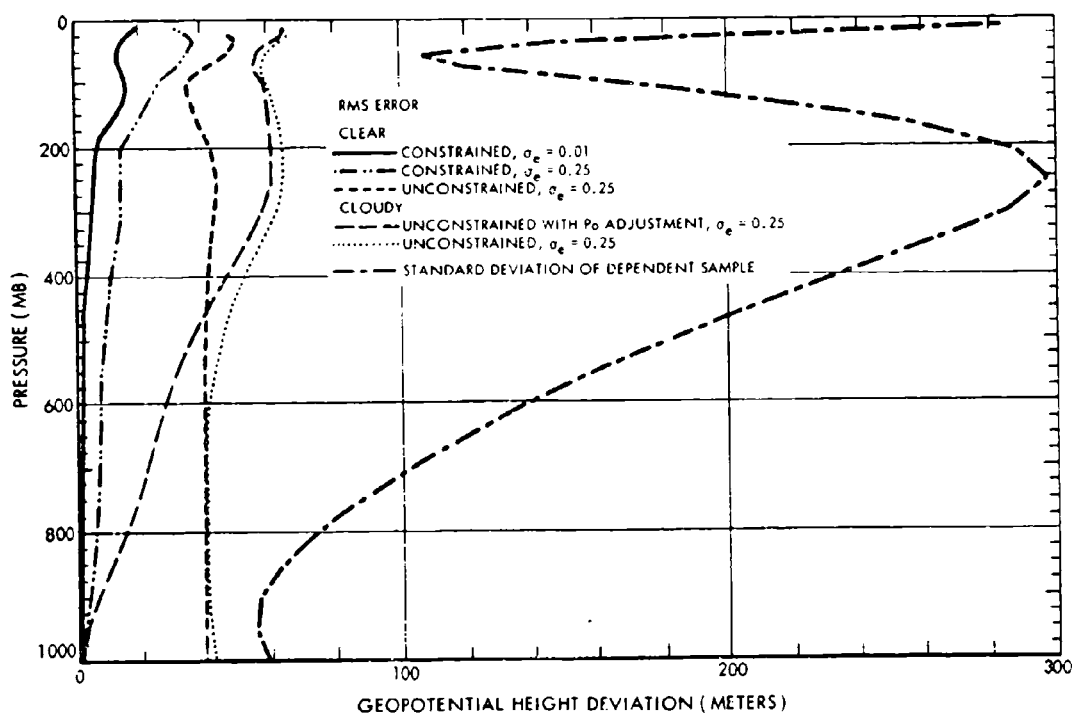
FIGURE 5. Uncertainty of Height Determination by SIRS
(After W.L. Smith, 1968)

By the equation relating the uncertainties of density and height,

$$\frac{d\rho}{\rho} = - \frac{dz}{H} \qquad (1.24)$$

wherein H is the scale height, about 7 km, the fractional uncertainty of density is about 1%.

Since the linear spatial resolution on the ground of the SIRS is about 225 km, the interval between clouds cannot be resolved by a single observation. However, according to Suomi (1969), the NASA ATS satellites have demonstrated that time and space can be traded; that is, a 90% cloud cover could be effectively sounded to the ground in one hour of observation. By means of such a tradeoff, a 10 to 15 km resolution radiometer makes possible altitude coverage all the way to the ground. A. W. McCulloch and W. L. Smith (1969) have proposed a high resolution temperature sounder, with 7.5 km ground resolution, by which the intervals between clouds may be resolved, thereby permitting resolution of smaller temperature and height uncertainties described as "clear, $\sigma_e = 0.25$" in Figs. 4 and 5, namely less than 2 ^{O}K and $\pm$0 meters over most of the altitude range, 0 to 10 km.

As may be judged by inspection of Figs. 3, 4, and 5, the determination of temperature and pressure or height by the inversion of nadir directed radiometer measurements of the 15 micron CO_2 line is effective only between the earth's surface, or the top of the cloud layer if uninterrupted, and the height of the 10 mb surface, approximately 30 km. J. C. Gille (1968) has suggested the inversion of horizon-directed radiometer measurements of the 15 micron CO_2 line to determine the temperature, and the pressure or height, in the stratopause, from 30 to 60 km. Since the absorption is proportional to the density-path length integral, the horizon-directed measurements are sensitive to the atmosphere at higher altitudes than are the nadir-directed measurements, and the weighting functions are similar in shape, but much narrower, than those of Fig. 3. J. C. Gille's estimate of uncertainty is based on the following considerations. Assuming a

21

satellite at 400 km altitude, the vertical dimension for a 1 milli-
radian field of view is approximately 0.4 km. Over this height the
curvature of the radiance profiles is small, so that changes may be
easily resolved in the field of view. Gille considers a cooled or-
biting optical system and detector capable of measuring a full scale
signal of 7 $w\ m^{-2}\ ster^{-1}$ to an uncertainty of 0.01 $w\ m^{-2}\ ster^{-1}$, or
0.14%. Pointing errors may be the limiting factor in determining
resolution because of the large radiance profile slope, about 0.2
$w\ m^{-2}\ ster^{-1}\ km^{-1}$. If the pointing error is one milliradian, the re-
sulting uncertainty of tangent height will approximate 0.4 km yielding
error of about 0.08 $w\ m^{-2}\ ster^{-1}$, or about 1%. The two error sources
(in radiance measurement and pointing) may, therefore, contribute to
a total measurement error of about 1%. The contribution of error due
to the computational inversion may be expected to be the same as in
the case of the nadir-directed radiometry.

McKee et al. (1969) have analyzed the errors of temperature de-
termination from horizon radiance profiles of the 15 micron CO_2 line,
for the altitude range 20.5 to 55.5 km. McKee et al. find that the
error sources shown in Table 5 are realizable, and contribute errors
in temperature determination as indicated.

TABLE 5.   ERRORS OF TEMPERATURE FROM HORIZON RADIANCE PROFILES
(McKee et al., 1969)

ERROR		AT ALTITUDE 20 KM		AT ALTITUDE 50 KM	
TYPE	MAGNITUDE	FOR SIGNAL $W\ M^{-2}\ STER^{-1}$	$\Delta T_{^\circ k}$	FOR SIGNAL $W\ M^{-2}\ STER^{-1}$	$\Delta T_{^\circ k}$
SCALE ERROR	(0.01 SIGNAL)	5.92	0.5	1.10	1.16
BIAS ERROR $W\ M^{-2}\ STER^{-1}$	0.01		0.03		0.12
NOISE ERROR $W\ M^{-2}\ STER^{-1}$	0.01		2.30		0.93
TANG. HEIGHT ERROR $W\ M^{-2}\ STER^{-1}$	0.5		1.35		3.80
PRESSURE ERROR	(0.1 PRESSURE)		1.52		5.79

22

Other radiation bands may be used similarly. At the low altitudes, below 30 km, two interesting constituents of the atmosphere which are highly variable in mixing ratio are water vapor and ozone. As is shown in Fig. 6, the absorption coefficient of water vapor in the infrared is about two orders of magnitude greater than that of carbon dioxide, which is nearly constant in mixing ratio. Radiometer measurements in either of the two H_2O bands shown in Fig. 6 may yield data on the mixing ratio-height distribution of water vapor. However, since the ozone band absorption coefficient is of the same approximate size as the CO_2 band, and the mixing ratio is far smaller in the altitude range of interest, still another band of radiation should be considered -- that of the Hartley band in the ultraviolet -- for the determination of the ozone mixing ratio-height distribution.
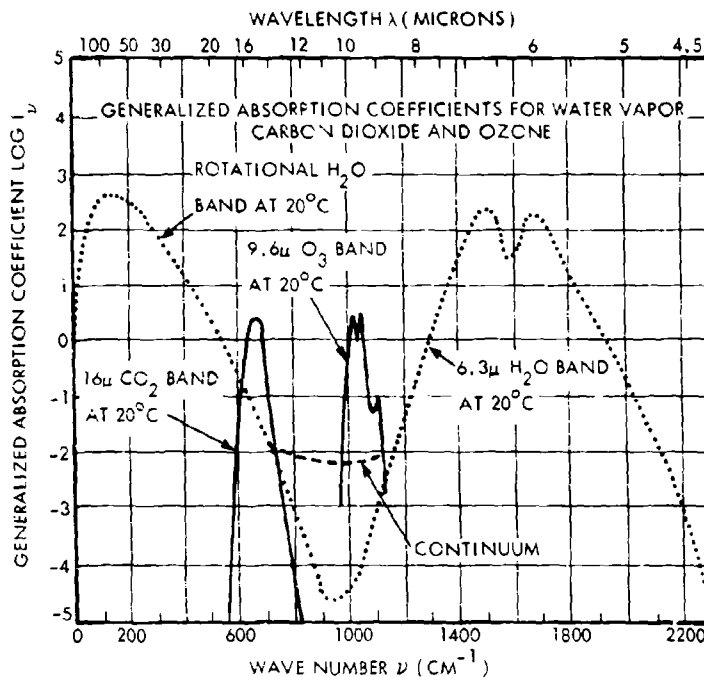
FIGURE 6. Generalized Absorption Coefficients for the Major Absorbing Bands H_2O, CO_2 and O_3 (After Elsasser and Culbertson, 1960)

S. Twomey (1961) has described the problem of manipulating ultraviolet spectral measurements in the wavelength region 2800 to 3000 A for the determination of ozone mixing ratio-height distribution from the solar radiation backscattered from above the median ozone level (about 25 km). Twomey anticipated that the error of ozone determination can be made less than 1%. Herman and Yarger (1969) have elaborated the concept to indicate the method should be effective over the range 2 to 40 km.

DENSITY OF H_2O and O_2 BY MICROWAVE EMISSION

A third region for application of inversion of radiometer measurements if the atmospheric microwave spectrum, notably the weak resonance of water vapor near 22 GHz (1 GHz = 10^9 cps) or 1.35 cm wavelength and the strong complex of oxygen resonances near 60 GHz (0.5 cm). Atmospheric emission at these frequencies can be received with microwave radiometers, and the received radiance expressed in terms of the brightness temperature T_B may be measured. The accuracy with which T_B may be measured is 0.2 to 1.0 $^\circ$K. Since the Planck function B is essentially linear in this spectral region, as indicated in Eq. 1.9, the inversion of Eq. 1.8 is straightforward.

In the nearly opaque regions of the spectrum the temperature profile may be obtained in a manner exactly analogous to that in the infrared spectral region. In the nearly transparent regions water vapor and perhaps ozone may be inferred in some circumstances, especially oversea areas. Because a microwave radiometer looking down may see water vapor or ozone in absorption or emission, dependent on the brightness temperature of the surface, the highly emissive land areas are characterized by a brightness temperature nearly the same as the atmospheric temperature. Over water areas, the surface emissivity ($\epsilon(\nu)$) of Eq. 1.3 and the surface brightness temperature (effect of the first term of Eq. 1.3) are low, and the atmospheric emissions (the second term of Eq. 1.3) are unambiguous. Waters of MIT, cited by Gille (1968), has quoted the inversion

uncertainties associated with zero and 1% errors of microwave radio-
meter measurements to be 2 to 3.7 ^{O}K (about 1%) for temperatures
at altitudes below 15 km, and to be 0.09 to 0.11 gm cm^{-2} (about 3
to 30%) for integrated water vapor, and that the height resolution
is comparable to that of the 15 micron infrared channels; that is
the emission by oxygen in a spectral channel of 0.2 GHz width comes
mainly from an atmospheric layer about 10 km thick.

SYSTEMS CONSIDERATIONS

Although systems studies, involving cost-effectiveness compari-
sons with physically feasible alternatives, are beyond the scope of
the study effort reported in this volume, nevertheless some analogies
to proven systems can be made. The techniques for measurement of
atmospheric emission, as probes of the altitude region up to 30 km,
have been largely proven by NIMBUS and TIROS satellites, the history
and characteristics of which are described in some detail in Appendix
A of this volume. The 700 lb NIMBUS and 300 lb TIROS satellites orbit
sun-synchronously at altitudes of 400 to 600 nmi, making measurements
continuously along a swathe about 500 nmi wide along the orbital
projection on the earth's surface. Eight such satellites, with
ascending nodes at 45° intervals, are required to obtain measure-
ments over all the earth at three hour intervals.

By means of a system of similar sensor complexity with the
addition of a directionally stabilized pointing control, in similar
sun-synchronous orbits, the atmosphere can be probed for density and
temperature at all altitudes up to about 60 km.

SUMMARY

In summary, inversion of radiometric measurements from an earth
orbiting satellite yields the distribution with respect to altitude,
of temperature, total particle density, pressure, and density of
water vapor, carbon dioxide, molecular oxygen and ozone, with frac-
tional uncertainty between one and two percent, as indicated in more
detail in Table 6.

TABLE 6. INVERSION OF ATMOSPHERIC EMISSION

EMISSION LINE		ATMOS. PARAMETER		FRACT. UNCERTAINTY MEAS.	INVER.	TOTAL	ALTITUDE RANGE, km	NOTE
2800-3000A	O_3	Density O_3	vs Z			0.01	2-40	Daytime Only (Solar Backscatter)
6.3μ	H_2O	Density H_2O	vs Z				0-20	Above Clouds
15μ NADIR	CO_2	Temperature	vs p	0.01	<0.01	0.01	0-30	Above Clouds
		Altitude	vs p		0.002-0.01	0.01	0-30	Above Clouds
		Density (Total, CO_2)	vs Z		0.01	0.01	0-30	Above Clouds
HORIZON		Temperature	vs p	0.01	<0.01	0.01	30-60	Above Clouds
		Altitude	vs p		0.01	0.01	30-60	Above Clouds
		Density (Total, CO_2)	vs Z		0.01	0.01	30-60	Above Clouds
22 GHz (0.5 cm)	H_2O	Temperature	vs p	0.005	0.01	0.01	0-15	Penetrates Clouds
		Integ. Density H_2O	vs Z		0.03-0.3	0.3	0-15	Penetrates Clouds
53.5 GHz (1.35 cm)	O_2	Temperature	vs p	0.005	0.01	0.01	0-5	Penetrates Clouds
		Altitude	vs p		0.002-0.01	0.01	0-5	Penetrates Clouds
		Density (Total, O_2)	vs Z		0.01	0.01	0-5	Penetrates Clouds

26

ABSORPTION OF SOLAR RADIATION

One technique by which the vertical distribution of the temperature and density of the atmosphere may be determined remotely by satellite-borne instrumentation is the observation of the variable absorption of solar radiation as the satellite crosses the terminator, that is, as the line of sight from the satellite to the sun is occulted by the solid earth and its atmosphere. By suitable choice of lines or wave bands of the solar spectrum which are selectively absorbed by the earth atmosphere, the density and temperature of neutral components of the atmosphere may be determined in the upper atmosphere (e.g., from about 80 to 300 km altitude) where other techniques are often inapplicable.

A characterization of the technique is given in Fig. 7, which summarizes considerations reviewed in the following paragraphs, dealing in turn with basic theory, characteristics of the solar radiation wave bands, detector characteristics and vehicle and system considerations.

RADIATIVE TRANSFER

The principles of radiative transfer which govern the technique of determining density by observing the absorption of solar radiation at various depths in the atmosphere differ from those described in the discussion of the inversion of atmospheric emission in that the emission of the atmosphere is taken to be negligible by comparison with that of the solar source. In consequence, the spectral radiance from the sun detected at the satellite may be described as

$$N_s(\lambda) = N_o(\lambda) \exp\left\{-\int_h^\infty \sigma n(z) F\left(\frac{a + z}{H}, \Xi\right) dz\right\} \qquad (2.1)$$

PRINCIPLE OF OPERATION

- ABSORPTION = f(ρ, K, χ) OF ABSORBING GAS
- MASS ABSORPTION COEFFICIENT (K) KNOWN IN X-RAY AND EUV
- PATH LENGTH (χ) KNOWN BY GEOMETRY
- DETERMINES DENSITY (ρ)

UNCERTAINTY OF MEASUREMENT

- DENSITY: 10%
- TEMPERATURE: 10%

COVERAGE IN VOLUME

- DENSITY AVERAGED OVER VOLUME 7 KM x 300 KM x 1.6 KM
- TWO VERTICAL PROFILES FROM 90 TO 300 KM ALTITUDE, PER ORBIT
- NINE SATELLITES FOR DAILY SAMPLE IN 1800 KM GRID SPACING

STATUS OF DEVELOPMENT

- PRINCIPLE DEMONSTRATED BY ROCKET EXPERIMENTS
- DATA ANALYSIS BY COMPUTER DEMONSTRATED

RECOMMENDATION

- INVESTIGATE FEASIBILITY OF SATELLITE SYSTEM FOR NEEDS OF LOW ALTITUDE SATELLITE ORBIT
  PREDICTION, USEFUL FOR RADIO COMMUNICATION.
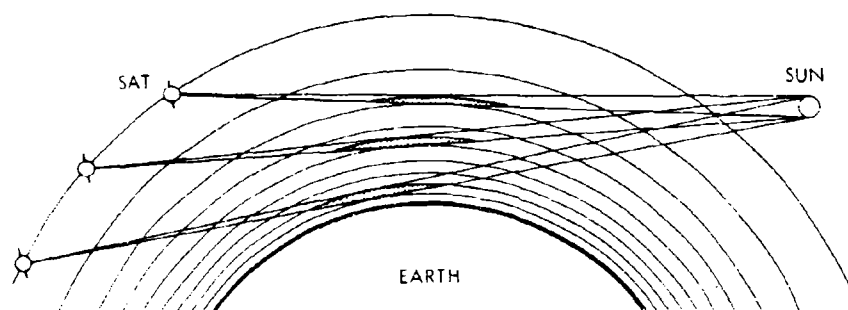
ATMOSPHERIC ABSORPTION OF SOLAR RADIATION

FIGURE 7. Measurement of Absorption of Solar Radiation for Density at 90-300 km

wherein E is the spectral radiance at a given wavelength λ, at altitude h

E_O is the spectral radiance of the sun outside the absorbing atmosphere

σ is the absorption cross section (cm^2)

n is the number density of the absorbing gas (cm^{-3}), at altitude z

λ is the wavelength of monochromatic radiation

F is the Chapman function (of a, z, H and Ξ)

a is the radius of the earth

Ξ is the solar zenith angle

H is the atmospheric scale height

z is the altitude in the atmosphere

The Chapman function $F\left(\dfrac{a+z}{H}, \Xi\right)$ takes into account that the incidence of radiation is not normal. In the relation of Eq. 25, if the latter were written for a plane stratified atmosphere, $F\left(\dfrac{a+z}{H}, \Xi\right)$ becomes sec Ξ. It has values, in the case of the spherically stratified atmosphere of the earth, that are tabulated in Swider (1964) (e.g., $F \approx 39$ and sec $\Xi = \infty$ at $\Xi = \frac{\pi}{2}$). The power detected by a radiometer is represented by the integral over the inner product of the incident spectral radiance and the spectral efficiency of the detector, over a band wavelengths to which the radiometer is sensitive.

If the radiant flux is characteristically that of a black body, then the incident radiance over a wave band limited by λ_1, λ_2 detected by an ion chamber sufficiently excited to pass current I within limits of its sensitivity $(\lambda_{min}, \lambda_{max})$, will be given by

$$E(\lambda_1, \lambda_2) = \frac{I(\lambda_{min}, \lambda_{max})}{q\sigma a} \frac{\displaystyle\int_{\lambda_1}^{\lambda_2} \frac{d\lambda}{\lambda^5(e^{c_2/\lambda\tau} - 1)}}{\displaystyle\int_{\lambda_{min}}^{\lambda_{max}} \frac{\tau(\lambda)\, d\lambda}{\lambda^5(e^{c_2/\lambda\tau} - 1)}} \qquad (2.2)$$

wherein I = ion chamber current

ε = photon detection efficiency, within limits λ_{min}, λ_{max}

$E(\lambda_1, \lambda_2)$ = energy flux in the band of wavelengths λ_1, λ_2

ω = ion pairs formed in the ion chamber per erg of radiant energy

λ = wavelength

a = aperture area of detector

q = electron charge

c = velocity of light

h = Planck's constant

C_2 = 1.439 cm $^{\circ}K$

T = temperature of black body source

For the case when in Eq. 2.2, the bands of energy flux to be determined and those of the detector sensitivity are the same, then the flux is proportional to the current in the detector

$$E = \left(\frac{1}{q\omega a \overline{\varepsilon}}\right) I \tag{2.3}$$

wherein $\overline{\varepsilon}$ is an averaged value of photon detection efficiency.

Considering now the flux at an altitude h, over a wave band (limited by λ_1, λ_2), as the integral of Eq. 2.1

$$E(\lambda_1, \lambda_2, h) = \int_{\lambda_1}^{\lambda_2} E_0(\lambda) \exp\left(-\int_{h}^{\infty} \sigma(\lambda, z) n(z) F\left(\frac{a+z}{H}, \varphi\right) dz\right) d\lambda \tag{2.4}$$

then the logarithmic derivative is

$$\frac{d \ln E(h)}{dz} = \frac{1}{E} \frac{d\ E(h)}{dz}$$

$$= \frac{\int_{\lambda_1}^{\lambda_2} E_0(\lambda) \exp\left(-\int_h^\infty \sigma(x,z)n(z)F\left(\frac{a+z}{H}, \Xi\right)dz\right)\left(-\sigma(\lambda,z)n(z)F\left(\frac{a+z}{H}, \Xi\right)\right)d\lambda}{\int_{\lambda_1}^{\lambda_2} E_0(\lambda) \exp\left(-\int_h^\infty \sigma(\lambda,z)n(z)F\left(\frac{a+z}{H}, \Xi\right)dz\right)d\lambda} \tag{2.5}$$

If over the narrow band of sensitivity of the radiometer $E_0(\lambda)$ is taken as that of a black body, then Eq. 2.5 may be written, with z in lieu of h, as

$$\frac{d \ln E(z)}{dz} = n(z)\ F(z) \left[\frac{\int_{\lambda_1}^{\lambda_2} \sigma(\lambda,z) \dfrac{\exp\left(-\int_h^\infty \sigma(\lambda,z)n(z)dz\right)}{\lambda^5\left(e^{C_2/\lambda T} - 1\right)}\,d\lambda}{\int_{\lambda_1}^{\lambda_2} \dfrac{\exp\left(-\int_h^\infty \sigma(\lambda,z)n(z)dz\right)d\lambda}{\lambda^5\left(e^{C_2/\lambda T} - 1\right)}}\right] \tag{2.6}$$

from which the density may be evaluated by

$$n(z) = \frac{d \ln E(z)/dz}{\bar{\sigma}(z)\ F(z)} \tag{2.7}$$

wherein $\bar{\sigma}(z)$ is a mean value evaluated as the quantity in square brackets in Eq. 2.6.

Also the density over a short interval of altitude may be evaluated in terms of scale height

$$H(z) = \frac{k}{g} \frac{T(z)}{\bar{m}(z)} \tag{2.8}$$

32

as
$$n = n_o \, e^{-z/H} \tag{2.9}$$

so that
$$H(z) = -\left(\frac{d\ln n(z)}{dz}\right)^{-1} \tag{2.10}$$

wherein   T is temperature

     z is altitude

     k is Boltzmann's constant

     g is the acceleration due to gravity

     $\bar{m}$ is the mean molecular weight of the atmosphere.

With the description of density given as in Eq. 2.9, the temperature may be determined by the derivative relation

$$T(z) = -\frac{g}{R}\left(\frac{d\ln n(z)}{dz}\right)^{-1}\left(\bar{m}(z)\right)^{-1} \tag{2.11}$$

In short, from a height profile of radiance, determined from radiometer measurements by Eq. 2.2, the height profile of density may be determined by Eq. 2.7, the height profile of scale height by Eq. 2.10, and if the mean molecular weight $\bar{m}(z)$ be known, the temperature profile may be determined by means of Eq. 2.11.

The certainty of an individual data point associated with determination of each of the parameters for which profiles in height are made may be described by the following relations.

Assuming the measurements of detector current I and detector efficiency are independent, the variance in determination of flux is described by

$$\left(\frac{\Delta E}{E}\right)^2 = \left(\frac{\Delta I}{I}\right)^2 + \left(\frac{\Delta \varepsilon}{\varepsilon}\right)^2 \tag{2.12}$$

Similarly assuming independence of the determinations of radiance, absorption cross section and Chapman constants, and that

the independence of radiance and radiance gradient is described by correlation ρ_E, the variance of the determination of density is given by

$$\left(\frac{\Delta n}{n}\right)^2 = \left(\frac{\Delta \text{ grad } E}{\text{grad } E}\right)^2 + \left(\frac{\Delta E}{E}\right)^2 + \left(\frac{\Delta \sigma}{\sigma}\right)^2$$

$$+ \left(\frac{\Delta F}{F}\right)^2 + 2\rho_E \left(\frac{\Delta \text{ grad } E}{\text{grad } E}\right)\left(\frac{\Delta E}{E}\right) \qquad (2.13)$$

Also, assuming the dependence of the determinations of density and density gradient as described by correlation ρ_H, the variance of scale height is given by

$$\left(\frac{\Delta H}{H}\right)^2 = \left(\frac{\Delta n}{n}\right)^2 + \left(\frac{\Delta \text{ grad } n}{\text{grad } n}\right)^2 + 2\rho_H \left(\frac{\Delta n}{n}\right)\left(\frac{\Delta \text{ grad } n}{\text{grad } n}\right) \qquad (2.14)$$

Similarly, the variance of temperature may be described by

$$\left(\frac{\Delta T}{T}\right)^2 = \left(\frac{\Delta H}{H}\right)^2 + \left(\frac{\Delta \overline{m}}{\overline{m}}\right)^2 + 2\rho_{MN}\left(\frac{\Delta n}{n}\right)\left(\frac{\Delta \overline{m}}{\overline{m}}\right)$$

$$+ 2\rho_{MN}\left(\frac{\Delta \text{ grad } n}{\text{grad } n}\right)\left(\frac{\Delta \overline{m}}{\overline{m}}\right) \qquad (2.15)$$

wherein ρ_{MN} and ρ_{MN}' define the correlation constants of density and molecular weight and of density gradient and molecular weight, respectively.

In the evaluation of variance of the height profile of an atmospheric parameter by Eqs. 2.12, 2.13, 2.14 and 2.15, account must be taken of the reduction of variation resulting from smoothing of data of a number of points. For example, if data from N points of mean value M and standard deviation $\sigma = (\text{variance})^{\frac{1}{2}}$ are smoothed, the uncertainty $\left(\frac{\Delta P}{P}\right)$ of the smoothed parameter P may be estimated to be the standard fractional error, that is

$$\frac{\Delta P}{P} = \frac{\sigma}{M\sqrt{N}} \qquad (2.16)$$

33

In the selection of wavebands which may be usefully exploited for the determination of atmospheric parameters by observation of the absorption of solar radiation, it is helpful to consider the altitude at which the optical depth is unity for solar radiation in the waveband of interest; that is to say, the altitude h at which, by Eq. 2.7,

$$\Delta \ln E = \int_{h}^{\infty} \bar{\sigma}(z) n(z) F(z) dz = 1 \qquad (2.17)$$

To approximate the altitude h, one may take an approximation to the density height profile, as in Fig. 8, which is the basis for Hinteregger's (1964) data to be cited below. The density profile of Fig. 8 implies the column density $N = \int_{h}^{\infty} n \, dh$ profile shown in Fig. 9, and the profiles of scale height, temperature and mean molecular mass shown in Fig. 10.
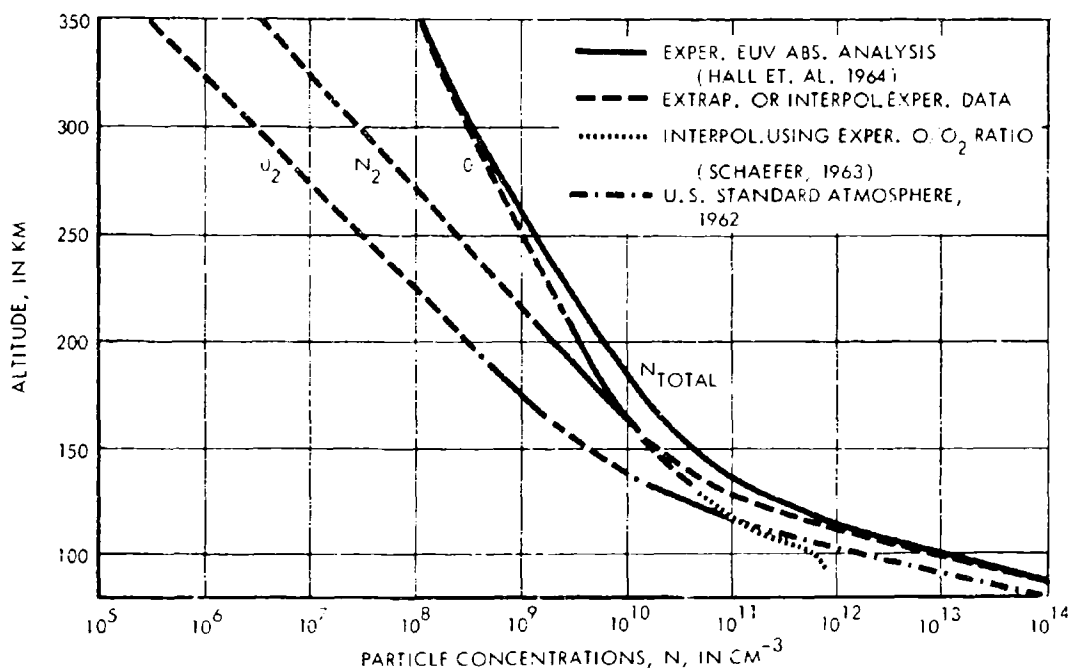
FIGURE 8. Neutral Constituents of Thermosphere Over White Sands, N.M.,
July 10, 1963, 10:00 A.M. (After H. E. Hinteregger et al., 1964)

34
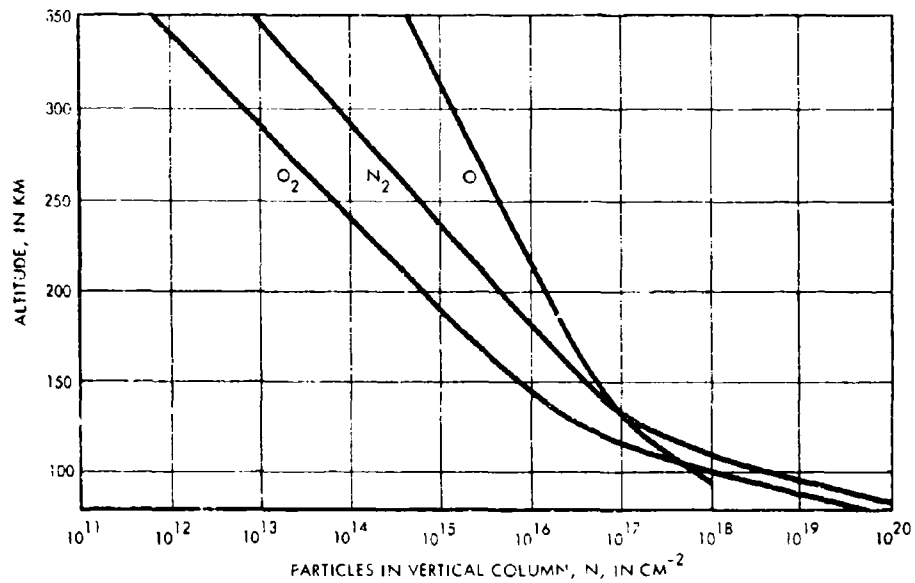
FIGURE 9.   Constituent Column Densities, $N = \int_{h}^{\infty} ndh$,

For July 10, 1963 Thermosphere (After H. E. Hinteregger et al., 1964)
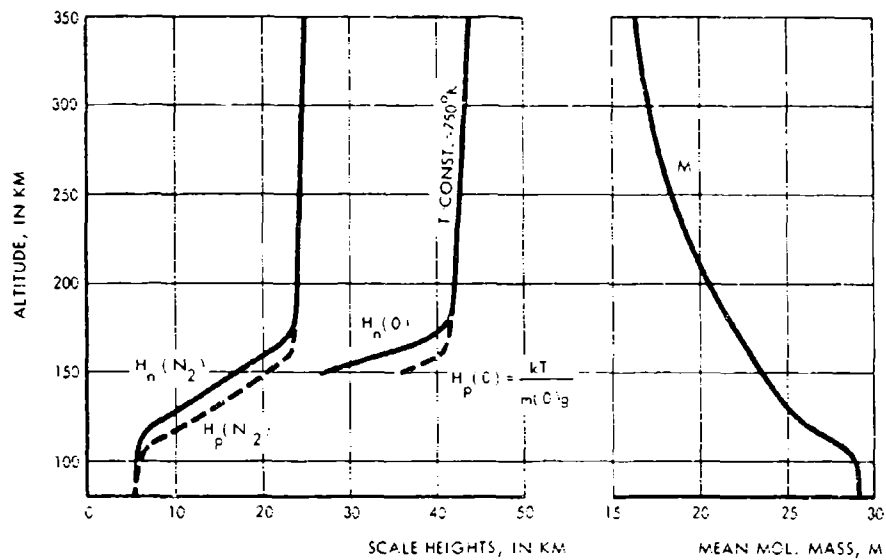
FIGURE 10.   Scale Heights and Mean Molecular Mass of July 10, 1963
Thermosphere Model (After H. E. Hinteregger et al., 1964)

As shown by Swider (1964), the Chapman function from a satellite at altitude 200 km, observing the solar radiation passing through a tangent height of 60 to 200 km, takes values from about 30 to about 90.

The absorption cross sections, for the principal constituents of the atmosphere in the altitude region 60 to 200 km (e.g., O, O_2, and N_2) are summarized for wavelengths 1 to 2000 A in Fig. 11 from data published by Hinteregger, et al. (1964).

The following are examples of diagnostic wavebands, for which computations of effective optical depth are given in Table 7. Shown in Fig. 12 is the absorption of solar flux in the bands 10 - 20 A, near the Hydrogen Lyman Alpha (1215.7 A) line, and in the Schumann-Runge continuum (1375 - 1500 A). The first of these absorbs each of the three principal constituents O, O_2, and N_2. Under the assumption that near the turbopause diffusion has not appreciably affected the proportions of oxygen and nitrogen, the one waveband alone is diagnostic of the neutral particle density in the region 105-135 km. The latter two are diagnostic only of the density of molecular oxygen (O_2), to cover the region 80 - 115 km and 125 - 145 km, respectively. The data of Fig. 12 were determined at Eglin, Florida (Lat. 30 A^0N at 0709.59 CST on 21 February 1966. Zenith angle was 83^0, and Chapman function F ~ 7.6. Measured from a satellite, the altitudes for which the three examples are diagnostic may be perhaps two scale heights higher, or for total particles (N_2, O_2 and O), the 10 - 20 A band is diagnostic in the altitude range 130 - 160 km, and for O_2 the ultra-violet bands are diagnostic in the altitude range from about 98 km to the turbopause near 112 km and from about 152 to 198 km, respectively.

A waveband that is diagnostic of O_2 alone at altitude perhaps two scale heights above that of the Schumann-Runge continuum is that encompassing the line of Hydrogen Lyman Beta (1025.7 A). Absorption of H Ly β in vertical incidence has been described by L. A. Hall et al., 1963, as in Fig. 14.
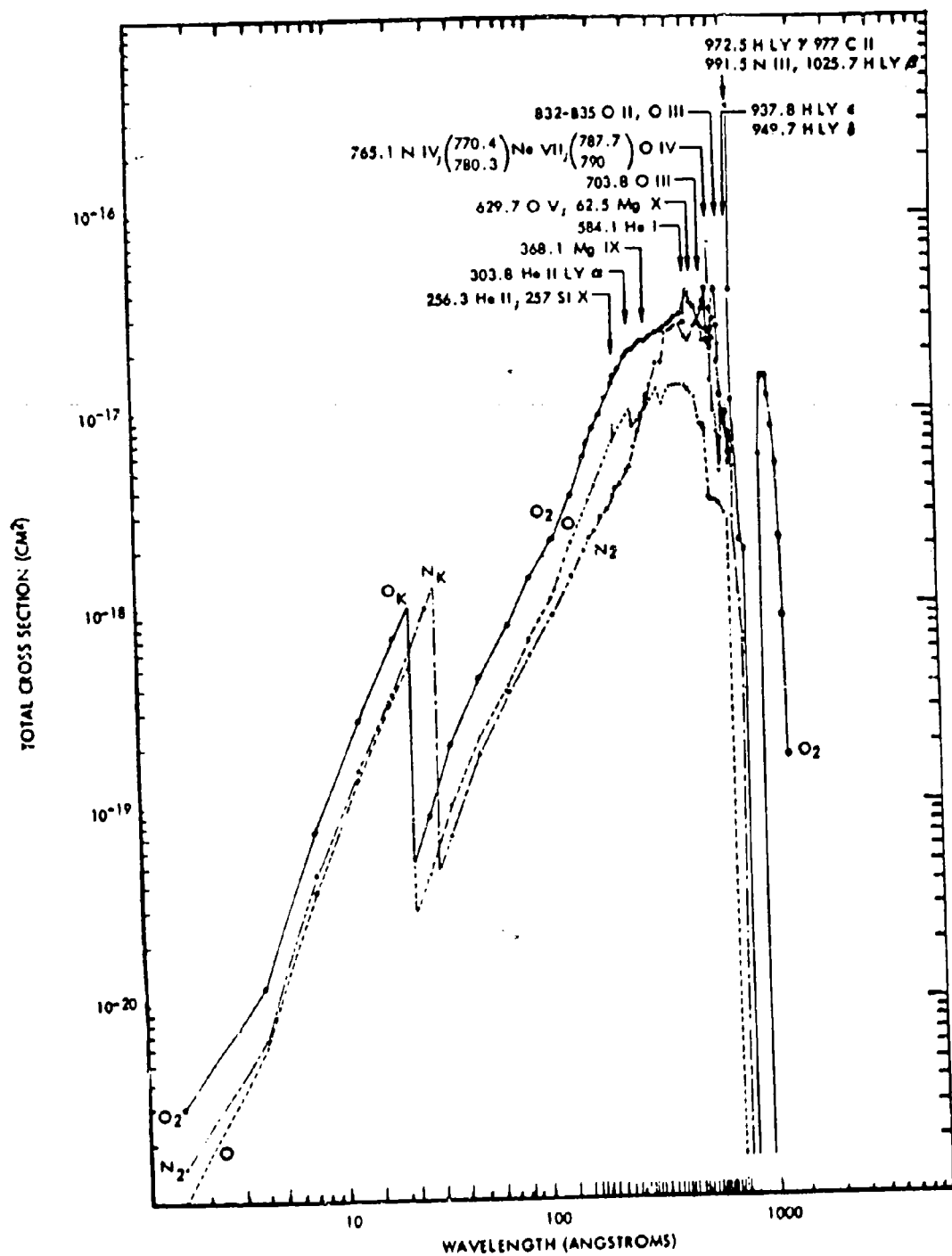
FIGURE 11. Absorption Cross Section of O, O_2, and N_2 (After Hinteregger et al., 1964)

TABLE 7. ABSORPTION OPTICAL DEPTHS OF EUV AND X-RAY WAVEBANDS

	Constituent	Absorption Cross Section 10^{-18} cm^2		At Z = 90 km		At Z = 120 km		At Z = 150 km		At Z = 180 km		At Z = 200 km		At Z = 250 km		
				$\int N(Z)dz$	$\sigma\int N(Z)dz$	$\int N(Z)dz$	$\sigma\int N(Z)dz$	$\int N(Z)dz$	$\sigma\int N(Z)dz$	$\int N(Z)dz$	$\sigma\int N(Z)dz$	$\int N(Z)dz$	$\sigma\int N(Z)dz$	$\int N(Z)dz$	$\sigma\int N(Z)dz$	
1375-14[illegible] Å (Schumann-Runge Continuum)	[illegible] [illegible] N[illegible]	0 14.3 0	$\sigma\int N(Z)dz$	-- 5E1[illegible] 2.5E19	0 71.5 0 71.5	1.5E17 6E16 4E17	0 8.6E-1 0 8.6E-1	5E16 8E15 4E16	0 1.[illegible]E-1 0 1.[illegible]E-1	1.7E15	2.4E-2 2.4E-2					Unity Optical Depth @ 12[illegible] km
			$F_{(Z)}$		76		76		37		36					
			$\sigma F\int N(Z)dz$		54[illegible]		65		4.5		0.[illegible]7					
[illegible] Å ([illegible])	[illegible] [illegible] N[illegible]	[illegible] [illegible] [illegible]	$\sigma\int N(Z)dz$	-- 5E18 2.5E19	0 1E-1 0 1E-1	1.5E17 6E16 4E17	0 1.2E-3 0 1.2E-3									Unity Optical Depth @ 1[illegible] km
			$F_{(Z)}$		76		76									
			$\sigma F\int N(Z)dz$		7.6		.091									
[illegible] Å ([illegible])	[illegible] [illegible] N[illegible]	[illegible] 1.6 0	$\sigma\int N(Z)dz$	-- 5E18 2.5E19	0 6.0 0 6.0	1.5E17 6E16 4E17	0 1.0 0 1.0	5E16 8E15 4E16	0 1.28E-2 0 1.28E-2							Unity Optical Depth @ 1[illegible] km
			$F_{(Z)}$		76		76		37							
			$\sigma F\int N(Z)dz$		456		76		0.47							
[illegible]	[illegible] [illegible] N[illegible]	[illegible] [illegible] [illegible]	$\sigma\int N(Z)dz$					5E16 7E15 4E16	1.65E-1 2.3E-1 1.12 1.515			1.5E16 6E14 4.5E15	5E-2 1.06E-2 1.26E-1 1.97E-1	4.5E15 7E13 6E14	1.4[illegible] 2.3E-3 1.65E-2 2.0[illegible]E-2	Unity Optical Depth @ 2[illegible] km
			$F_{(Z)}$						37				20		20	
			$\sigma F\int N(Z)dz$						56				4		0.41	
[illegible]	[illegible] [illegible] N[illegible]	[illegible] [illegible] [illegible]	$\sigma\int N(Z)dz$					5E16 7E15 4E16	1.65E-1 1.96E-1 3.3E-1 [illegible].51E-1			1.5E16 6E14 4.5E15	5E-2 1.7E-2 4.3E-2 [illegible]	4.5E15 7E13 6E14	1.48 1.95E-3 5.9E-3 [illegible]	Unity Optical Depth @ 2[illegible] km
			$F_{(Z)}$						37				20		20	
			$\sigma F\int N(Z)dz$						26				2.2		0.451	
[illegible]	[illegible] [illegible] N[illegible]	[illegible] [illegible] [illegible]	$\sigma\int N(Z)dz$					5E16 7E15 4E16	6.5E-1 2.05E-1 9.2E-1 1.78			1.5E16 6E14 4.5E15	1.35E-1 1.74E-2 1.14E-1 3.16E-1	4.5E15 7E13 6E14	5.6E-2 2.35E-3 1.38E-2 [illegible]38E-2	Unity Optical Depth @ 2[illegible] km
			$F_{(Z)}$						37				20		20	
			$\sigma F\int N(Z)dz$						66				6.3		1.47	
[illegible]	[illegible] [illegible] [illegible]	[illegible] [illegible]	$\sigma\int N(Z)dz$					[illegible] 7E15 4E16	[illegible] 1.5E-2 4.5E-2 1.11			1.5E16 6E14 4.5E15	1.64E-1 1.3E-2 5.1E-2 0.22	4.5E15 7E13 6E14	4.5E-2 1.5E-3 6.8E-3 5.41E-2	Unity Optical Depth @ 2[illegible] km
			$F_{(Z)}$						37				20		20	
			$\sigma F\int N(Z)dz$						41				4.4		1.1	
[illegible]	[illegible] [illegible]	[illegible] 14.4 1.9	$\sigma\int N(Z)dz$					5E16 7E15 4E16	3.5E-1 1.01E-1 1.5E-1 0.6			1.5E16 6E14 4.5E15	1.08E-1 8.6E-3 1.7E-2 1.36E-1	4.5E15 7E13 6E14	3.2E-2 1.01E-3 2.3E-3 3.5E-2	Unity Optical Depth @ 2[illegible] km
			$F_{(Z)}$						37				20		20	
			$\sigma F\int N(Z)dz$						22				2.69		0.7	
[illegible]	[illegible] [illegible]	[illegible]47 0.09 [illegible]	$\sigma\int N(Z)dz$					5E16 7E15 4E16	2.2[illegible] 6.3E-4 4.0E-2 4.29E-2			1.5E16 6E14 4.5E15	6.75E-4 5.4E-5 4.5E-3 5.17E-3	4.5E15 7E13 6E14	2.[illegible]E-4 6.3E-6 6E-4 8.13E-4	Unity Optical Depth @ 175 km
			$F_{(Z)}$						37				20		20	
			$\sigma F\int N(Z)dz$						1.6				0.103		1.6E-2	
[illegible]	[illegible]	0.155 0.2[illegible] 0.15	$\sigma\int N(Z)dz$	-- 5E18 2.5E19	large 1.15 1.7 large	1.5E17 6E16 4E17	2.07E-2 1.6E-2 6.02E-2 9.6E-2	5E15 8E15 4E16	6.7E-3 2.5E-3 6.0E-3 1.40E-2							Unity Optical Depth @ 14[illegible] km
			$F_{(Z)}$		76		76		37							
			$\sigma F\int N(Z)dz$		large		7.3		0.55							

FIGURE 12. Absorption of Solar Flux as Measured From Rocket NC 7.181 at
0709.59 CST, 21 February 1966, Eglin, Florida

The absorption cross section by O_2 for H Ly β, $\sigma_{O_2} \simeq 1.6(10)^{-18}$
cm^2; by O and by N_2, the absorption cross section is negligibly
small. From a satellite, the H Ly β is diagnostic of the density
of O_2 in a region about three scale heights above that shown in
Fig. 13, or from about 130 to 160 km. Density solutions obtained
simultaneously from measurements of the absorption of 10 - 20 A and
H Ly Beta yield, if diffusive separation is assumed negligible, the
height distribution of N_2, O_2 and O in the altitude range 130 to
160 km.

PHOTON FLUXES, $\Phi(\lambda, \Delta\lambda, h)$ IN PH CM^{-2}SEC^{-1}
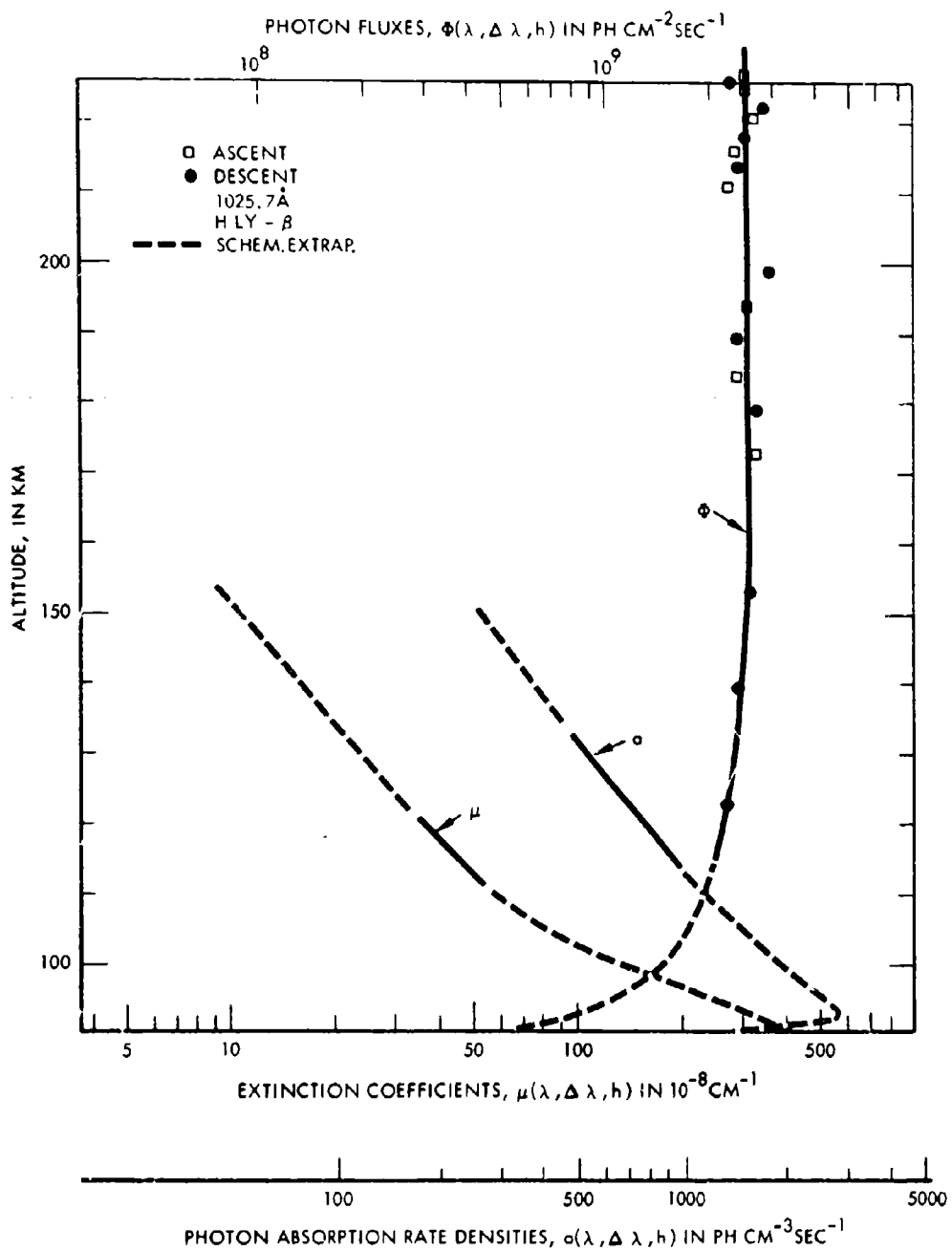
FIGURE 13. Flux, Extinction Coefficient, and Absorption of H Ly B 1025.7 A (After L. A. Hall et al., 1962)

In the same altitude range for which the Schumann-Runge continuum
is diagnostic for O_2, the absorption of 23 - 30 A radiation is ab-
sorbed by both N_2 and O_2. Here again, if it can be assumed that dif-
fusive separation is negligible, density solutions obtained simul-
taneously from measurements of the two bands yield the height distri-
bution of N_2, O_2 and O. The assumption of negligible diffusive
separation is a weak one, as may be seen by inspection of Fig. 8.

In the altitude range 217 to 248 km, simultaneous density solu-
tions from measurements of the absorption of the lines at 787.7A(O IV),
790A(O IV) and 256.3 A (He II) may be used to determine unambiguously
the height distributions of N_2, O_2 and O. Also in the altitude range
237 to 263 km, simultaneous density solutions from measurements of
the absorption of the lines at 256.3 A (He II), 368.1 A (Mg IX), and
584.3 A (He I) may be used to determine the height distributions of
N_2, O_2 and O. Probably representative of such measurements are the
experimental data reported by L.A. Hall et al. (1962) as described
in Fig. 14 for vertically incident 790 A radiation and in Fig. 15
for vertically incident 368.1 A radiation.

Summarized in Fig. 16 are the altitude regions for which the
density-height distribution of principal atmospheric constituents
may be determined. In these same regions, by use of the temperature-
density relation of Eq. 2.11, the temperature-height distribution may
also be determined.

DETECTOR CHARACTERISTICS

The detectors described by L.A. Hall et al. (1962) as employed
by H. E. Hinteregger and his group at AFCRL for measurements in the
region of wavelength 250 to 1300 A are monochromaters equipped with
a 2 meter concave grating of 7500 lines per inch and an entrance
slit of width 50 microns. The angle of incidence of radiation on
the grating is 86 degrees. The narrowest slit employed was 0.75 mm
wide, with foreshortened width of 53 microns at the short wavelength
end of the scan, and about 100 microns at the long wavelength end.
The wavelength increments covered by the slit were 1.5 A and 3 A at

PHOTON FLUXES, $\Phi(\lambda, \Delta\lambda, h)$, IN PH CM^{-2}SEC^{-1}
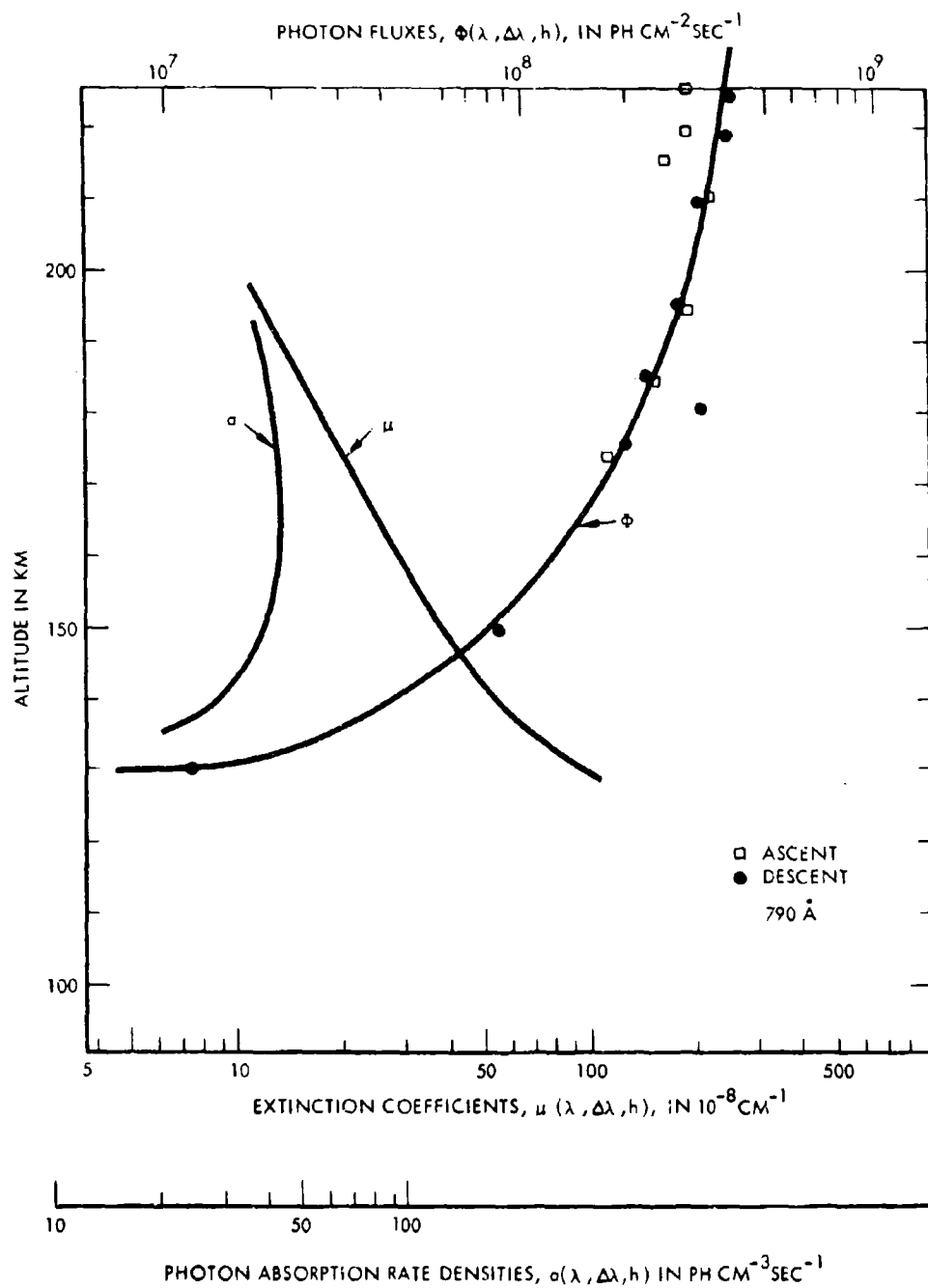
FIGURE 14. Flux, Extinction Coefficients, and Absorption at 790 A
(After L. A. Hall et al., 1962)
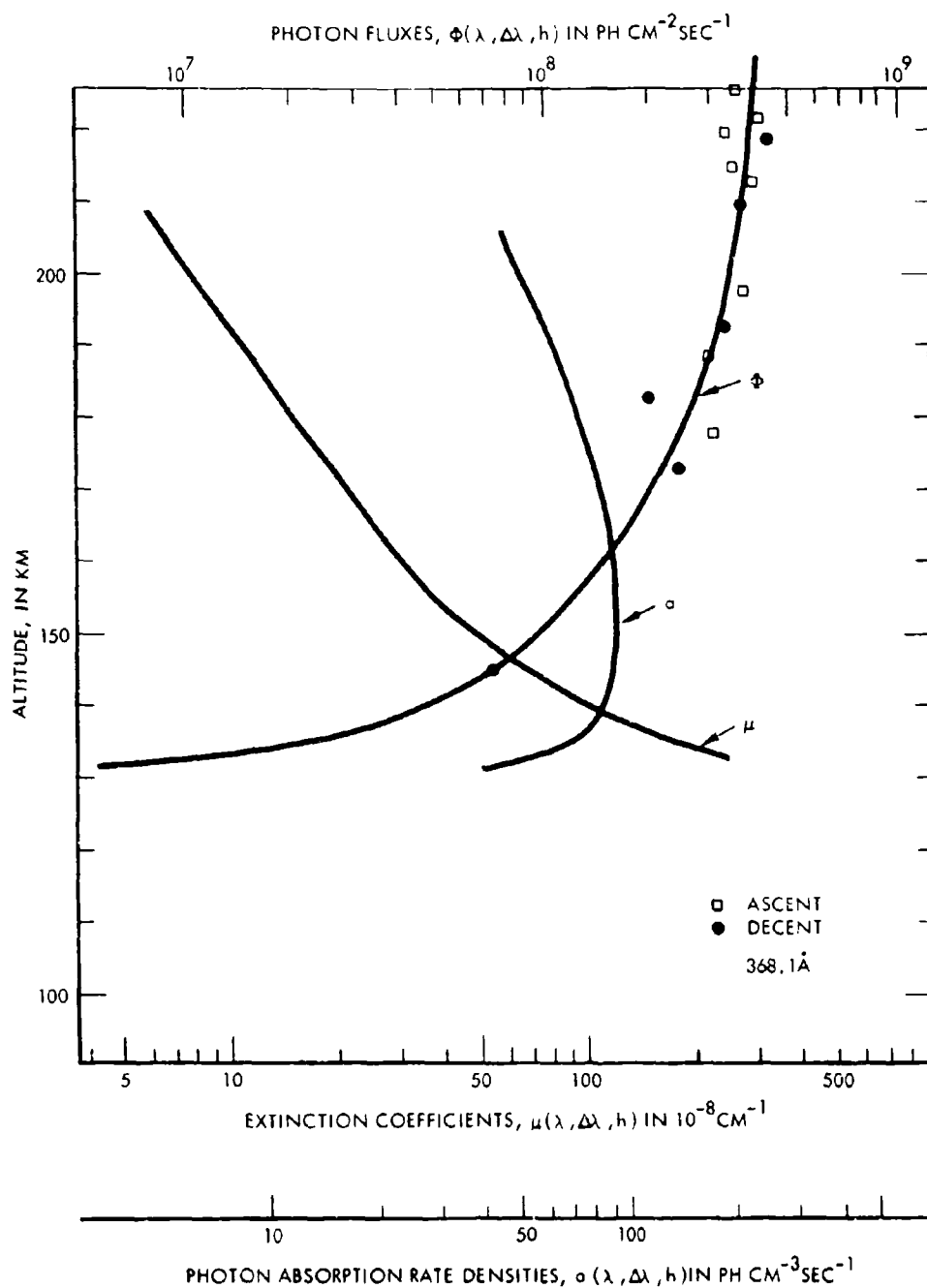
FIGURE 15. Flux, Extinction Coefficients, and Absorption at 368.1 A
(After L. A. Hall et al., 1962)
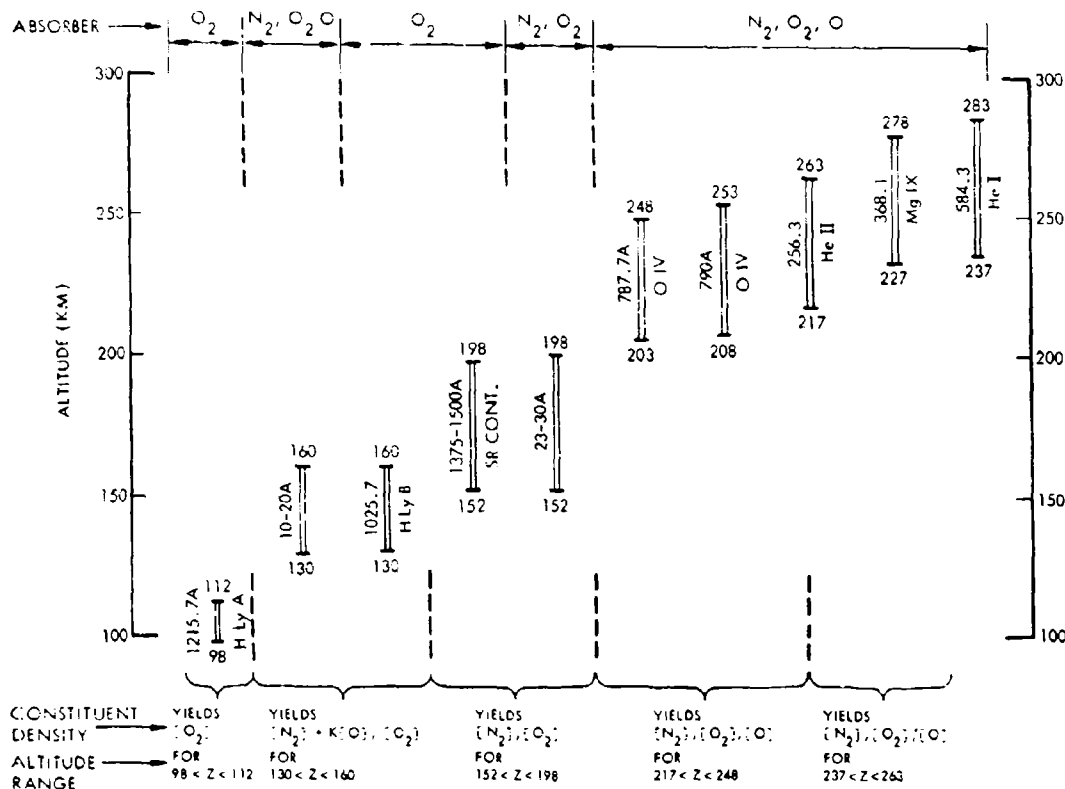
FIGURE 16. Density by Atmospheric Absorption of Solar Radiation

the short and long wavelength limits, respectively. Dispersed radia-
tion passing through the exit slit in any position was intercepted
by a photomultiplier with a 3.5 inch long semiconductive cathode.
The photomultiplier output was input to a pulse amplifier to counting
circuits, with overall gain so adjusted that a variation in gain over
a factor two would cause a change in counting rate of only 5 percent.
The count accumulation was read out continuously in 32 steps in the
0 to 5 volt d.c. range of the telemetry. Readability of the flight
record had a high speed upper limit of two megacycles. However,
since the chosen entrance slit height of 8 mm limited the expected
counting rate for the H_e II resonance line to about 5 $(10)^4$ sec^{-1},
dead-time corrections were not required for most of the observed
counting rates, with the exception of the Hydrogen Lyman alpha line

with counting rate $2.7 (10)^5$ sec^{-1}. Hall et al. (1962) estimate that the "estimated error" of the absolute photoelectric yield of the tungsten reference electrode is ±10% in the wavelength range 536 to 1216 A, and ±15% to ±25% in the range 250 to 536 A. The "estimated error" in quantitative comparison of the response of different rocket instruments is much smaller than the errors listed above.

An alternative to the grating monochromator and photocell combination described above is the use of narrow-band photon-counters or ionization chambers. The technique of preparing such detectors has been described by Chubb and Friedman (1955) and by Grobecker (1967).

The described ion chambers, typically, have an outside diameter of 1 inch and are 1½ inches long. Each chamber has an end window acting to filter out short wavelength radiation, and each has a gas filling. The ionizing potential of the gas filling sets the upper limit of the detector's wavelength response. Windows for narrow-band ion chambers in the soft x-ray region are made by coating Mylar film with sufficient thicknesses of metal and using the absorption characteristics of the filling gas as part of the window function. For windows of ion-chambers in the ultraviolet region, at wavelengths greater than 1200 A, solid crystals, such as LiF, BaF$_2$, etc. are used.

The fractional uncertainty of measurements of flux using ion-chambers is about the same as those made using monochromator and photocell combinations, approximately ten to twenty-five percent, as obtained by rocket borne measurements described by Grobecker (1969).

VEHICLE AND SYSTEM CONSIDERATIONS

The orbit characteristics of the satellite vehicle for the instruments used to measure the absorbed solar radiation may require a detailed study for optimization of coverage, spacing of profiles and the like. A notable distinction of the solar absorption measurements from the atmospheric emission measurements is that the former may be accomplished only over vertical profiles at each of two discrete

positions along the path of the satellite, as compared to a continuous
swathe along the orbit of the satellite making emission measurements.
Of course, both types of measurement may conceivably be made from
the same satellite vehicle; however, the data output of solar absorp-
tion profiles, not continuous along the orbit path, is much smaller
than that of atmospheric emission profiles.

An example of the coverage obtainable is illustrated in Fig. 17.
One set of five satellites having orbits (numbers 1 to 5 of the
figure) chosen to intersect the terminator with a large angle between
the orbit path and the terminator, at latitudes evenly spaced between
the equator and the pole, are launched with a common ascending node.
A second set of four satellites (numbers 6 to 9 inclusive in the
figure), are launched in orbits having similar inclinations, but
with a common ascending node displaced 90° from that of the first
set. If the satellite altitude is about 150 nmi (278 km), the period
is about 1½ hours. Since the satellite transits the terminator twice
in each orbit, each satellite measures absorption profiles at 32 loca-
tions per day. Such a combination of nine satellites yields density-
height profiles of one observation per day at a grid spacing of about
22°.

Simple geometric considerations lead to the following character-
istics of the volume of atmosphere probed by the technique. The
angle of the earth's horizon below the horizontal plane of a satellite
at altitude of 200 km is about 3 degrees. The path length from the
satellite to the point of earth tangency of the line of sight is
about 345 km. The distance subtended by the half degree diameter
of the sun at a distance of 345 km is about 2.75 km, which is the
approximate value of the vertical and meridional-horizontal dimensions
of the atmospheric volume observed. The dimension, in the earth-
sun line, of the observed atmospheric volume, or the path length
within one atmospheric scale height of the nominal tangent altitude,
is about 410 km. In short, the observations determine the average
density in a volume of the atmosphere which is about 345 km in the
direction from the satellite to the sun, and of dimensions about
410 km along the sun lines, and 2.75 km normal to the sun line.

46

JULY SOLSTICE TERMINATOR   JAN SOLSTICE TERMINATOR

NP

SP
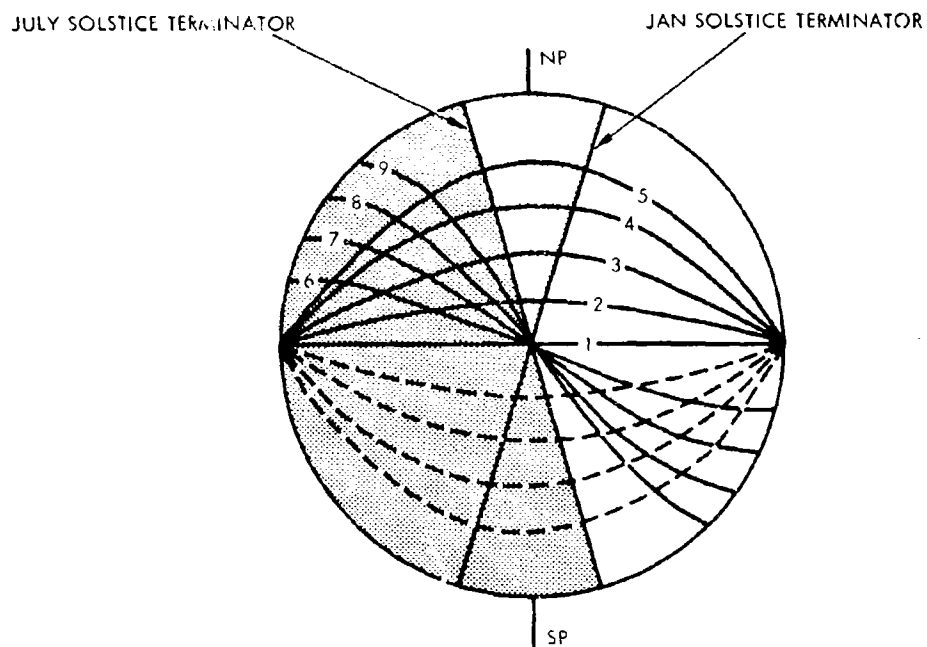
FIGURE 17. Satellite Orbit Intersection with Effective Solar-Terrestrial Terminator

SUMMARY

In summary, it has been shown that, by techniques of already demonstrated feasibility, the measurement from a satellite of solar radiations in the extreme ultraviolet and soft x-ray region may pr vide data for the determination of piecewise continuous vertical profiles of density of total particles, N_2, O_2 and atomic oxygen, (scale height and of temperature in the entire altitude range from about 100 to about 300 km. The uncertainty of such determinations of density is about 10 percent, adequate for some needs (i.e., satc lite orbit prediction), but inadequate for others.

47

OCCULTATION OF SATELLITE-TO-SATELLITE TRANSMISSION

A technique for the determination of density in the lower tropo-
sphere is the coherent microwave occultation system described by
B. Lusignan et al., 1968 and 1969, along the lines demonstrated by
NASA Mariner spacecraft in the measurements of the atmospheres of
Mars and Venus (A. Kliore et al., 1965 and 1967).

A characterization of the techniques is given in Fig. 18, which
summarizes considerations reviewed in the following paragraphs dealing
in turn with the basic theory, the estimates of error and system con-
siderations.

The occultation effects have been described by Lusignan et al.,
1969, in terms of a basic geometry illustrated in Fig. 19. Two satel-
lites in the same orbit are spaced so that the radio waves from one
to the other pass through the atmosphere. In the atmosphere the radio
waves propagate with a velocity given by

$$v = c/n \qquad (3.1)$$

where c is the speed of light in vacuum, and n, the refractive index
is given by

$$n = 1 + 10^{-6} N \qquad (3.2)$$

The refractive modulus N is proportional to the air density and water
vapor density, as described in Volume II, and given by the relation

$$N = 0.223 \, \rho_a + 0.334 \, \rho_w + 1.75(10)^3 \, \frac{\rho_w}{T} \qquad (3.3)$$

where ρ_a is the density of dry air in gm cm^{-3}, ρ_w is the density of
water vapor and T is the temperature in degrees Kelvin.

The changes in refractive index have two effects on the radio
waves: an apparent increase in path length due to retardation or

shortening of wavelength along the path and a bending of the path due to a gradient of the refractive index normal to the path. Both effects combine to give a path length between satellite that is longer than the free space path length.

PRINCIPLE OF OPERATION

- BENDING AND PHASE CHANGE OF MICROWAVE IN OCCULTING ATMOSPHERE = $f(\rho, T, X)$
- PATH LENGTH (X) DETERMINED BY GEOMETRY
- DETERMINES DENSITY (ρ) AND TEMPERATURE (T)

UNCERTAINTY OF MEASUREMENT (Theoretical, with no experimental authentication)

- DENSITY OF AIR: 0.1%
- DENSITY OF WATER VAPOR: 1%
- TEMPERATURE: 10%

COVERAGE IN VOLUME

- AVERAGE OVER VOLUME 500 KM x 1.3 KM x 150 M
- SEVEN SATELLITES IN GROUP DETERMINE DENSITY AT 6 ALTITUDES FROM 2.5 TO 20 KM
- TWENTY-ONE SATELLITES MAKE DAILY SAMPLE ON 1000 KM GRID

STATUS OF DEVELOPMENT

- SYSTEM SPECIFICATIONS STUDIED; ERRORS ESTIMATED
- EVALUATION OF COMPUTATIONAL REQUIREMENTS INCOMPLETE

RECOMMENDATIONS

- INVESTIGATE FEASIBILITY OF A 7-SATELLITE DEVELOPMENTAL EXPERIMENT TO MEET NEEDS OF NUMERICAL WEATHER PREDICTION, RADIO COMMUNICATION AND BALLISTIC WEAPON TARGETING. THIS MAY BE DONE BY CIVIL AGENCIES.

MICROWAVE SATELLITE-TO-SATELLITE OCCULTATION
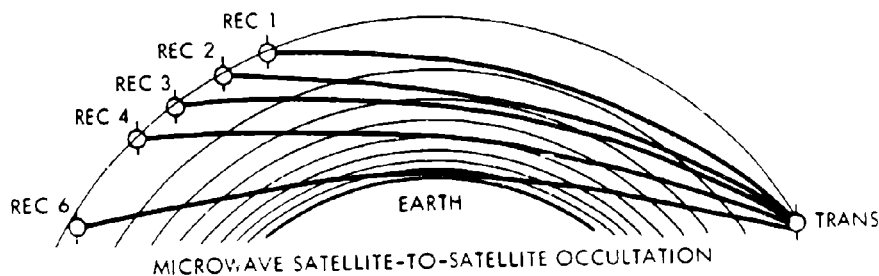
FIGURE 18.   Measurement of Microwave Satellite-to-Satellite Occultation for Density at 4-20 km

FIGURE 19. Basic Geometry of Occultation Measurement
(After B. Lusignan et al., 1969)

The mathematics of the inversion have been described in detail by G. Fjelbo and V. R. Eshleman (1968) and R. A. Phinney and D. L. Anderson (1968).
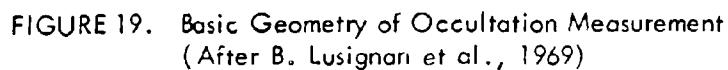
Lusignan et al.(1969) describe a computer ray tracing program based on Fermat's principle that the path followed by an electromagnetic ray through a refractive medium is such that the integral $\int nds$ is a minimum. Referring to Fig. 19, the integral equation for radius r, the distance from the earth's center to a point on the ray path, as a function of the angle θ_T, measured from the center of the ray path, is given by

$$r(\theta_r) = \int_0^{\theta_T} r(\theta) \left[\frac{r(\theta)\ n(r(\theta))}{r_t\ n_t} - 1 \right]^{\frac{1}{2}} d\theta \qquad (3.4)$$

where r_t is the altitude of the ray at the tangent point $\theta_T = 0$. Equation 3.4 is integrated by computer to determine the actual path.

61

The integral $\int nds$ along the path ds = $(r\,d\theta + dr)$ gives the total phase path length of the ray.

Lusignan et al.(1969) suggest that the experimental behavior may be crudely perceived from an analytical solution assuming spherical symmetry, small bending, and constant scale height in the atmosphere. The assumption of scale height implies that the density ρ is an exponential function of height h:

$$\rho = \rho_s \, e^{\frac{-h}{H}} \qquad (3.5)$$

Neglecting water vapor terms in Eq. 3.3, the refractive modulus N is

$$N = N_s e^{\frac{-h}{H}} \qquad (3.6)$$

where the subscript s implies a value at the earth's surface.

The following approximate equations follow from the assumptions:

Total bending angle
$$\epsilon(h) = (2 \times 10^{-6})N_s e^{-h/H}(\pi R/2H)^{\frac{1}{2}} \qquad (3.7)$$

Total excess path length
$$\emptyset(h) = \Delta R(h) + \Delta L(h) \qquad (3.8)$$

Excess path length due to retardation
$$\Delta R(h) = (2 \times 10^{-6})N_s e^{-h/H}(\pi RH/2)^{\frac{1}{2}} = H\epsilon(h) \qquad (3.9)$$

Excess path length due to bending
$$\Delta L(h) = R_a \epsilon^2(h)/4 \qquad (3.10)$$

Difference in altitudes of closest approach of bent and unbent rays
$$h - h_o = R_a \epsilon(h)/2 \qquad (3.11)$$

where

N_s = surface refractivity

R = distance from the earth's center to the ray

H = atmosphere's scale height

h_0 = closest approach of an unbent ray

h = closest approach of the bent ray

The radio system of the satellites measures the path length within about one half wavelength (or 3 cm). A continuous radio wave, transmitted from the master satellite to the repeater satellite, is retransmitted phase coherently back to the master where the received and originally transmitted frequencies are compared. A difference in transmitted and received frequencies is a "Doppler frequency," recorded on a counter in the master. Since at a frequency of 5 GHz, each wavelength is 6 cm long, the system has an uncertainty of one way path length of 3 cm. The total effective path length change is indicated as a function of altitude in Fig. 20, from which it may be inferred that the uncertainty of 3 cm represents a fractional uncertainty of $5(10)^{-5}$ near the surface to about $3(10)^{-3}$ at 20 km.

Measurement of a 3 MHz signal modulating the 5 GHz, with an uncertainty in phase of 4 degrees, yields a separate indication of one-way path length.

In passage through the atmosphere, the radio waves are influenced by the air in a volume indicated approximately in Fig. 21. The cross section normal to the ray path is determined by the Fresnel zone which in the horizontal direction has a dimension of about 1.3 km. In the vertical direction the gradient in the atmosphere, contributing to the change in path length, shrinks the effective Fresnel zone to about 150 meters. Along the path, the atmospheric effects decrease mainly as a result of the radio waves leaving the atmosphere, with
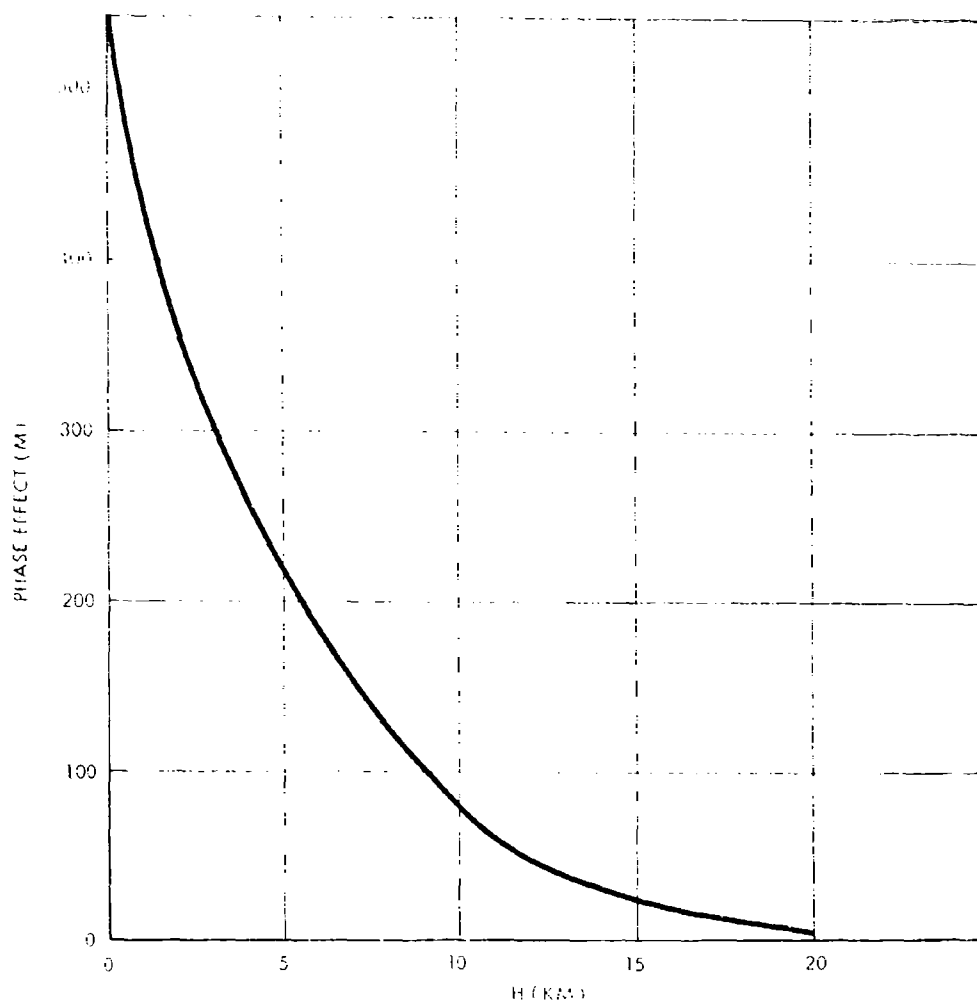
FIGURE 20. Path Length Change Versus Altitude (After B. Lusignan et al., 1969)
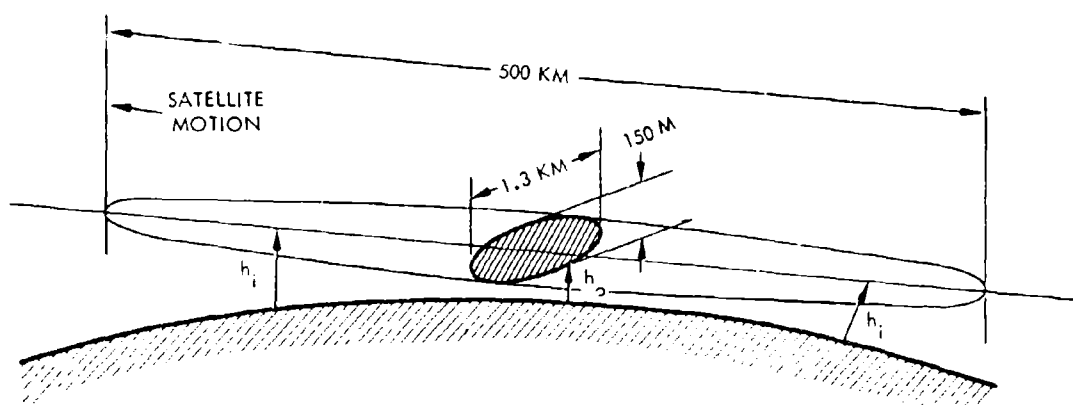
FIGURE 21. Volume Caused by Occultation (After B. Lusignan et al., 1969)

the result that 75% of the bending and retardation occur over a horizontal distance of 500 km.

As indicated roughly by Eqs. 3.7 to 3.11 inclusive, as the atmospheric pressure increases, the total path length, the bending angle and the altitude of closest approach also increase. For a given satellite spacing, Lusignan's (1969) ray tracing program is used in a recursive search procedure to find the ray that reaches the satellites. Once this ray is identified, its starting height is recorded and phase defect calculated. Figure 22 shows the total phase defect as a function of surface atmospheric pressure for several satellite spacing distances. For the illustration of Fig. 22, the pressure decays with altitude according to the scale height variation of a standard atmosphere. Figure 23 shows the height of closest approach of the same rays, satellite spacings and surface pressures.

Lusignan et al. (1969) have analyzed the specifications of the system to be sure that uncertainties are less than about 0.001 in absolute value of density. As yet, there has been no experimental authentication of Lusignan's theoretical error estimates.

Such fractional uncertainties translate to about 0.5 m in horizontal spacing and about 24 m in a vertical direction. The contributions to horizontal uncertainty are estimated on theoretical grounds by Lusignan et al. (1969) to be the following: measurement of phase defect, 0.05 m; ionospheric refraction negligible; radio oscillator instability negligible; air drag, 0.004 m; solar pressure, 0.2 m; orbit oblateness, 0.2 m; weather fluctuations averaged over one or two months, less than 0.5 m.

The contributions to vertical uncertainty are estimated to be: orbit period negligible; orbit oblateness, 0.02 m; eccentricity of orbit, less than 0.5 m; and oblateness of the earth's surface, less than 24 meters.

The oblateness of the earth's surface, known with uncertainty less than 24 meters, is such that mean sea level varies about 20 km from the spherical from the poles to the equator. In spacing of
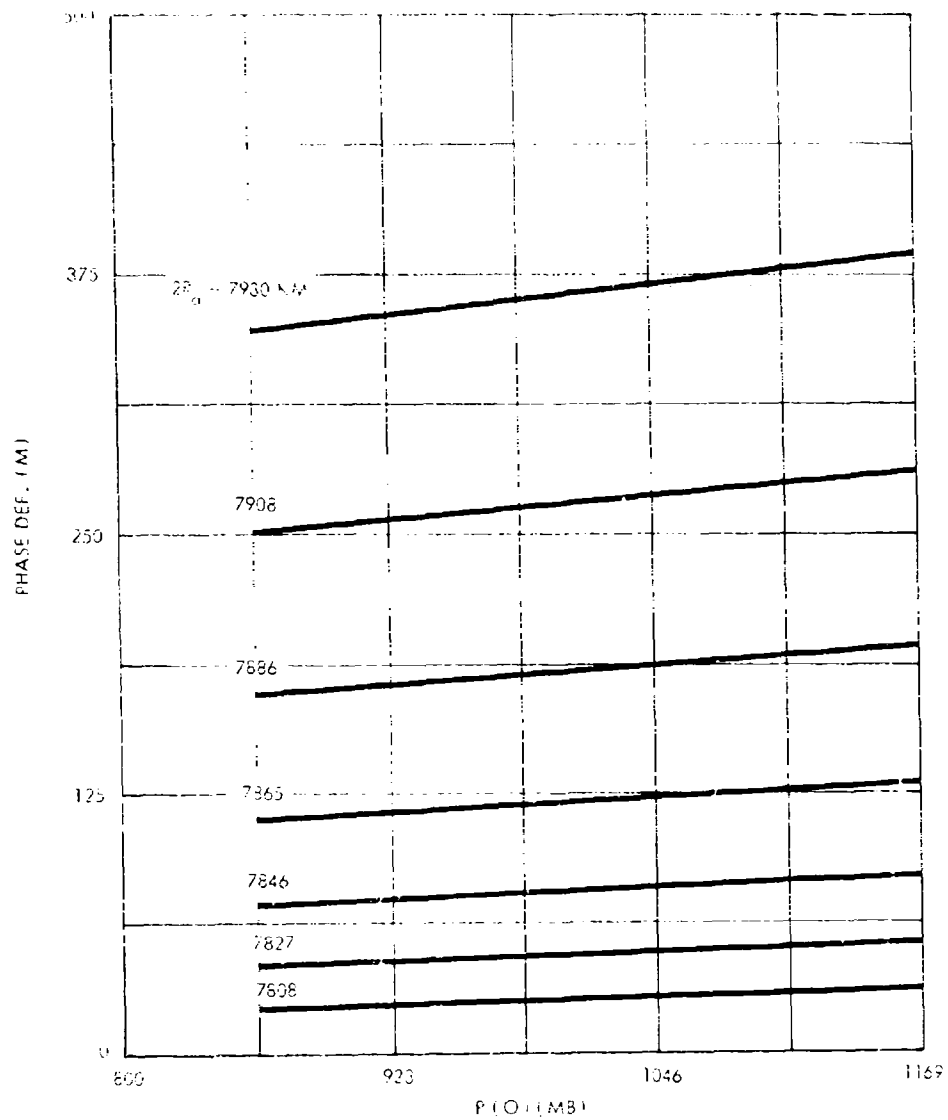
FIGURE 22. Phase Defect Versus Surface Pressure for Fixed Satellite Separations, Ra
(After B. Lusignan et al., 1969)
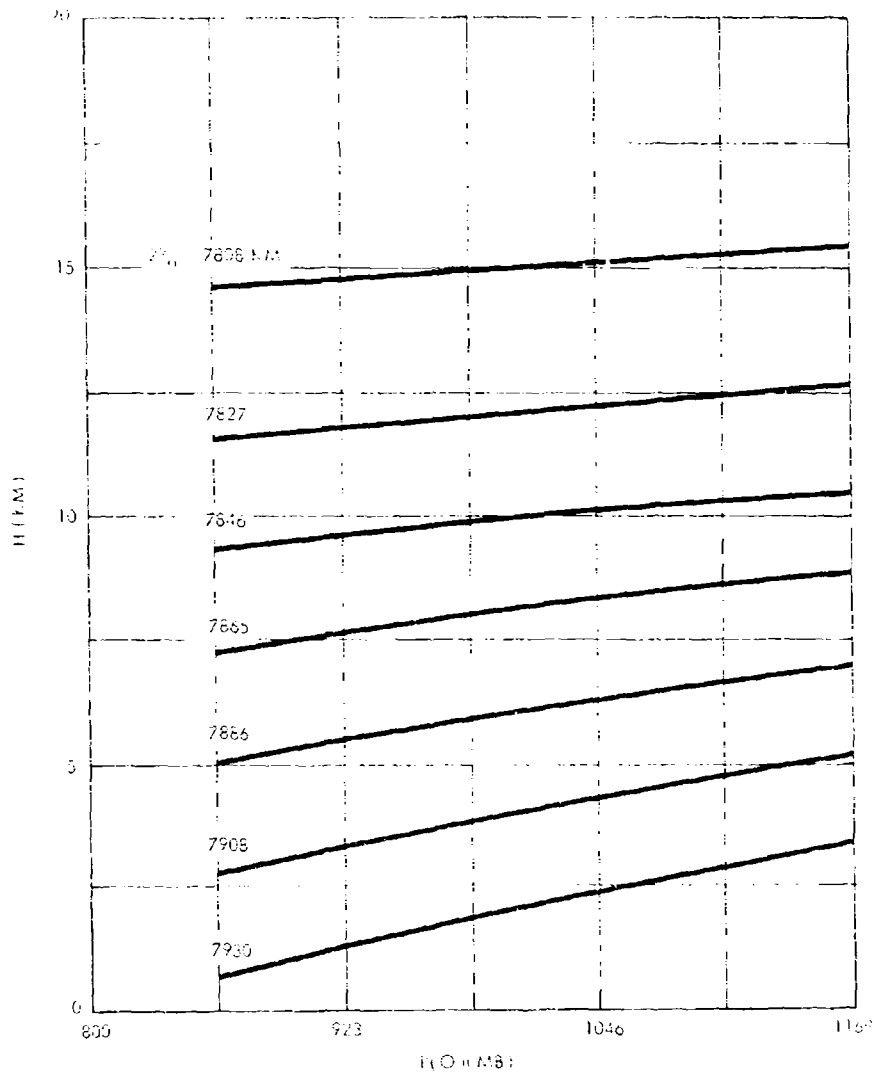
FIGURE 23.   Minimum Altitude Versus Surface Pressure for Fixed Satellite
Separations, Ra (After B. Lusignan et al., 1969)

several satellites, the oblateness must be considered so that the measurements may be made at a useful set of altitudes. Shown in Fig. 24 is the variation in minimum altitude measured from sea level of each of a set of six satellites which pass from pole to equator. Set 1, spaced to keep its rays above the atmosphere, suffers the full 20 km variation. For rays in the atmosphere, the decreasing altitude of the wider spacing is offset by increased bending and rise in ray altitude, so that variations from pole to equator for sets 2 to 6 are only 5 to 10 km.

The precise tracking information is derived by measurements between the individual satellites, not from ground tracking systems which have additional sources of error. However, determination of the absolute ground projected position of each pair of satellites depends upon ground tracking, with uncertainty of several kilometers acceptable for the needs of numerical weather prediction.

The effect of water vapor in the lower troposphere, given analytically by Eq. 3.3, is shown in the example of Fig. 25. The total refractive modulus of dry air is . wn as function of altitude, as well as that of an atmosphere with the partial pressure, of water vapor at the surface, of 10.2 m bars. While water droplets in clouds considerably attenuate radio waves, they add less than 1 N unit to the refractive modulus at altitudes 2 km and above and consequently do not seriously affect the phase path length.

The iter vapor content of the atmosphere may be sensed by a second occultation frequency at an exact multiple of the primary 5 GHz signal near the water vapor absorption near 20 GHz. Whether the 20 GHz signal has a different refractive index and consequently a different phase path, than the 5 GHz signal is currently being evaluated.

Water vapor may affect the occultation system by offering multiple paths for rays between satellites, with scintillations strong enough to disrupt the phase lock of the satellite receivers.
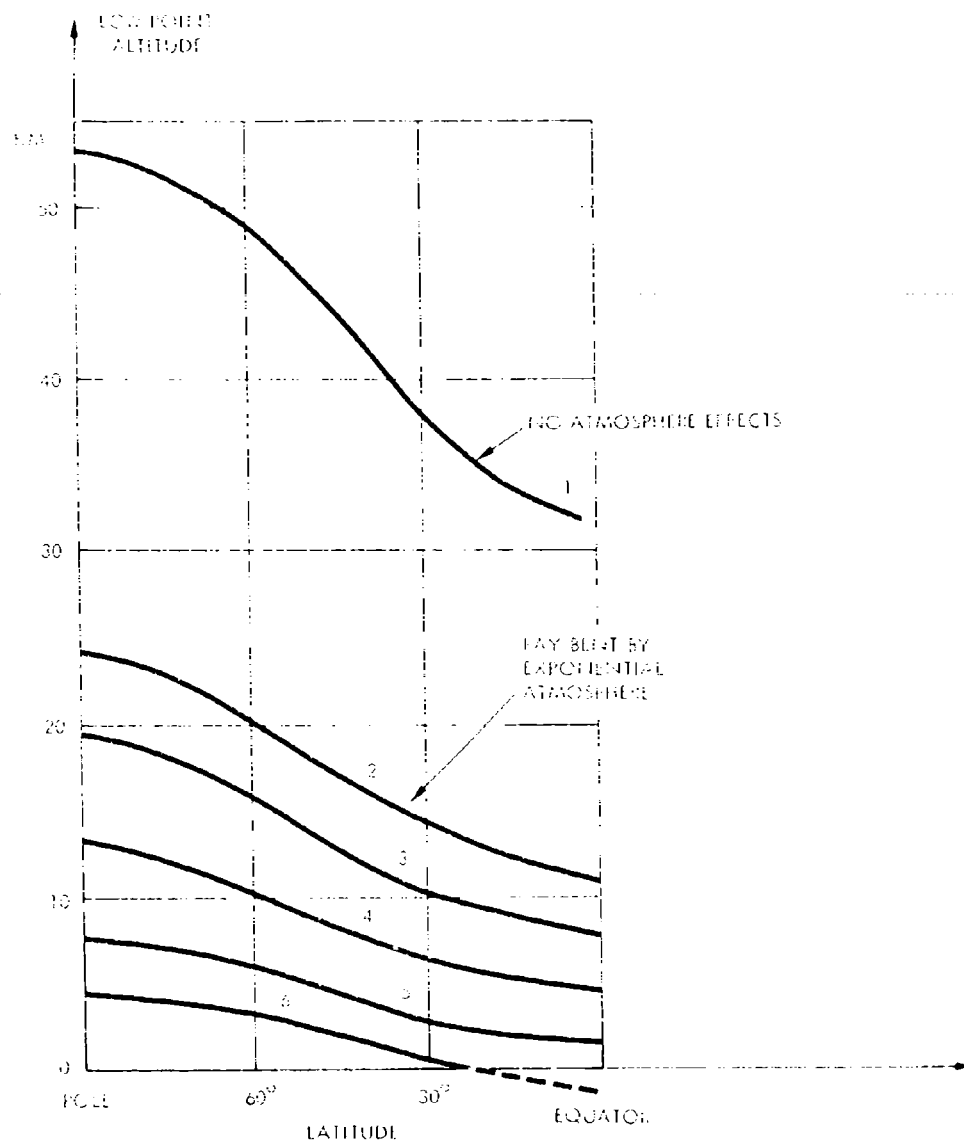
FIGURE 24. Variation of Ray Altitudes with Latitude
(After B. Lusignan et al., 1969)

It is expected that scintillation errors of this kind will affect
only rays in the lowest 2 km of the atmosphere.
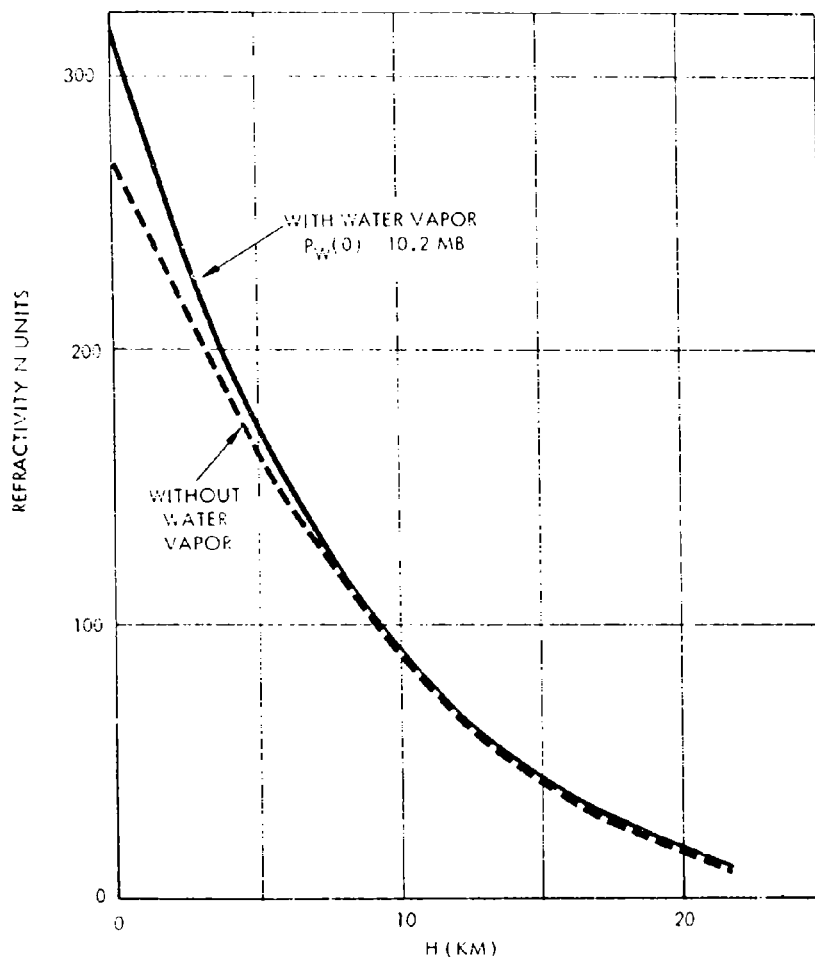
FIGURE 25. Total Refractivity as a Function of Altitude
(After B. Lusignan et al., 1969)

Radio systems, penetrating the clouds, have potential for sup-
plying meteorological data not available from visual and infrared sys-
tems. In Fig. 26 is shown the average occurrence of clouds at various
altitudes between latitudes 41° and 77° over Russia during the years

1959-1963 (R. T. Hall, 1968). Also plotted in Fig. 26 is the capability of the microwave occultation system, anticipated by Lusignan et al. (1969), clearly effective from 20 km down to 5 km and possibly obtainable with correction for water vapor as low as 2.5 km.
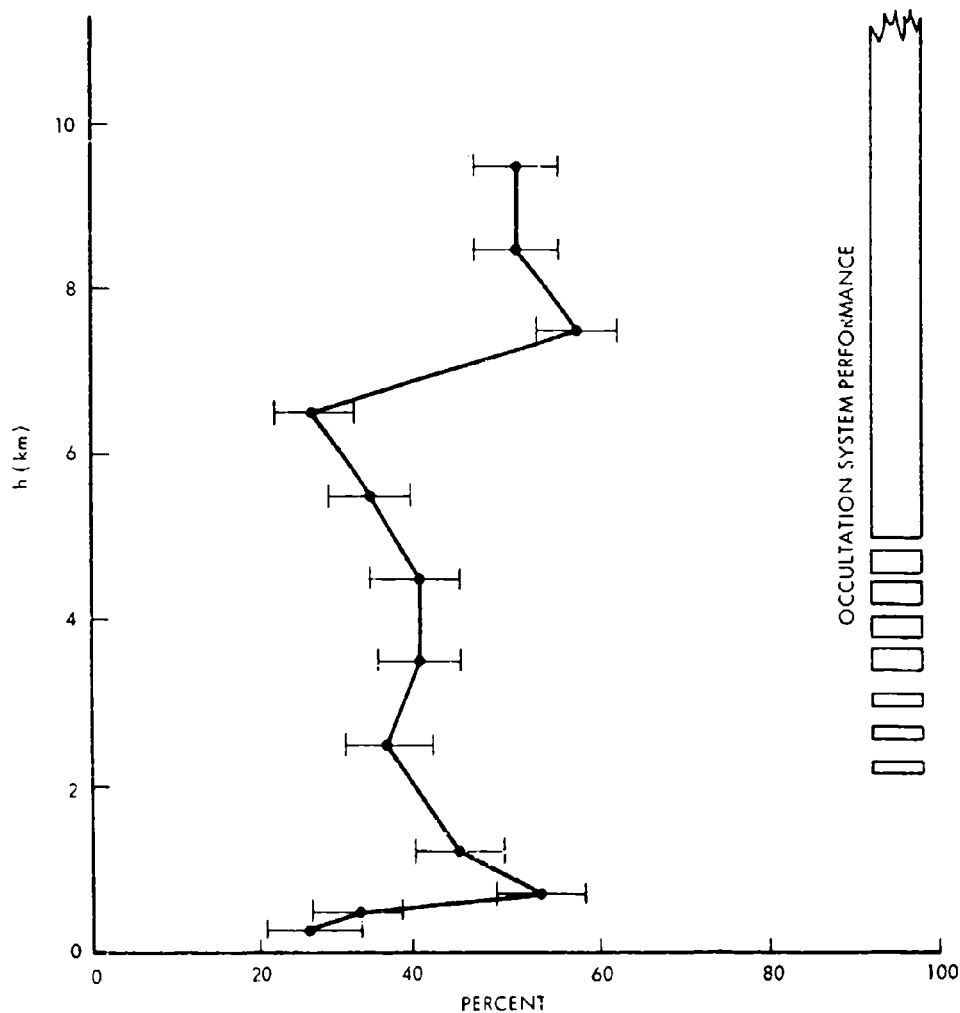
FIGURE 26. Probability of Clouds Versus Altitude
(After B. Lusignan et al., 1969)

In Fig. 27 is shown the grid of vertical samples obtainable each twelve hours with three occultations systems, each consisting of a master and six repeaters (Lusignan et al., 1969).

40°N

GRID
TIME = 30 SEC

SCALE

0   1000 MILES

1000   KM

EAST-WEST
GRID SPACING

KM

1000

800

600

400

200

POLE   60°   30°   EQUATOR
                    LATITUDE
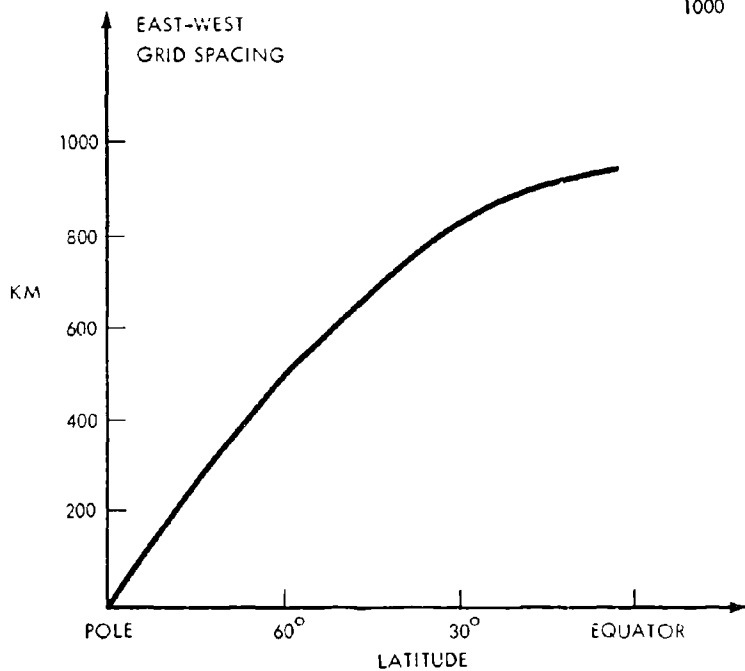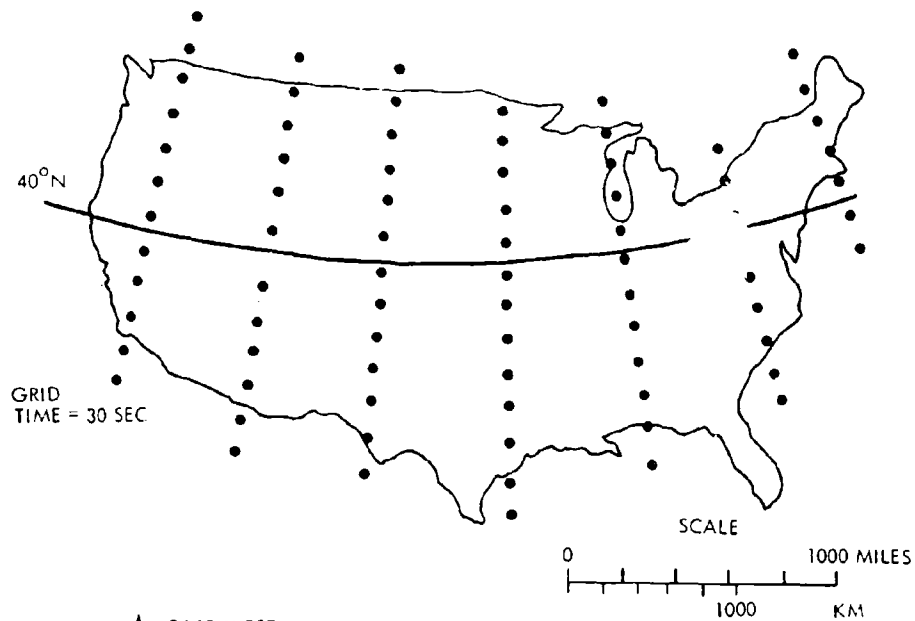
FIGURE 27.   Grid Spacing with Occultation Satellite
                    (After B. Lusignan et al., 1969)

62

In summary, a pair of satellites in the same earth orbit, but separated about 60° in phase will have a radio path between them that intersects the atmosphere continuously. With a coherent transponder between satellites at a frequency of 5 GHz, changes of 3 cm in the phase path can be recorded, giving theoretically a sensitivity to changes in atmospheric density of better than 0.001 in fractional uncertainty of density. With a set of seven polar orbiting satellites to sense density at five levels in an altitude range 2.5 to 20 km, in each of three systems, samples of density may be taken over a horizontal worldwide grid of spacing less than 1000 km, twice daily.

SATELLITE DECELERATION

The effect of aerodynamic drag on the orbit characteristics of satellites becomes important for military applications that require orbits with a low perigee altitude (say, 100 nmi). The aerodynamic drag at satellite velocities at such altitudes has a significant effect on the life of the satellite in orbit, which can be expressed as a function of the ballistic parameter of the satellite $(w/C_D A)$, the orbit eccentricity, and the perigee altitude. For a typical orbit eccentricity of 5×10^{-2} and a given ballistic parameter, the life of the satellite in orbit decreases by nearly three orders of magnitude as the perigee altitude drops from 400 nmi (i.e., TIROS satellite) to 100 nmi. This drastic effect of aerodynamic drag on the life of satellites at low altitudes has also important implications when determining the position of a satellite in low altitude orbit.

Measurement of the deceleration of the satellite by means of accelerometers within the satellite itself is a technique for in situ determination of atmospheric density at satellite altitudes. Characterization of the technique is given in Fig. 28 which summarizes considerations discussed in the following paragraphs.

The aerodynamic drag force on the surface of the satellite (D) is a function of the ambient density (ρ), the satellite velocity relative to the ambient medium (V_s), the drag coefficient of the satellite (C_D) and the frontal area of the satellite (A), i.e.,

$$D = \tfrac{1}{2} \rho \, V_s^2 \, C_D A \qquad\qquad (4.1)$$

where $\tfrac{1}{2} \rho \, V_s^2$ denotes the dynamic pressure, and C_D is the drag coefficient for free-molecule flow. Since the ambient density at altitudes above 80 nmi depends also on the variability of solar phenomena, the accuracy in the determination of the life and position of a satellite in low altitude orbit depends on the accuracy in the

PRINCIPLE OF OPERATION

- DECELERATION OF SATELLITE IN ORBIT $= f\left[(\rho)_{atm} \text{ and } (V, C_d, A)_{vehicle}\right]$

- "DRAG FREE SATELLITE", WITH ACCELERATION CONTROLLED PROPULSION, FLIES IN ORBIT UNPERTURBED BY DRAG

- VELOCITY (V), DRAG COEFFICIENT (C_d) AND DRAG AREA (A) OF VEHICLE ARE KNOWN

- DETERMINES DENSITY (ρ)

UNCERTAINTY OF MEASUREMENT

- DENSITY: 10%

- RELATIVE DETERMINATIONS HAVE ERRORS LESS THAN 3%

COVERAGE IN VOLUME

- DENSITY MEASURED BY SATELLITE IN SITU

STATUS OF DEVELOPMENT

- ACCELEROMETER DEMONSTRATED IN OV1-15, OV1-16 AND OTHER SATELLITES

- "DRAG FREE SATELLITE" PROPULSION SERVO DEMONSTRATED IN LABORATORY

RECOMMENDATION

- DESIGN AND TEST SATELLITE INSTRUMENTED WITH ACCELEROMETERS FOR NEEDS OF LOW ALTITUDE SATELLITE ORBIT PREDICTION, USEFUL FOR R/V DISCRIMINATION AND RADIO COMMUNICATIONS
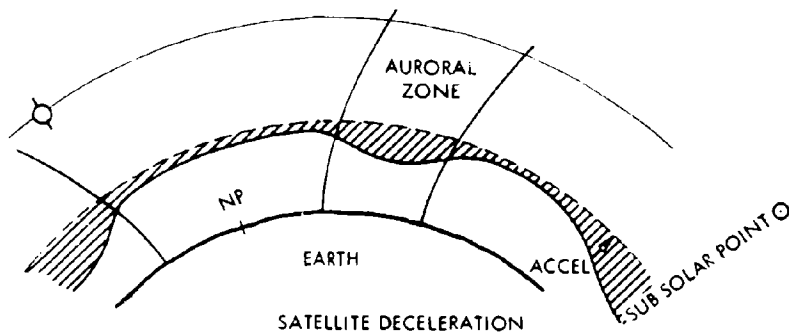
FIGURE 28.   Measurement of Satellite Deceleration for Density at 100-300 km

knowledge of the variability of the ambient density at a given altitude above 80 nmi. The variability of the ambient density at such altitudes can be determined from measurements of the drag force, the satellite speed, the drag coefficient and the frontal area of the satellite. The accuracy in the determination of each of these parameters is described below.

The aerodynamic drag force on the satellite can be measured instantaneously by using a low -g accelerometer capable of detecting accelerations of the order of 10^{-7} g's. A requirement for such low decelerations levels bring about a need to calibrate the low -g accelerometer in orbit. This has been accomplished by using an accelerometer that is supported by electrostatic forces. The accelerometer is calibrated by mounting it on a stable platform provided by a non-spinning satellite such as the Agena vehicle. The calibration of the accelerometer requires determination of the scale factor and bias of the instrument as a function of time during the measurement of the aerodynamic drag. This calibration is accomplished by mounting the accelerometer on a rotating table within the satellite. Since the angular speed of the rotating table can be varied from zero to about one revolution per minute, it is possible to obtain accelerometer data (during every 2048 seconds) for the following four conditions: (1) rotation at a fixed angular speed (of 0.44495 rpm), (2) rotation at a fixed angular speed equal to twice the first value, (3) no rotation while the sensitive axis of the accelerometer points forward (towards the nose of the satellite), and (4) no rotation, sensitive axis aft. The scale factor is determined from the average accelerometer output of the two rotating modes, while the bias is fixed from the accelerometer output of the two non-rotating modes together with the scale factor. Results described in Appendix B indicate good stability of the bias and scale factors in the calibration of the accelerometer over 67 orbits. The sensitivity of the low -g acceler-ometer to 10^{-7} g's provide measurements of the drag acceleration (F/M) at low orbit altitudes to within 1% (DeBra, 1969).

The satellite mass, needed for accelerometer measurements, is known to fractions of a percent.

The speed of the satellite relative to the ambient medium
depends on knowledge of the motion of both the satellite and the air.
The principal uncertainty in this relative motion is due to the
presence of winds, which may be of the order of about 300 ft/sec at
very low satellite altitude (say, 70 nmi). Hence, the uncertainty
in V_s is approximately 1% and that in V_s^2 about 2% (DeBra, 1969).

The frontal area of a non-spinning satellite may be measured
with uncertainty less than 1%.

In terms of the above listed uncertainties, the relative error
in $C_D\rho$ may be written

$$\frac{\Delta(C_D\rho)}{C_D\rho} = \left\{ \left(\frac{\Delta(F/m)}{F/m}\right)^2 + \left(\frac{\Delta m}{m}\right)^2 + \left(\frac{\Delta A}{A}\right)^2 + 4\left(\frac{\Delta v}{v}\right)^2 \right\}^{\frac{1}{2}} \qquad (4.2)$$

and is less than three percent.

The drag coefficient of a satellite in free-molecule flow depends
on the accommodation coefficient, the distribution of the reflected
gas molecules after impact and reemission from the outer-most layer
on the surface of the satellite (i.e., points, chemical deposits, etc),
and the body shape. The accommodation coefficient (α) indicates the
degree of energy transfer between the impinging gas molecules and
such outer layer of the satellite surface, i.e.,

$$\alpha = \frac{E_i - E_r}{E_i - E_s} \qquad (4.3)$$

where E_i denotes the average kinetic energy of the incident gas mole-
cules, E_r that of the re-emitted gas molecules, and E_s the kinetic
energy corresponding to the temperature of the outer layer of the
satellite surface. The accommodation coefficient also depends,
therefore, on the ratio of the mass of the incident gas atoms to the
mass of the atoms in the outer layer of the satellite surface. The

distribution of the reflected gas molecules is characterized by its two extreme mechanisms, i.e., specular and diffuse reflections. Specular reflection occurs when the angle of reflection of a particle is equal to its angle of incidence, while diffuse re-emission takes place according to the Knudsen cosine law. Finally, the body shape does not introduce significant changes in the drag coefficient for free-molecule flow as the average energy of the reflected particles E_r is controlled by the temperature of the outer surface layer, i.e., as E_r approaches E_s or α approaches 1.0.

Theoretical and experimental results for satellite applications indicate the following trends concerning the parameters controlling the level of the drag coefficient for free-molecule flow (Cook, 1965): (1) the accommodation coefficient at the surface of most satellites probably exceeds 0.8 at low satellite altitudes (say, below 200 nmi) at all times of the day and for all levels of solar activity; (2) the exact distribution of the reflected molecules is unknown, and it is probably best to assume diffuse re-emission until further experimental data are available. Fortunately, for accommodation coefficients near unity, the drag coefficient is not particularly sensitive to the distribution of the reflected molecules and little error will ensue from assuming an incorrect distribution; (3) the effect of body shape on the drag coefficient for free-molecule flow is also negligibly small as the accommodation coefficient approaches unity; (4) the effect of altitude on the drag coefficient for free-molecule flow is negligibly small for satellites in low altitude orbits (say, less than 200 nmi); and (5) the value of the drag coefficient for free-molecule flow used in recent years (i.e., $C_D = 2.2$) represents a good estimate based on current knowledge, but it could be low by as much as 10 to 15 percent.

Experience with U. S. satellites in determining atmospheric drag by accelerometer measurements is described in Appendix B. The results of OV1-15 and OV1-16 satellite experiments have been described by Champion (1969), Champion, Marcos and McIsaac (1969) and Champion, Marcos and Schweinfurth (1969).

69

The foregoing considerations indicate that the variability of
the ambient density at low satellite altitudes can at present be
measured with an uncertainty nearly equal to that of the drag coef-
ficient, i.e., to within an r.m.s. error of 10 to 15 percent (DeBra,
1969).

The satellites OV1-15 and OV1-16 for determination of density by
directly measuring drag decelerations have been launched in polar
orbits of perigee altitude about 200 km. From the initial altitude,
drag decay of the small eccentricity orbit has resulted in perigee
altitude reduction to less than 150 km in 30 to 60 days. Satellites
in highly eccentric orbits or with large mass to drag area ratios may
nave lifetimes of a year or more. A large number of such satellites
would be required to give coverage required for use systematically as
regular inputs for purposes of computational simulation.

A more complicated variant is the "drag-free satellite," which
has a self-contained propulsion unit servo controlled by the satellite
accelerometer to maintain the orbit unperturbed by drag decay. Life-
times of a year for a "drag-free satellite" in a circular orbit may be
practical. If operated in a circular polar orbit, 12 "drag-free satel-
lites" would provide data for one altitude continuously along the
orbital paths separated by a maximum distance of about 1600 km. Even
two satellites in polar orbits of large eccentricity, 90° separation
of ascending nodes and 90^{c} differences of perigee latitudes will yield
useful data (Champion, 1969).

DUST BACKSCATTER OF LASER TRANSMISSIONS

INTRODUCTION

Recent developments of laser technology, and the exploration of
the potential of the technology to develop atmospheric probes of
density, temperature, aerosol content and winds, have made exciting
strides. Although the techniques are not as yet fully developed,
there is a basis for believing they have distinctive potential capa-
bilities which deserve further development.

The special characteristics of laser atmospheric probes, now
commonly called lidars, are the demonstrated ability to detect
profiles of aerosol layers in the atmosphere up to altitudes of about
100 km, the small divergence of the laser beam (i.e., one milli-
radian) which can probe an area of transverse diameter of 100 m at
100 km distance, and the small pulse duration of about 30 nano-
seconds, corresponding to a line-of-sight resolution of about 10 m.

A characterization of the technique is given in Fig. 29 which
summarizes considerations reviewed in the following paragraphs dealing
in turn with basic theory, non-coherent detection, coherent detection,
uncertainty of measurements and system considerations.

THEORY

Analysis of the laser signals returned from the atmosphere is
based on the theory of Rayleigh scattering of light by molecules,
Mie scattering by aerosols and on the theory of Raman scattering.
In theory in a dust-free atmosphere, Rayleigh scattering leads to
information describing density and temperature profiles. Goody
(1964) has summarized the theory for Rayleigh scattering in the
atmosphere.

PRINCIPLE OF OPERATION

- LIDAR (A PULSED LASER, ANALOGOUS TO A RADAR) ILLUMINATES AND RECEIVES BACKSCATTER FROM
  AEROSOLS AND MOLECULES. ANALYSIS IS BENEFITED BY NARROW BEAM (0.4 MR), NARROW PULSE
  WIDTH (20 NANO SEC) AND NARROW BANDWIDTH (20A). AEROSOL AND MOLECULAR SCATTER
  MAY BE DISTINGUISHED BY RAMAN EFFECT.

UNCERTAINTY OF MEASUREMENT

- BACKSCATTER BY AIR AND AEROSOLS: 15% AT 20 KM; 100% AT 40 KM
- BACKSCATTER BY H_2O: 5% AT 4 KM

COVERAGE IN VOLUME

- BEAM OF 0.4 MILLIRAD YIELDS RESOLUTION OF 120 M AT 300 KM RANGE
- RANGE RESOLUTION 1.5 KM
- SCATTER VOLUME IS 120 M x 120 M x 1500 M

STATUS OF DEVELOPMENT

- DEMONSTRATIONS OF GROUND BASED LIDARS TO 100 KM RANGE WITH 5 JOULES IN PULSE OF
  5 μ SEC SHOWS PARTICLE SCATTER SUPERPOSED ON MOLECULAR SCATTER
- DEMONSTRATION OF WATER VAPOR BACKSCATTER AT GROUND FROM ALTITUDES 0-4 KM
- RAMAN SCATTER OF LIDAR HAS NOT BEEN DEMONSTRATED

RECOMMENDATION

- RESEARCH TECHNIQUES TO DISTINGUISH AEROSOL (MIE) SCATTER FROM MOLECULE (RAYLEIGH)
  SCATTER, INCLUDING RAMAN SCATTER BY MOLECULES
- DEVELOP HIGH POWER LASERS
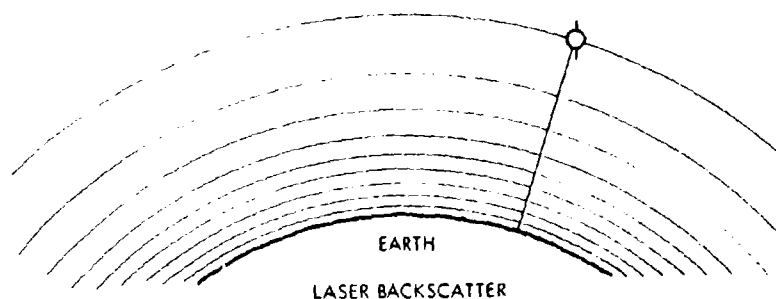
FIGURE 29. Measurement of Laser Backscatter by O_2, H_2O, Dust for Density at 0-30 km

72

The scattered irradiance I at distance R is related to the irradiance I_O of the incident beam of linearly polarized (in direction ϕ) light scattered in direction θ by an optically small particle is given by

$$\frac{I}{I_O} = \frac{\sigma (\theta, \phi)}{R^2} \qquad (5.1)$$

In the scattering of linearly polarized light by optically small particles, for which the condition $2 \pi a m' \ll \lambda_O$ is satisfied, where a is the particle radius, m' is the refractive index of the particle, and λ_O is the vacuum wavelength of the radiation, the angular scattering cross section may be written

$$\sigma(\theta, \phi) = \frac{(2\pi)^2 (m-1)^2}{n^2 \lambda_O^4} \sin^2 \phi \qquad (5.2)$$

where m is the refractive index of the gas rather than of the individual particles and n is the number density of particles. The total cross section σ is found by integrating over all angles.

For air under standard conditions and light of wavelength 6328 Å, $\sigma(\theta, \phi)$ is $2.6(10)^{-26}$ cm^2. Also, the scattering efficiency

$$Q_S \equiv \frac{\sigma}{\pi \sigma^2} \sim 3(10)^{-12} \qquad (5.3)$$

is very small for the molecules found in normal air.

In scattering by spheres which are not small compared with λ_O, the scattering is strongly forward directed, may have several lobes, and varies less strongly with wave length than in the Rayleigh case. The theory of such scattering has been worked out by Mie, so that

$$\sigma = \frac{\lambda^2}{2 \pi} f (4 \pi a) \qquad (5.4)$$

For a water droplet of radius 1 micron, the scattering efficiency is a maximum, so that for wavelength 6328 Å, the total cross section

73

is $1.3 (10)^{-7}$ cm^2. The aerosol particles of principal importance in atmospheric optics are those with radii $0.1 < \alpha < 1.0$ microns. In this range, according to Goody (1964)

$$\sigma = \pi \, \alpha^2 \, (11.7(10)^4 \, \alpha - 0.67) : \quad 0.1 < \alpha < 0.4 \text{ microns}$$

$$\sigma = \pi \, \alpha^2 \, (-3.3(10)^4 \, \alpha + 5.3): \quad 0.4 < \alpha < 1.0 \text{ microns} \quad (5.5)$$

A third form of scattering, well known in physics but not yet exploited in atmospheric instrumentation, is the Raman scattering by molecular vibration, which is uniquely characteristic of the scatterer and which radiates a scattered frequency different from the incident radiation. Raman scattering represents displacement from a critical line due to changes in polarizability of the molecule during vibration-rotation, or rotation alone or vibration alone. For example, for N_2, the Raman scatter radiation is displaced to a wavelength longer than that of the exciting radiation. If the latter is 8583 A, the Raman vibration wavelength is 1.128 microns. Other displacements for N_2 are due to interaction with the rotation or combined rotation-vibration mode, and are much fainter in amplitude to be observed in the far infrared (Herzberg, 1964).

If Rayleigh scattering only occurs in the atmosphere, temperature may be determined from the temperature gradient, using the relation between scale height (the distance in which density varies by factor e) and temperature.

Noncoherent Detection

Using Equations 5.1 and 5.2, the intensity on the ground of a pulse, scattered from a height range dh at altitude h, containing N_0 photons in a interval t seconds is given by

$$I_g = \frac{\sigma \, n \, N_0 T^2}{t \, h^2} \, dh \qquad (5.6)$$

where T is the fraction of light transmitted by the lower atmosphere. Allowing for the finite duration t of the pulse, and integrating

74

over a time τ, the number of photons incident on a mirror of diameter D is

$$N = \frac{\pi D^2 \tau c \sigma N_o^2 n}{8 h^2} \qquad (5.7)$$

If the quantum efficiency of counting of the detector is ϵ, the number of photons actually counted is given by

$$C = \frac{n \sigma}{h^2} \frac{\pi D^2 \tau c N_o T^2 \epsilon}{8} \qquad (5.8)$$

The relation (8) gives the count of photons to be returned by Rayleigh scattering, and is the basic equation by which the performance of a lidar equipment may be evaluated.

Equation 5.8 gives the parameters to be considered in writing specifications for a lidar. Those which may be varied include wavelength λ, the diameter D of the receiving mirror, the integration time τ, the number of photons transmitted N_o, and the quantum efficiency ϵ of the photomultiplier tube used as detector. The transmission T of the atmosphere must also be taken into account since it is wavelength dependent.

Choice of wavelength should consider the inverse proportion to the fourth power of the wavelength of the scattering coefficient σ and that the quantum efficiency ϵ of the detector is greater for shorter wavelengths. However in the lower atmosphere the transmission T decreases as the wave length gets shorter. The optimum wavelength seems to be between 0.4 and 0.5 microns. With recent experiments, however, the choice of wavelength has been dictated by the fact that the ruby laser, operating at 0.694 microns, is the most powerful and efficient of the high power pulse lasers working in the visible spectrum. The performance of lasers as transmitters is currently developing rapidly.

The limitation on the size of the receiving mirror used for non-coherent detection under standards easier than those of astronomy seems only to be one of cost.

The number of photons transmitted is directly proportional to energy output. Clearly the highest available energy should be used. In general, the basic lasing pulse is 0.5 to 1.0 millisecond. Such length does not yield range resolution. A system of Q-switching, involving a rotating prism, causes lasing to occur in giant pulses of about 20 nsec duration. By such a means, a series of giant pulses is obtained which have a total energy of about 5 joules in an overall duration of about 5 microsec at a repetition frequency of about 0.16 pulses per second

The integration time for a single pulse depends upon the height resolution required. A long integration times yields a larger number of photons, but decreases the height resolution. A common integration time is 10 microsec, corresponding to height resolution of 1.5 km.

The quantum efficiency of photomultiplier tubes depends on the type of cathode and the wavelength. The S-20 response normally used does not allow high efficiency at 0.694 microns. Typically the efficiency is 3 to 6%.

Noise in an optical sounder can arise in two ways: due to an external source such as sky noise, or due to an internal source such as receiver noise. Sky noise is usually wide band, originating from scattered sunlight in day time, and from starlight, airglow, moonlight and other minor sources at night, and may be reduced by use of a narrow band optical filter in the receiving system. The bandwidth of the transmitted signal is approximately 10^{-6} micron. Because the insertion loss of optical interference filters increases rapidly as bandwidth decreased, it is practical to use a filter not narrower than $2(10)^{-3}$ microns (20 Å). Sky noise is further reduced by

restricting the beamwidth of the laser system. The beamwidth of the laser itself, about 10 millirad, is further reduced by use of a parabolic transmitting mirror. A 20 cm mirror reduces effective beamwidth to 0.4 millirad.

Noise from the photomultiplier is reduced by cooling of the photocathode, by use of a shutter to protect the photomultiplier from the fluorescence of the laser after the pulse and from the over-excitation of the cathode by intense light scattered by the lower atmosphere.

Temperature regulation of the laser is required, to avoid wave-length drift as the laser heats up from the energy dissipated within it. In general temperature must be stabilized to be within a band of about $1^{\circ}C$.

Examples of lidars in current use have been described by Clemesha et al., 1967, Collis and Ligda, 1966, Sandford, 1967, and others.

Coherent Detection

The coherence of electromagnetic radiation of a laser suggests immediately its exploitation in ways analogous to radar Doppler measurement. J. C. Owens (1969) has made a system analysis of optical heterodyne measurement of Doppler shifts as a method for the remote determination of vector wind velocity, by bistatic measurements. Owens (1969) technique, since it is bistatic and requires that the unscattered radiation travel an optical path of equal length to that of the scattered radiation, is clearly not useful for monostatic measurements from satellites. However his computation of the maximum range attainable in wind or temperature measurement using aerosol or molecular scattering is interesting. Owens finds that the signal-to-noise power ratio of scattering from scatterers of number density n is given by

$$\frac{S}{N} = \frac{\varepsilon\, P_o}{h\nu B}\; \frac{8}{3\,\pi}\; \frac{n\, \lambda^2\, \sigma\, (\theta_1 \phi)}{d} \qquad\qquad (5.9)$$

wherein S is power of received signal, N is power of noise, ε is the quantum efficiency of the detector, $h\nu$ is the energy of a single photon, P_o is the laser transmitter power, B is the receiver system bandwidth.

λ is the wavelength of radiation and d is the diameter of the spherical scattering volume. Setting the signal-to-noise ratio to unity, and using the approximation for the diameter of the scattering volume to be

$$d \approx 2\, \lambda\, \frac{R}{D} \qquad\qquad (5.10)$$

where R is the range from transmitter to scattering volume and D is diameter of the receiving aperture, Owens (1969) finds that the effective range is given by

$$R = \frac{\varepsilon\, P_o}{h\nu B}\; \frac{8}{6\,\pi}\; n\, \lambda\, \sigma\, (\theta_1 \phi)\, D \qquad\qquad (5.11)$$

Assuming the values of the system parameters to be as follows:

Detector Efficiency	ε =	0.05
Transmitter Power	P_o =	50 mw
Wavelength	λ =	6328 Å
Receiving Aperture Diameter	D =	15 cm

Owens finds that ranges of such a system may be the following: for clear air conditions, using bandwidth B = 50 kHz, the range is 55 cm; and for fog, using bandwidth of 825 Hz, the range is 175 m. Because the thermal motion of the molecules is much greater in frequency broadening than the displacement of the wind induced Doppler, the range calculated by equation 5.11 is $1.8(10)^{-6}$ cm, which is to say the measurement of wind by Doppler is impossible.

For similar reasons, Owens finds that measurements of temperature based on Rayleigh scattering are also infeasible.

OBSERVATIONS

Goyer and Watson (1968) have summarized recent results of observations of the upper atmosphere by lidar techniques. Figure 30 shows Goyer and Watson's summary of the ratio of the total back-scatter cross sections (molecular plus aerosol) to molecular back-scatter cross section as a function of altitude, as measured by a number of scientists including Bain and Sandford (1966), Clemesha et al. (1966, 1967), Fiocco and Columbo (1964b), Fiocco and Grams (1964a, 1966), Fiocco (1965), Kent et al. (1967), Nishikori et al. (1965), and Grams and Fiocco (1967). All have detected the 18 to 20 km scattering layer, and a broad secondary scattering layer around 24 km. Three studies (Fiocco et al., 1963, Bain and Sandford, 1966 and McCormick et al., 1966) have reported scattering layers as high as 120 km, which others have challenged on the grounds that the poor signal to noise ratio at the high altitudes could not show definite evidence.

Schotland (1965) has made use of the 6942.15Å water vapor absorption line in an attempt to determine the water vapor absorption profile in the lower 4 km of the atmosphere. Since the half-width of the line is only 0.1 A, the measurement required a shift in the wavelength of the laser radiation of only 0.6 A, easily obtained by the temperature control of the laser rod. By measuring the ratio R(z) of the return signal intensity in the absorption line to that outside that line, at discrete altitudes, Schotland obtained qualitative water vapor profiles shown in Fig. 31.

Uncertainty of Measurements

Collis and Ligda (1966) have estimated the statistical variability in groups of ten lidar observations between 20 and 40 km to be the following, in terms of standard deviation divided by the mean: 0.15 at 20 km, 0.25 at 25 km, 0.5 at 30 km, 0.7 at 35 km and 1.0 at 40 km.
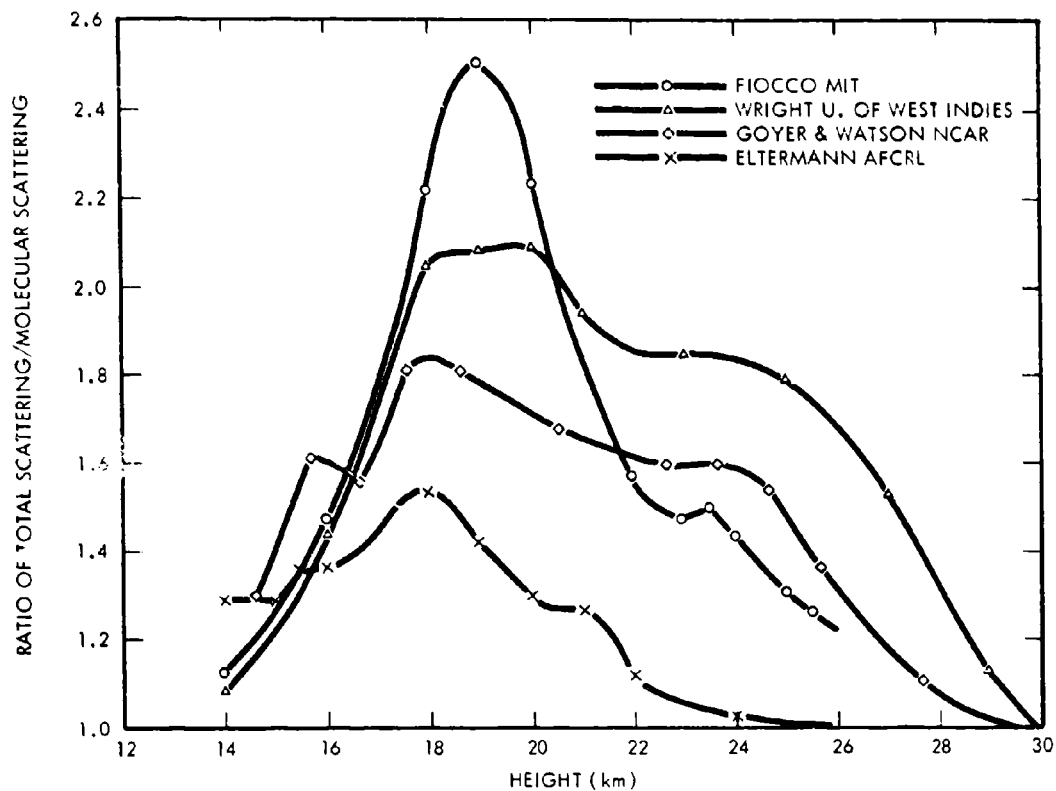
FIGURE 30. Ratio of the Total Backscatter Cross Section (Molecular Plus Aerosol)
to Molecular Backscatter Cross Section as a Function of Altitude
(After Goyer and Watson, 1968)

Schotland (1965) has estimated the uncertainty of the data on
water vapor in the atmosphere up to 4 km, shown in Fig. 31 to be
between 3 and 5%.

It is reasonable to expect that the uncertainty of measurements
will depend on signal to noise ratio, which will be smaller at long
range than at short range.

SYSTEM CONSIDERATIONS

The high power laser has been proven as a tool for probing the
atmosphere for total particle number density with fractional
uncertainty of about 0.15 and water vapor density. It appears to

80
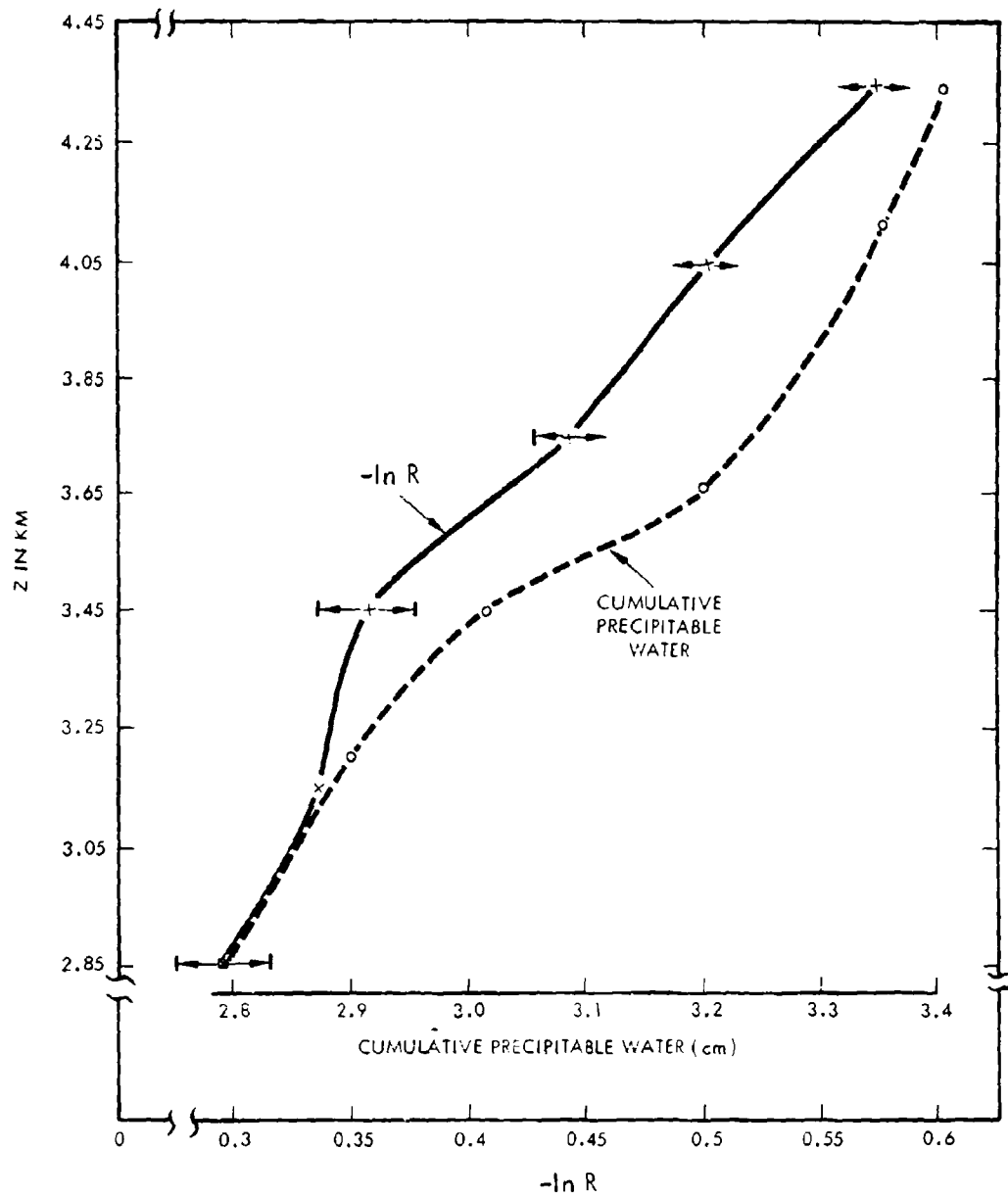
FIGURE 31. Water Vapor Sounding Data for 26 March 1965
(R. M. Schotland et al., New York University, 1965)
(From Goyer and Watson, 1969)

have potential as a probe for determination of density of other
atmospheric components and in particular aerosols. Chief limitation
on use of the technique, in satellites other than the incomplete
state of development of components, appears to be the inefficiency
(high dissipation) of input power.

MOTION OF CLOUDS FROM SATELLITE PICTURES

The motion of clouds is to some extent a measure of the wind. Such motion may be deduced from pictures of clouds, made from cameras in satellites.

A characterization of this technique is given in Fig. 32, which summarizes considerations reviewed in the following paragraphs.

PRINCIPLES OF OPERATION
- MOTION OF CLOUDS IN TIME SEQUENCE PICTURES FROM SATELLITES DETERMINES WIND

UNCERTAINTY OF MEASUREMENT
- WIND VELOCITY: 25%
- LIMITED BY IDENTIFICATION OF CLOUDS WHICH MOVE WITH AIR

COVERAGE IN VOLUME
- AT CLOUD HEIGHT (1-18 KM) ONLY

STATUS OF DEVELOPMENT
- DEMONSTRATED BY TIROS, NIMBUS, ATS

RECOMMENDATION
- SINCE TECHNIQUE HAS LIMITED UTILITY, LEAVE DEVELOPMENT TO OPERATORS AND OTHER AGENCIES

SATELLITE PICTURES OF CLOUDS
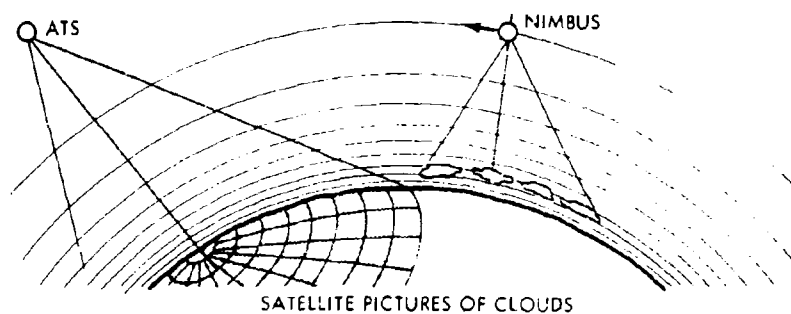
FIGURE 32. Measurement of Cloud Motion From Satellite Pictures for Wind at 1-18 km

A series of successive pictures obtained from satellites in
geosynchronous orbit (i.e., in the equatorial plane at about 19,300
nmi altitude) can show in a global scale a rather continuous motion
of given cloud elements over geographical locations under sunlight
conditions. The continuous motion of given cloud elements is
detectable under sunlight conditions because geosynchronous satel-
lites remain fixed relative to the earth. The motion of clouds
then becomes of interest because they can be used as tracers for the
determination of the horizontal wind field at mainly low altitudes,
since preliminary results indicate that the population of traceable
clouds has a distribution of about 60 percent below 5000 ft (850 mb),
30 percent between 300 and 200 mb, and 10 percent in other altitudes
(Fujita, 1969). Proposals for the early GARP program would utilize
two kinds of high resolution instruments for the observation of the
cloud elements: (1) an optical scanner similar to the spin-scan
cameras used in the NASA ATS-1 and ATS-3 satellites (Appendix A),
which would provide daytime cloud tracking with a horizontal resolu-
tion of 2 to 3 km with an accuracy for horizontal displacement of
about 1 km; (2) a scanning infrared radiometer operating in the
8-12 μ window region to measure the altitude of cloud tops with an
accuracy of ± 0.5 km (assuming a temperature profile and a uniform,
opaque cloud), and a horizontal resolution of 8 to 12 km with an
accuracy for horizontal displacement of about 5 km. This IR radio-
meter would provide pictures with a spatial resolution range (at
nadir) of about 8 x 8 to 16 x 16 km (depending on the optics) of
the disc of the earth, with a full picture available every 30 minutes.
This sensor subsystem would yield daytime wind data from cloud
elements that are larger than 8 to 12 km, but which have a detectable
structure of smaller scale. Since the nighttime wind data will not
be as good, this subsystem is limited to daytime and cloudy conditions.

Measurements of horizontal wind profiles from cloud motion have
been made using available pictures from the ATS-1 and ATS-3 geo-
synchronous satellites. The spin-scan subsystem on these satellites
provides pictures with a resolution of about 4 km (Appendix A). The

"cloud velocity" is obtained by the measurement of a cloud displacement as derived from a sequence of ATS photos (Johnson, 1967). The suitable cloud elements are selected by avoiding clouds that do not move with the wind, i.e., (1) orographic clouds, (2) cumolonimbus clouds (3) clouds that are related to the phase velocity of horizontal-transverse wave motions, (4) clouds with a rapidly changing structure at their boundaries, and (5) clouds in the area of jet streams where the windshear is rather large. The cloud displacements have been measured by using a stereoscope and a plastic measuring device called a "stereo wind graph." Two pictures properly positioned under the stereoscope allows one to measure the change in cloud position accurately. The reduction of cloud displacement to cloud velocity requires the following considerations: (a) the scale of the photographs as obtained from the relative dimension of the earth's picture image diameter to the earth's diameter; (b) rectification of the geometry, since one is looking at the projection of an oblate spheroid on the flat plane of an ATS picture; (c) corrections for aspect ratio, which is the ratio of oblateness introduced into the printed ATS picture from the deflection of the electronic beam in the display print system. The picture elements are "squeezed" together so that the picture is printed oblately; and (d) print paper distortion introduced by paper stretching during the developing process. The resulting cloud velocity values can then be compared with radiosonde wind measurements by assuming that the clouds move with the wind field. Since the altitude of the clouds in the ATS pictures is unknown, the dew points determined from the radiosonde soundings were used to fix the levels of the clouds.

A comparison of the direction and magnitude of the velocity vectors for the cloud motion derived from ATS pictures with radiosonde wind data for 61 observations has been made by M. H. Johnson (1968) who indicates the following results: (1) the standard deviation between the direction of the cloud motion and the radiosonde wind data is 15 deg for wind velocities that are higher than about 4 m/sec (see Fig. 33); and (2) the standard deviation between the

85

magnitude of the cloud velocity and the radiosonde wind data is 2.2 m sec^{-1} (see Fig. 34). The fractional uncertainty of wind estimation varies from about 0.25 at 15 m sec^{-1} to 1.0 at 3 m sec^{-1}. Comparable errors have been reported by L. F. Hubert and L. Whitney (1969) and Fujita et al. (1968).
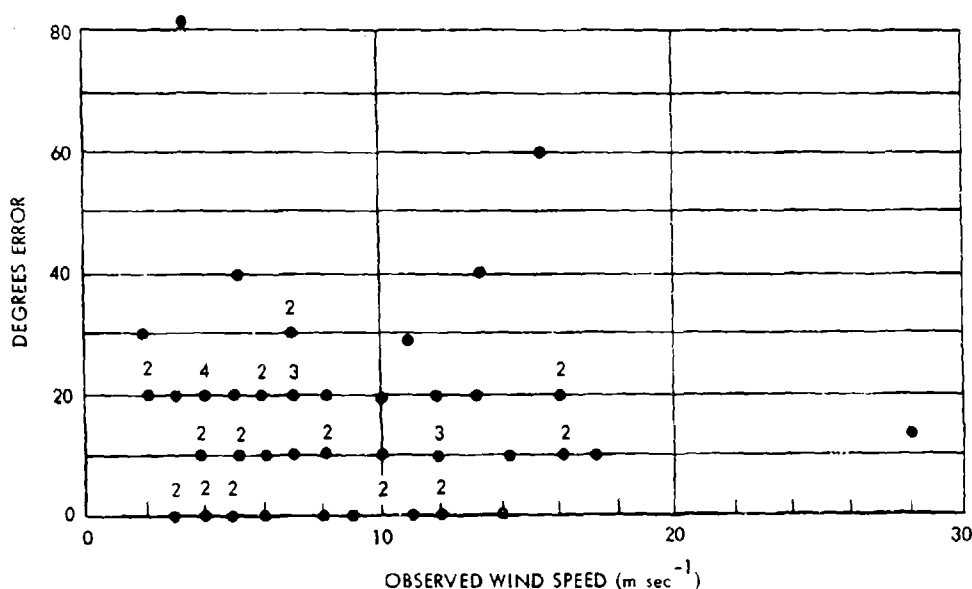
FIGURE 33. Distribution of Directional Differences Between Observed and Calculated Wind Directions (After M. H. Johnson, 1967)

The use of computational techniques for determination of divergence and rotation of a cloud field promises an improvement over the techniques based on comparison of the cloud positions with terrestrial references.

The foregoing results from ATS picture data indicate that observations from geosynchronous satellites of the motion of selected clouds during a short time can yield the horizontal wind velocity at low cloud levels over given geographical locations under sunlight conditions. The horizontal wind field derived from geosynchronous satellite picture data by itself lacks the accuracy required for the

long-range forecasting of the weather. However the wind data derived from cloud pictures appear to be valuable as one form of initial condition input to the computational simulation of wind fields.
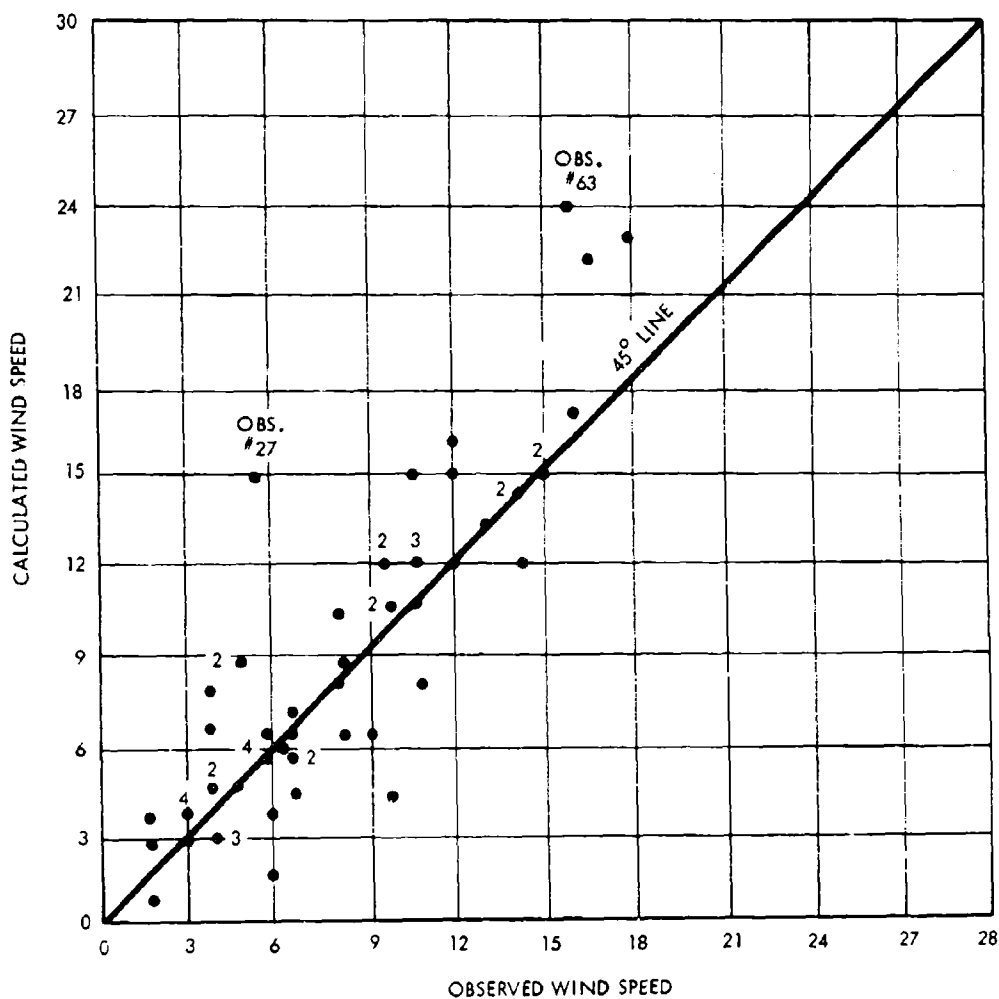
FIGURE 34. Distribution of Speed Differences Between Observed and Calculated Wind Speed (After M. H. Johnson, 1967)

TRACKING OF BALLOONS FROM SATELLITES

The measurement of the displacement of constant-level satellite tracked balloons is a technique for the direct measurement of wind, which seems to have great promise.

A characterization of the technique is given in Fig. 35 which summarizes specifications and performance to be developed by the Global Atmospheric Research Program, an international collaborative effort which is receiving considerable support within the United States. The detailed description of the the program has been described in detail by Bolin, 1967.

Components of the balloon system have been partially demonstrated. The first satellite system tests are scheduled for NIMBUS-D in 1970-71. However, since the technique appears to be receiving great attention from civil agencies and the system of balloons also seems to have great military vulnerability, it is recommended that the major tasks of the development be left to the civil and international agencies.

<u>PRINCIPLE OF OPERATION</u>

- BALLOONS AT CONSTANT DENSITY LEVEL ARE TRACERS FOR WINDS, WITH DISPLACEMENT MEASURED FROM SATELLITE BY DIFFERENTIAL DOPPLER OR EOLE RANGE RATE MEASUREMENTS.

<u>UNCERTAINTY OF MEASUREMENT</u>

LOCATION TECHNIQUE	LOCATION ERROR	WIND ERROR	FRACTIONAL WIND ERROR
RANGE/RANGE-RATE SYSTEM	1-2 KM	0.15-0.3 MSEC^{-1}	1.5 - 3%
DIFFERENTIAL DOPPLER	10 KM	2.5 MSEC^{-1} IN 90 MIN	25%
		1.3 MSEC^{-1} IN 2.4 HR	13%

<u>COVERAGE IN VOLUME</u>

- 10,000 BALLOONS AT 200 MB (10-15 KM ALTITUDE) WITH LIFETIME 1 YEAR YIELD ONE MEASUREMENT PER DAY ON 400 KM GRID IN ZONE 60°N - 60°S

- 5,000 BALLOONS AT 800 MB (1 KM ALTITUDE) WITH LIFETIME 20 DAYS YIELD ONE MEASUREMENT PER DAY ON 430 KM GRID IN ZONE 30°N - 30°S

<u>STATUS OF DEVELOPMENT</u>

- BALLOON DEMONSTRATED BY U.S. AND FRANCE

- LOCATION SYSTEM EOLE DEMONSTRATED IN AIRCRAFT; DIFFERENTIAL DOPPLER NOT DEMONSTRATED

- BALLOON ELECTRONICS AND POWER SUPPLY DEMONSTRATED BY EOLE

- FIRST SATELLITE TESTS NIMBUS D 1970-71

<u>RECOMMENDATION</u>

- SINCE MILITARILY VULNERABLE, LEAVE MAJOR DEVELOPMENT TO CIVIL AND INTERNATIONAL ORGANIZATIONS

SATELLITE-TRACKED BALLOONS
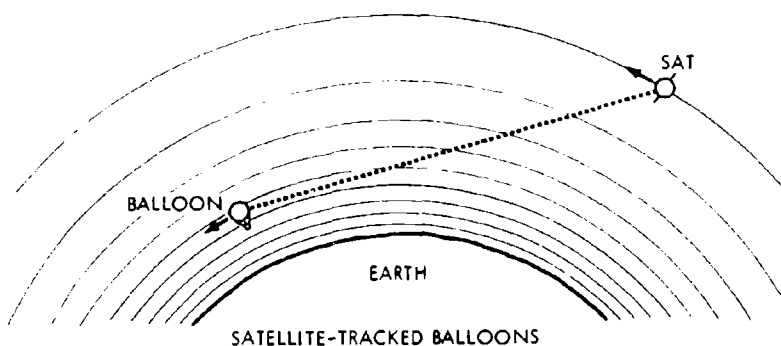
FIGURE 35. Measurement of Displacement of Satellite Tracked Balloons for Wind at 1 km and 10-15 km

NUMERICAL METHODS AND COMPUTER SIMULATION

A review of techniques for measurements from satellites indicates that wind may be determined explicitly by utilization of balloon-tracking satellites together with satellite TV-like observation of cloud motions. However, these techniques appear to be marginal as judged both on theoretical grounds and from the results of past performance. An alternative to such explicit measurement techniques is the implicit determination of winds by computational simulation of atmospheric motions, and a discussion of such an approach forms the content of the present section.

One application of computers in a simple form is the use of temperature data as determined by TIROS satellites in the mid-latitude field for the estimation of velocities utilizing the geostropic wind equation as described in Volume IV. The error in using the approximate geostropic wind equation results in uncertaintites of the order of 20% in the wind, a figure which is adequate for many purposes (for example in airline flight routing), but in others, such a numerical weather prediction, the geostropic approximation is clearly quite inadequate.

A further important exploitation of computation simulation is the prediction of cloudiness. In view of the importance of albedo variation in weather processes, the variability of cloud distribution is a most significant contributor to the variability of winds in the troposphere. Experiments in the prediction of cloudiness have been undertaken by Kasahara and his associates at NCAR, Boulder, Colorado.

The global simulation of the atmospheric circulation in the upper atmosphere for the implicit determination of winds using a full set of atmospheric input data has been suggested by Murgatroyd (1968). The success of such simulations for the lower atmosphere (the tropo-sphere) in the last few years lends credence to the belief that this,

much larger task (which must include the tropospheric simulation as part of the total) can indeed be accomplished. To indicate the nature of the problems to be faced in such a project the remainder of this section will be devoted to a brief summary of the basis of the numerical programs that are used today for global weather and climate simulations, together with an indication of the types of difficulty that have been overcome in their implementation, and will conclude with an estimate of the scope or the corresponding numerical problem for simulation of the complete atmosphere from 0 to 200 km.

A characterization of the technique of computational simulation of the atmosphere as a means of determining wind at all altitudes is given in Fig. 36, which summarizes considerations discussed in the following paragraphs dealing in turn with differential equations for tropospheric simulation, finite difference forms and stability, nonlinear effects and stability, boundary conditions, characertistics of current tropospheric numerical simulations, and the extension from current tropospheric simulations to simulations of the global upper atmospheric circulation.

Differential Equations for Tropospheric Circulation

Until the advent of high speed computing techniques, attempts to solve the mathematical problems of atmospheric motions were based on gross simplifications of the governing equations, several of which have been discussed in "Hydrodynamic Theory of Wave Motion in the Troposphere" of Volume IV. Today, with the aid of rapid computation capability, a much more complete and satisfactory set of fluid dynamic equations can be tackled. The commonly accepted formulation that is believed to be quite adequate for describing tropospheric conditions (i.e., weather) consists of the compressible Navier-Stokes equations with the following assumptions:

a. The planetary atmospheric layer is thin compared with the earth's radius.

b. The horizontal component of the Coriolis force is negligible. $\qquad$ (8.1)

c. The hydrostatic equation holds.

PRINCIPLE OF OPERATION

- CONTINUITY EQUATIONS (MOMENTUM, MASS, ENERGY) ARE BASIS FOR WINDS = f(ρ, T, ENERGY, POSITION) IN TROPOSPHERE, AND MORE VARIABLES IN UPPER ATMOSPHERE
- ALL REQUIRED INPUTS ARE DETERMINABLE BY SATELLITE ON 300 KM, 3 HR GRID

UNCERTAINTY OF DETERMINATION

- WIND: 25% (GEOSTROPHIC APPROXIMATION IN MID LATITUDE TROPOSPHERE); <<25% (PRIMITIVE EQUATIONS) FOR TROPOSPHERE; LARGER FOR UPPER ATMOSPHERE

COVERAGE IN VOLUME

- GLOBAL, OVER ALTITUDE RANGE 0-300 KM ON 300 KM GRID AND IN 3 HOUR TIME STEPS

STATUS OF DEVELOPMENT

- DEMONSTRATED FOR TROPOSPHERE BUT WITH INADEQUATE DATA INPUT
- TROPICAL TROPOSPHERE ANALYSIS LIMITED BY INADEQUATE INPUT DATA (ESPECIALLY WATER VAPOR)
- UPPER ATMOSPHERE ANALYSIS LIMITED BY INADEQUATE INPUT DATA, KNOWLEDGE OF PROCESSES AND PRESENT-DAY COMPUTER CAPACITY

RECOMMENDATION

- DEVELOP SYSTEMS TO DETERMINE ALL MEASUREABLE ATMOSPHERIC PARAMETERS FROM SATELLITES
- RESEARCH ATMOSPHERIC PROCESSES, ESPECIALLY IN UPPER ATMOSPHERE, FOR WHICH 1973 GARP MAY PROVIDE LOWER BOUNDARY
- DEVELOP LARGE CAPACITY COMPUTERS, I.E., ILLIAC IV
- BEGIN UPPER ATMOSPHERE COMPUTATIONAL SIMULATION

COMPUTER SIMULATION

FIGURE 36. Computational Simulation of Atmosphere for Wind at All Altitudes

In the meteorological community the Navier-Stokes equations with these assumptions are commonly called the "primitive equations." Some treatments of atmospheric circulation problems do omit, some but not all, of the horizontal Coriolis force terms (assumption b) in the equations, but the logical consistency of this is questionable (Eckart, 1960).

Other assumptions, affecting the "forcing terms" in the equations, i.e., those involving body forces and energy transfers arising from viscous and external sources, are also made, but these can be discussed independently of the general formulation of the partial differential equations. These equations are, under assumptions 8.1 (compare "Physics of the Troposphere" of Volume IV).

Continuity: $$\frac{\partial \rho}{\partial t} + \nabla \cdot (\rho \bar{v}) = 0 \tag{8.2}$$

Momentum:
$$\frac{\partial u}{\partial t} + \bar{v} \cdot \nabla u - \Omega \sin\theta u = -\frac{1}{\rho}\frac{\partial p}{\partial x} + F_x \tag{8.3}$$

$$\frac{\partial v}{\partial t} + \bar{v} \cdot \nabla v + \Omega \sin\theta v = -\frac{1}{\rho}\frac{\partial p}{\partial y} + F_y \tag{8.4}$$

Thermodynamic or energy.
$$\frac{\partial s}{\partial t} + \bar{v} \cdot \nabla s = \frac{q}{T}$$
or
$$(\frac{\partial}{\partial t} + \bar{v} \cdot \nabla)\, \ell n\, T^{1/\gamma} = \frac{q}{c_p\, T} \tag{8.5}$$

State: $$p = \rho\, RT \tag{8.6}$$

Hydrostatic: $$\frac{\partial p}{\partial z} = -\rho g \tag{8.7}$$

where x, y, z are rectangular coordinates in which the (x, y) plane is locally horizontal to the earth's surface.

$\bar{v} = (u,v,w)$ is the fluid velocity

s   is the entropy

ρ is the density

T   is the temperature

p   is the pressure

$\overline{F} = (F_x, F_y, F_z)$ is the body force

q is the rate of energy input

g is the force of gravity

R is the gas constant

c_p is the specific heat at constant pressure, and

γ is the specific heat ratio

In the normal procedure for a finite difference numerical solution of these equations the first four are treated as "prognostic" equations, i.e., the time derivatives are evaluated in terms of given (observed) initial values at time t of all the dependent variables, and then the equations are integrated over a short time step Δt. The result are estimates of ρ, u, v, and s at time $(t + \Delta t)$ in each of the horizontal planes selected for the finite difference vertical grid. Involved in this process is knowledge of the vertical velocity, w, not normally obtainable from meteorological observations; in fact, w can be derived from the remaining two equations, 8.0 and 8.7, combined with the continuity equation. The result is the Richardson equation that couples the vertical to the horizontal motions:

$$w = -\int_0^z \left(\frac{\partial u}{\partial x} + \frac{\partial v}{\partial y}\right) dz - \frac{1}{\gamma} \int_0^Z \frac{1}{p} \left\{ \left[\frac{\partial p}{\partial t}\right]_{z = z_T} + u \frac{\partial p}{\partial x} \right.$$
$$\left. + v \frac{\partial p}{\partial y} - g \int_z^{z_T} \left(u \frac{\partial(\rho u)}{\partial x} + v \frac{\partial(\rho u)}{\partial y}\right) dz \right\} dz + \frac{1}{c_p} \int_0^z \frac{q}{T} dz \tag{8.8}$$

where z_T is the "top" of the atmosphere, the upper altitude limit of the computational grid system.

The details of how the computation proceeds between the horizontal prognostic estimations (Eqs. 8.2-8.5) and the "diagnostic" equations (8.6-8.8) vary with different numerical schemes, and need not be entered into here, since no fundamental questions involving computational characteristics are involved. However, it may be mentioned that a common variation is to use the pressure p instead of z as

independent vertical coordinate, with a subsequent simplification in the diagnostic Eq. 8.8. Another standard modification of the equations as presented here is the use of longitude, λ, and latitude, θ, in place of x and y as independent variables. This does not affect the general discussion in any way.

The procedure for solution described above requires specification of the stress terms F_x, F_y, and the energy source q. In Volume IV, "Hydrodynamic Theory of Wave Motion in the Atmosphere" discusses the external sources of energy in some detail. Indeed their accurate evaluation is a very important and difficult part of the total forecasting problem; we cite in particular the questions of radiative transfer and latent heat in phase changes of water as being particularly significant. However, the mathematical aspects which we discuss here are not sensitive to these questions, rather they are influenced by the viscous and thermal conductivity contributions to F_x, F_y, and q, since these are functions of the dynamic state of the atmosphere. In the normal formulation of the Navier-Stokes equations, these factors are given as

$$(F_x, F_y, F_z) = \frac{1}{\rho} \left\{ \mu \nabla^2 \bar{v} + \frac{1}{3} \mu \nabla (\nabla \cdot \bar{v}) \right\} \tag{8.9}$$

$$q = \frac{1}{\rho} \left\{ k \nabla \cdot (\nabla T) + \Phi \right\} \tag{8.10}$$

where μ and k are the (molecular) viscoscity and thermal conductivity, respectively, assumed constant; the first term in 8.10 is the thermal diffusion contribution to q, and Φ the viscous dissipation function, is given by

$$\Phi = \mu \left[2 \left\{ \left(\frac{\partial u}{\partial x} \right)^2 + \left(\frac{\partial v}{\partial y} \right)^2 + \left(\frac{\partial w}{\partial y} \right)^2 \right\} + \left(\frac{\partial w}{\partial y} + \frac{\partial v}{\partial z} \right)^2 \right.$$
$$\left. + \left(\frac{\partial u}{\partial z} + \frac{\partial w}{\partial x} \right)^2 + \left(\frac{\partial v}{\partial x} + \frac{\partial u}{\partial y} \right)^2 \right] \tag{8.11}$$

The role of the quantities 8.9 and 8.10 in atmospheric circulation is not clear. They are certainly important in the Ekman layer, but in the finite difference computational schemes the latter is a small fraction of the vertical grid size and the molecular diffusion and dissipation properties are incorporated via lower altitude boundary conditions, which have not been discussed as yet. For similar reasons (i.e., the large dimensions of the finite difference mesh, both vertically and horizontally), it has been argued that the forms 8.9 and 8.10 are not appropriate for the finite difference solution, and that the dissipation and diffusion effects should rather be expressed in terms of an assumed random turbulent flow eddy motion occurring at a sub-grid scale. By analogy with turbulent boundary flow theory, it is assumed that this turbulence can be represented in terms of a Reynolds stress and an effective eddy viscosity coefficient, usually with much simplified expressions for F and q as functions of the velocity or the velocity derivatives.

Whether such a representation is valid physically is not known, however, from a computational point of view the introduction of dissipation can be vital in order to achieve computational stability as will be discussed below. Apart from this important contribution, the effects of the diffusive and dissipative aspects of F and q are probably not important for short period forecasting. For longer time periods (currently estimated as three days or more), it is not yet known whether a different representation is necessary, or even whether a stochastic formulation for the sub-grid scale effects is possible at all. This question will be entered into in more detail later in this section when nonlinear effects are considered.

Finite Difference Formulations and Their Stability

The prognostic system of Eqs. 8.2 - 8.5 appears at casual inspection to be straightforward, if lengthy, to solve by finite differences. Computation times, however, are considerable, as can be seen from the characteristics of present-day numerical programs listed in Table 8, and result in a limitation of their utility. The difficulty

97

arises both from the large number of spatial mesh points required by a global model, and from the restriction in the finite difference representation to a maximum time grid interval, as required for computational stability. In fact, the question of computational stability is a principal issue in the effective employment of numerical simulation of the atmosphere and a brief description of the nature of the problem follows.

The fluid dynamic equations for the horizontal motion 8.2 - 8.5 describe a nonlinear system in which the nonlinearities are introduced via the advective terms, $\overline{v} \cdot v$, and the dissipation function ϕ. Since there are no known methods of establishing the stability or convergence properties of finite difference representations of nonlinear equations of this degree of complexity, the main approach for treating them has had to be heuristic. Thus, linearized approximations are studied, and time and distance mesh scales are selected that ensure computational stability for those linearizations. The resulting numerical programs are then checked as to their nonlinear stability performance by trial computations. If as is common, the trial shows an instability, damping is empirically introduced into the system of equations, either with artificial viscosity terms or by an increase in magnitude of the voscosity that may already be present. As discussed earlier, it is expected that the frictional effects thus introduced should have little effect on scales larger than the grid size, so that the approach can be regarded as a device to alter the mathematical properties of the finite difference scheme without altering their physically important properties. There is clearly the danger in that ad hoc approach that in fact the mathematical and physical characteristics are more closely linked than assumed, and this possibility will be discussed in greater detail later.

The rationale for assuming that the properties of the linearized equations can be used to approximate the behavior of the nonlinear equations is based on the consideration of _local_ behavior. Thus, if the correct solution is continuous, and we assume that the difference

TABLE 8. GLOBAL TROPOSPHERIC CIRCULATION SIMULATIONS

Feature	Leith, 1965	Mintz-Arakawa, 1965	Smagorinsky et al., 1965	Kasahara and Washington, 1967
Equations (Refs. 1, 5)*	Hydrostatic	Hydrostatic	Hydrostatic	Hydrostatic
Coverage (Refs. 1, 2, 5)*	Global-spherical coordinate; Vertical coordinate-pressure	Global-spherical coordinate; σ-coordinate in vertical $\sigma = (p - p_0)/(p_s - p_0)$.	Northern Hemisphere $0° - 64$ N; Spherical coordinate; Vertical coordinate-pressure	Global-spherical coordinate; Vertical coordinate-height
Vertical Structure (Refs. 1, 5)*	Baroclinic atmosphere; continents and oceans; constant stability parameter	Baroclinic atmosphere; orography, ocean (sea/continent/ice); constant stability parameter	Baroclinic atmosphere; smooth earth; constant stability parameter	Baroclinic atmosphere; no orography, ocean-continent; temperature prescribed; constant stability parameter
Energy Dissipation Processes (Refs. 1, 5)*	Horizontal: turbulent viscosity; vertical: turbulent exchange; surface friction	Horizontal: turbulent viscosity; vertical: turbulent exchange; surface friction	Horizontal: turbulent viscosity; vertical: turbulent exchange; surface friction	Horizontal: turbulent viscosity; vertical: turbulent exchange; surface friction
a. Turbulent coefficient (Energy dissipation) $K_H \nabla^2 v_H$			Function of Deformation Tensor	Function of Deformation Tensor
Horizontal K_H m²sec⁻¹	10^6	$2(10)^4$ (at $7°$ latitude)	5	60 + stability dependent term
Vertical K_z m sec⁻¹	24	22 (at 600 mb)	$12(10)^{-3}$	3×10^{-3}
b. Frictional coefficient K_t	10^{-2}	$6.5(10)^{-3}$		
Energy Influx Processes (Refs. 1, 5)*	Horizontal: heat diffusion; convection in boundary layer	Horizontal: heat diffusion; convection in boundary layer; convection in moist air	Horizontal: heat diffusion only	Horizontal: heat diffusion; convection in boundary layer
a. Coefficient of turbulent heat diffusion K_T m²sec⁻¹ (Heat in = $K_T \nabla^2 T$)	10^6	$2(10)^4$ (at $7°$ latitude)	$1.5(10)^5$	Vertical: same as K_z
Surface Convection	Linear extrapolation	Linear extrapolation	$v_s = 0.5\{[2.384u_3 - 0.384u_1]^2 + [2.384v_3 - 0.384v_1]^2\}^{1/2}$ (Rotation in Ekman layer)	Same as Leith
Surface Heat Flux	$F_T = C_T |v_s|(T_3 - T_{s+1})$	Same as Leith	Same as Leith	
b. Coefficient of vortage convection C_T gm cm⁻³	10^{-5}		—	
c. Radiative Heat Influx	Temperature in each of 6 layers due to radiative heat influx; solar radiation is function of latitude, position of sun and empirical function of quantity of H_2O in layer. Rate of cooling is independent of latitude and atmospheric conditions, but is empirical function of quantity of H_2O in layer.	Solar radiation is function of latitude, position of sun and altitude. 12% energy absorption by upper layer; 15% energy absorption by lower layer; 73% energy absorption by earth; heat flux from earth to atmosphere 100 cal cm⁻² day⁻¹; atmospheric cooling an empirical function of altitude and temperature with allowance for average cloud conditions.	$\left(\dfrac{dq}{dt}\right)_{rad} = f(y) - C_3 \dfrac{\phi_1 - \phi_3}{T_a}$ wherein $f(y)$ - function of latitude y; C_3 - constant; T_a - rad. equil. temp. $\approx 251 - 259 °K$; ϕ_1, ϕ_3 - geopotentials for two levels. Assume: (a) heat distributed along vertical with aid of large scale movements and radiation so that stability parameter does not vary. (b) earth surface is black body.	Absorption by water vapor with constant relative humidity (60%); vertical infrared heating/cooling; integral formulation depending on pressure and temperature.
Moisture field (Refs. 1, 5)*				
a. Heat Influx due to phase transfer of H_2O	Creates additional heat source	Not taken into account	Reduces stability parameter to 80% and creates additional heat source.	Additional heat source. Released latent heat computed assuming complete saturation. Corrected with empirical "efficiency factor" that reduces heat influx.
b. Calculation of Humidity Field	Calculation as to condensation, precipitation and small scale processes.	Humidity at mean climatic field, determined by temperature of underlying surface.	Not calculable. Manabe and Strickler use mean climatic	Not calculable

99

(transfer of R_2U)			Corrected with empirical "efficiency factor" that reduces heat influx.
b. Calculation of Humidity Field	Calculation as to condensation, precipitation and small scale processes.	Humidity at mean climatic field, determined by temperature of underlying surface.	Not calculable
c. Clouds and Rain	Region of generation of latent heat of condensation	Manabe and Strickler use mean climatic humidity field with 3 layers of clouds shielding solar radiation and being source for long wave radiation	Average effect on radiation field
	Average effect on radiation field	Produce fixed latitudinal averaged latent heat source	Space-centered "diffusing-leapfrog", 3-level leapfrog for 11½ steps followed by one Lax-Wendroff diffusing step for the prognostic equations. Data stored at two time levels.
Finite difference scheme (Refs. 1, 4, 5)*	Explicit; forward directed time difference with respect to time; central difference with respect to space: splitting to resolve 3-D difference into two 2-D differences; vertical derivatives by directed difference:	Explicit; backward directed time difference; forward directed difference according to $\frac{du}{dt} \approx F(u)$ in 2 steps	Implicit scheme: central difference with respect to time and space; non-linear stability by friction.
	(1) Prognostic quantities: T, c, u, v	$u_{t+\delta t}^* = u_t + \delta F(u_t)$ $u_{t+\delta t} = u_t + \delta F(u_t^* + \delta t)$ Invariants:	Invariants: (a) potential temperature (b) relative angular momentum Iteration: stereographic mapping.
		(a) total energy for an adiabatic atmosphere	
	Known at t_0; compute in λ, t, to $(t_o + \frac{\delta t}{2})$; then compute in φ, z to $(t_o + \delta t)$	(b) total energy for adiabatic atmosphere	
		(c) total mass	
	(2) S_H, H compute at semiwhole number steps	(d) potential temperature	
		(e) mean vortex	
	(3) V_z, ω compute at whole numbered steps	(f) mean square vortex Stable to nonlinear instability (no use of friction)	
	(4) From V_z, ω, compute T_{dry}		
	(5) From T_{dry}, compute Humidity$_{dry}$		
	(6) From T_{dry}, Humidity$_{dry}$, compute condensation		
	(7) Compute surface p_s, V_H		
	(8) From p_s, V_H, compute potential temperature		
	CFL criterion satisfied throughout.		CFL criterion satisfied throughout
Computational Grid (Refs. 1, 4, 5)*			
a. Space Interval	$\Delta\lambda = 8^\circ - 80^\circ$ $\Delta\theta = 8.75^\circ$ 10 20 40°	9° 7°	$\Delta\phi = \frac{1}{9}$ so that, for 9 levels, 5° (coarser at poles)
$\Delta\theta$ Δp	0.1 to 1 bar (6 levels)	500 mb (2 levels)	$\rho - \rho_0 = \sigma^2 (3 - 2\sigma)$ 6 km (2 levels)
b. Grid spacing km	556	889	556	556
c. Grid Number (NCVIRH)	2592	1006	7200	2592
d. Time Interval	10 min	12 min	6 min	5 min
Computer Capacity (Refs. 1, 4, 5)*			
a. Total Number of Mesh	$1.5(10)^4$	$2(10)^3$	$1.5(10)^4$	$6.5(10)^4$
b. Number points for one hour forecast	$9.5(10)^4$	$1(10)^4$	$9.5(10)^4$	$6.5(10)^5$
c. Forecast vs forecast	1 year	1 year	60 days	100 days
d. Machine Type	IARC (1.2 STRETCH), IBM 7030	IBM 7094	IBM 704 / IBM 7090	CDC 6600
e. Machine time/forecast day	2.4 hr	1.7 hr	2.5 hr / 20 min	

*References:
1. Smagorinsky, J., Inverse atmos. Ocean Physics, Series 1, No. 12, pp. 1220-1254, 1962.
2. Report of the Study Conference on The Global Atmospheric Research Program (GARP), Appendix 1, pp. 1-39, World Meteorological Organ., 1967.
3. Gambo, N. A., K. Spielberg, IBM Journal, Vol. 11, pp. 312-336, 1967.
4. Kelley, H. C., IBM Journal, Vol. 11, pp. 584-600, Nov. 1967.
5. Mintz, A., and Y. Arakawa, Monthly Weather Review, Vol. 95, No. 7, pp. 389-402, 1967.

equations are solved by a progressive marching method, as outlined earlier in this section, we might expect a local linearization to have global relevance when the finite difference mesh is sufficiently fine. Continuity of the true solution is in fact ensured by inclusion of the diffusive effects of viscosity and thermal conductivity.

A discussion of linear stability can be based on the wave nature of the linearized equations for the horizontal motion as described in "Hydrodynamic Theory of Wave Motions in the Troposphere" of Volume IV.

Atmospheric wave motions are classifiable into these categories:

1. Acoustic waves
2. Gravity waves $\qquad$ (8.12)
3. Inertial waves

Actually acoustic waves have been eliminated in the formulation 8.2 - 8.7 of the equations, by virtue of the hydrostatic assumption, and the irrelevance of sound waves to atmospheric circulation is well established, at least for the troposphere. The main contributor to the atmospheric circulation are the inertial waves, and in fact, in the early approximations of atmospheric circulation only the inertial waves were included. The advent of greater computer capacity allowed inclusion of both gravitational and inertial modes, as in Eqs. 8.2 - 8.7.

It was shown by Courant, Friedrichs and Levy in 1928 that a forward differencing scheme, i.e., one for which, in one dimension,

$$\frac{\partial u}{\partial t} = \frac{u_j^{n+1} - u_j^n}{\Delta t}$$

and

$$\frac{\partial^2 u}{\partial t^2} = \frac{u_{j+1}^n - 2u_j^n + u_{j-1}^n}{(\Delta t)^2}$$

(8.13)

is stable (and convergent) as long as

$$c \frac{\Delta t}{\Delta x} \leq 1 \qquad (8.14)$$

where c is the wave velocity, 8.14 shows that for a chosen grid length Δx, stability requires that the time step be chosen to be less than Δx/c, so that the higher the wave velocities, the shorter is the time step that has to be used. The velocities for the three waves in Eq. 8.12 have maximum values in the troposphere of about 300 m/sec for the accoustic mode, 150 m/sec for the gravity wave and 10 m/sec for the inertial wave. The corresponding maximum allowable time steps given by Eq. 8.14 are 15 min, 30 min, and 8 hr, respectively. The actual figures for the full linear fluid dynamic equations are reduced from these values by two-dimensional effects and by advection. The latter results in 8.14 being modified to

$$(|\bar{v}| + c) \frac{\Delta t}{\Delta x} \leq 1 \qquad (8.15)$$

where $|\bar{v}|$ is the magnitude of the flow velocity at the point in question. The greatest reduction in Δt that results in using 8.15 in place of 8.14 occurs for the inertial wave, since its velocity is least.

In addition to a stability criterion involving the wave nature of the equations, a stability criterion can also be formulated for the diffusive part, i.e., for the viscous and thermal conductivity terms. The linear stability condition for this case is

$$\sigma \frac{\Delta t}{(\Delta x)^2} \leq 1 \qquad (8.16)$$

in which σ is a diffusion coefficient. The finite difference scheme is again of the forward type, as described by Eq. 8.13. In application 8.16 is usually less severe than 8.15, so that diffusive terms do not control the choice of grid size. An example of the use of 8.16 is considered for the complete atmospheric model (discussed later), not just for the troposphere.

The primitive Eqs. 8.2 - 8.7 exclude acoustic waves so that the controlling factor in determining the choice of time step is the gravity wave speed. The time steps listed in Table 8 for the current

atmospheric circulation models have been selected on the basis of a gravity wave stability requirement.

There are forms of finite difference approximations that can reduce or eliminate linear instability. Backward and central differencing methods when applied to wave and diffusion equations fall in this category. However, such systems result in implicit rather than explicit difference equations, so that a simple marching process for carrying through the finite difference solution is no longer possible, and solution of sets of simultaneous equations is required. This is usually regarded as sufficiently time consuming that explicit equations are preferred, even at the cost of the smaller time steps that are needed for stability of the latter.

The numerical simulations listed in Table 8 employ a variety of differencing techniques, the choices made involving compromises between stability requirements, truncation error and computation time for the problem of interest. All these approaches can be analyzed in terms of linear approximations for stability, and result in criteria exemplified here by 8.15 and 8.16. Nonlinear instabilities can also influence the type of finite difference equations used; the factors involved here are strongly linked to the sub-grid scale effects of turbulence discussed earlier, and the next paragraph will discuss these jointly.

Nonlinear Effects and Stability

The first attempts to solve the primitive equations showed up instabilities of an unanticipated variety, not predicted by the linearized equations. A possible cause for their appearance was suggested by Phillips (1959), and explained by him in terms of a simple nonlinear model equation, it being assumed that a similar result would apply also to the complete equations. The essence of Phillips argument is that nonlinear mixing (i.e., the product) of two different frequency wave components of the solution leads to beat frequencies; if the wavelength of one of these should happen to be less than the grid size (so that it is not resolved by the

finite difference mesh), this will be misinterpreted by the finite difference equations as a wave of length greater than the grid interval and will appear in the solution. The effect of finite differencing on such a nonlinear phenomenon is thus to introduce specious wave modes, and in physical terms this implies the false introduction of energy in the solution that should in fact be unresolved within the sub-grid size motions. Phillips was further able to show that the effect could be cumulative, and hence lead to instabilities that could be slowed down, but not eliminated by reducing the grid size.

A method employed by Phillips, and also by several of the numerical schemes summarized in Table 8, for controlling this form of computational instability is to add smoothing to the system by the introduction of friction terms and dissipation. The latter are represented in the nonlinear fluid dynamic Eqs. 8.2 - 8.5 by the terms F and $\dot{v}$. As discussed earlier, the magnitudes assigned to these quantities have, in many instances of atmospheric modeling, been chosen, not by physical arguments concerning the nature of the sub-grid scale stress effects, but empirically by requirements that nonlinear computational instability be eliminated. Unfortunately, in many cases it has been difficult to decide which of the fluctuations observed in the numerical solutions were a result of numerical instabilities, and which corresponded to natural instabilities of the atmosphere. Since the correct physical representation of the sub-grid scale effects is not known with certainty, but is of the same form as that required for numerical stability, the situation can become obscured very rapidly. In particular, the longer the desired prediction time of the simulation the more important are the sub-grid scale effects physically, and the greater is the need for mathematical damping of possible numerical instabilities.

The resolution of this difficult problem requires not just a better method of dealing with numerical instability, but a more adequate description of the sub-grid scale dynamics. The importance of the latter for long-term weather prediction is currently a matter of highest interest and priority since it involves the question of the ultimate forecasting capability of the presently envisaged numerical forecasting

schemes. The central question here is the rate at which energy can be transferred from the small (sub-grid) to the large (synoptic) scale motions. If this figure is as large as some estimates now place it, the current forecasting grid mesh gives a time limit of about three days for weather forecasting. A resolution of this particular question is hoped for in the near future from measurements of the energy spectrum of the atmospheric motions. If long-range forecasting is to become a reality confirmatory evidence for a "gap" in the energy spectrum between the meso and synoptic scales that is believed to exist is needed, not just within the atmospheric boundary layer, where most observations are made, but throughout the troposphere.

This characteristic of the energy spectrum is also important when considering requirements for initial data inputs to the numerical model. Thus, with conventional meteorological sensing instruments, measurements are made at fairly regular time intervals, of the order of an hour, say, but with an output that corresponds to an average value of the meteorological quantity taken over both a small physical volume and a short-time interval (seconds or minutes). When such data are interpreted in terms of much longer dimensions and longer times, corresponding to the space-time grid net for the computational simulation, aliasing occurs. Thus the mathematical model precludes the description of sub-grid scale wavelength and frequencies, to which the measuring instruments are clearly responding. The specific effect of the use of initial data of this variety on the computer simulation depends on the energy spectrum of the motions between the hourly and minute scales. If the high frequency content is low, aliasing is also low, but in fact, as shown in Fig. 37 there appears to be a peak in the energy spectrum around 1 minute. In an analysis by Cort and Taylor (1969), it is demonstrated that with a lower period cut-off of 2 hours in the frequency response of the data input to the computer, an error in the 2-hour period energy spectrum content of the order of a factor of 10 is possible. In terms of the computer simulation this type of result implies very large errors in

the highest frequency (grid scale) description of the simulation, and a subsequent degradation of the prediction accuracy as the prediction time increases. If the atmospheric energy spectrum is indeed as described by Van der Hoven (1957) and Oort and Taylor (1969), the only method of dealing with this difficulty (apart from reducing the time step in the simulation) is to change the method of taking meteorological data, so that a measure sensitive to the highest frequencies but averaged over space and time steps corresponding approximately to the grid mesh size of computation is obtained.
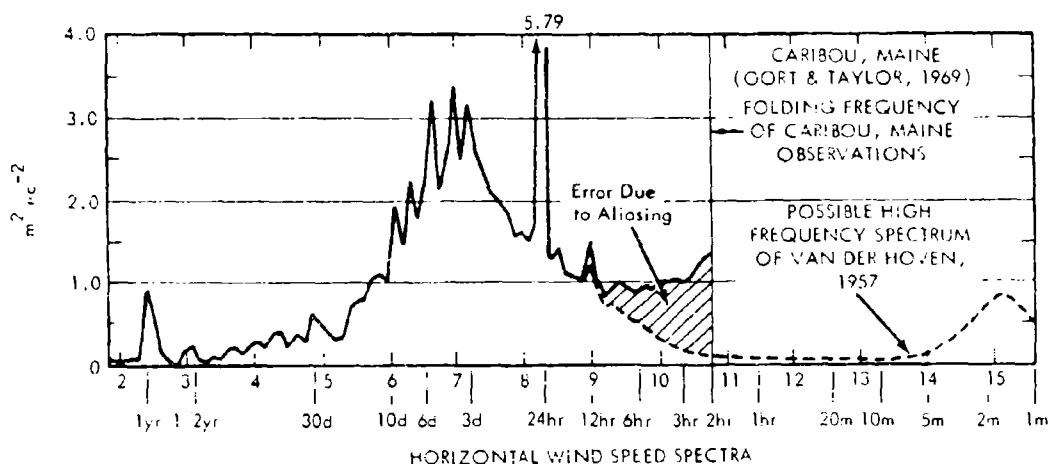
FIGURE 37. Results of an Attempt to Correct the Spectrum at Caribou, Maine, for the Effects of Aliasing from Periods Between 1 Min (the Basic Averaging Period of the Wind Reports) and 2 Hr (the Nyquist Frequency). Frequency F in Cycles/4096 Days (After Oort and Taylor, 1969)

An alternative method aimed at eliminating nonlinear computational instability is the use of energy conserving finite difference schemes. Thus, if the description given by Phillips is accepted, nonlinear instability is accompanied by a physically incorrect increase in energy in some wavelengths of the motion, so it might be ___d that a finite difference scheme that conserves energy could avoid the instability. In fact, the finite difference method used in the Mintz-Arakawa model

(see Table 8) was designed specifically to accomplish this. By the placing of certain integral restraints, not just total energy, but vorticity and zonal momentum are conserved exactly in this model for a frictionless non-dissipative atmosphere. The results of numerical computations with this system show no evidence of instabilities, even in the absence of dissipative terms.

An analogous approach is taken in the Kasahara-Washington model (see Table 8) where a Lax-Wendroff energy-conserving finite difference scheme is used. The nonlinear stability of this method, however, has not been demonstrated.

Whichever of the finite difference schemes is used, there remains a doubt as to its mathematical convergence and stability properties, since they are all too complex to allow rigorous mathematical proof, and basically the test of any one of them has been made by a trial run and comparison of the results with the actual atmosphere. Unfortunately, natural irregularities of the atmosphere are so prevalent that such a comparison is never perfect and there is always the possibility that some of the variations predicted by the model are of a mathematical and not a physical variety. In the final analysis, and in the absence of mathematical convergence proof, the only test of the numerical solution that approaches conclusiveness is a systematic series of trial calculations in which all initial and boundary conditions are kept the same while the grid mesh dimensions are changed. The large running times of the presently formulated atmospheric circulation models have prevented a test of this type from being made for any of them.

Boundary Conditions

The system of Eqs. 8.2 - 8.8 or its finite difference representation has to be supplied with suitable boundary conditions. The simulations that are of concern here are global, so that no lateral boundary conditions need be specified. The upper altitude limit for tropospheric models is at the tropopause; it is assumed that there is no influence of the upper atmosphere acting at the boundary on the troposphere. The lower boundary condition is normally applied above

107

the Ekman layer, rather than at the earth's surface. Hence the
boundary conditions have to allow for the turbulent transports of
heat and momentum that occur in the Ekman and Prandtl layers between
the earth and the lowest horizontal finite difference mesh surface.
The semi-empirical expressions that decide these effects are con-
tained in the following lower boundary conditions:

$$\left. \begin{array}{l} \dfrac{\partial u}{\partial z} = C_D \, u_s \, \sqrt{u_s^2 + v_s^2} \\[2ex] \dfrac{\partial v}{\partial z} = C_D \, v_s \, \sqrt{u_s^2 + v_s^2} \\[2ex] F_T = C_T \, (T_s - T_z) \, \sqrt{u_s^2 + v_s^2} \end{array} \right\} \qquad (8.17$$

Here F_T is the vertical heat flux, T_G the ground temperature, C_D the
surface friction coefficient, and the subscript s refers to values at
the "surface", i.e., at the outer edge of the lower, Prandtl layer.
The boundary layer specification is completed by adding the condition
$w = 0$ to 8.17.

The surface velocities u_s and v_s are usually obtained by linear
extrapolation from the solution at higher levels, though Smagorinsky
uses a more sophisticated extrapolation method that allows for rotation
of the flow through the Ekman layer (cf. Table 8). Additional terms
for the vertical heat flux can arise if humidity and water vaporization
effects are allowed for. Indeed, if they are, their contributions also
must be included in the heat source term q in Eq. 8.5. Volume IV dis-
cusses this briefly, and an indication of how the humidity effects are
allowed for in the various models is given by Table 8.

Characteristics of Current Tropospheric Numerical Simulations

Table 8 is a listing of some of the characteristics of the four
primitive global numerical circulation simulations for the troposphere
that have been constructed to date. These models are used, not for
operational forecasting, but for development of forecasting techniques
for the study of climatic problems. Other less comprehensive models
are used by the Weather Bureau for daily forecasting in the United

States; the Air Force and the Navy have comparable models for Service use. These operational weather prediction models are not global in coverage, and hence of less interest for this report than the larger global simulations, since it is probable that upper atmospheric simulations require very large if not global coverage.

All the simulations use the primitive equations, 8.2 - 8.7, with empirical or semi-empirical values for the stress terms F_x and F_y, and $\dot{}$, and heat source inputs to q from radiative heating and from the moisture field. The latter contributions can be treated in great detail and complexity; indeed there have been several large-scale numerical simulations of radiative transfer in the atmosphere, in which the fluid motions are ignored. A brief description of the type of radiative sources and sinks taken for the tropospheric circulation models is included in Table 8; a further general discussion of this topic is contained in Volume IV.

Also shown in the table are the principal characteristics of the finite difference schemes used, their computational properties and machine running times. A sample of the sequence of operations run through for solving the finite difference equations is illustrated with the Leith model.

Extension to Upper Atmospheric Circulation

The survey of the tropospheric circulation simulation problem given above illustrates the considerable magnitude of that task. From the figures quoted in Table 8 for machine requirements one might guess that an extension of the tr ospheric model to include stratospheric circulation would place the computational load outside the capabilities of present day computers. Besides the increase in volume coverage implied by increasing the altitude span of the simulation, the greater number of molecular constituents above the tropopause and the need for inclusion of their variation through chemical reactions as well as their radiative properties, lead to an enormous increase in computer requirements for simulation. Later in this section estimates will be made to indicate the scope of the problem; these indeed

show that present day computer capacity is inadequate for full global simulation, but that the next generation computers should be able to handle the required circulations.

An indication of the increased complexity of the equations for the upper atmosphere can be judged from those listed in Volume IV under "Physics of the Thermosphere and Ionosphere." These include, not just the effects of chemical changes, but the electrodynamic body forces that are needed to account correctly for the dynamics of the ionized constituents of the upper atmosphere. With a multicomponent fluid, momentum and energy equations are required for each species, and there are in addition rate equations linking them and ohmic loss equations for the ionized components. It should particularly be noted that the hydrostatic assumption is no longer applicable for the upper atmosphere, due to the presence of large vertical winds, so that in place of the Richardson Eq. 8.8, there now appears a fourth prognostic equation for the vertical acceleration. In general, the high wind velocities are the source of gravity wave motions that constitute an important element in upper atmosphere dynamics.

In addition to these additional features of the upper atmosphere which obviously can be a source of difficulty in the numerical mathematics of the simulation, the state of knowledge of the physics of the upper atmosphere has to be considered in assessing the feasibility of a model. Up to about 100 km it appears that this is sufficient, and above about 200 km, where plasma effects dominate, it is probable that the atmosphere is also sufficiently well understood. However, our knowledge of the processes occurring in the highly complicated region between 100-200 km, in which an involved series of coupled chemical changes take place, may not yet be adequate for use in a numerical simulation.

The potential availability from satellite measurements of data at space and time intervals suitable for computational simulation of the global atmosphere and its winds is evidenced by the tabulation of measurement accuracies given in Table 3.

On the positive side, however, competence to address the problem is improving steadily as evidenced by progress of the next generation computers (ILLIAC IV) and by the steady advance of understanding of the physics of the upper atmosphere. Moreover, for most of the DoD needs, which have been elaborated in Volume II the need is for "analysis," that is, a description of the present condition of the atmosphere in the light of observations currently made as opposed to "prediction" of its condition at some future time based on the analysis as an initial condition. Analysis is easier to do than prediction.

On the strength of the positive arguments, and with knowledge of the negative arguments, the scale of computational effort required for a simulation of the upper atmosphere to an altitude of, say, 200 km is considered. It is first necessary specify in time and in distance the computational grid spacing for which some criteria are given in Table 9. These criteria lead to the conclusion that the computation should be carried out with a spacing which is vertically less than about 10 km, horizontally less than 1000 km, and at time steps which are less than 100 sec. A better simulation than the minimum described above would employ a grid specification of 1000 km, a vertical spacing of 7 km, and a time step of 10 sec.

Shown in Table 10 is an estimate of the number of variable points required for upper atmosphere simulation in the altitude ranges up to 200 km. The number of points which would be required in the vertical grid varies from one altitude region to another according to Nyquist criterion applied to the temperature stratification. By the Nyquist criterion, at least two data points are required for each cycle of the variation encountered. In each case, about 800 points are required in the horizontal grid for a 100 km or 9-deg spacing.

The number of dependent variables per point for each of the atmospheric regions is of course different depending upon the significant variables, i.e., components of velocity vectors, pressure, density of principal contituents, and heat absorption by principal atmospheric absorbers. The total number of dependent variables per horizontal grid

TABLE 9. CRITERIA FOR GRID SPECIFICATION

	Δx (m)	ΔZ (m)	Δt (sec)
TEMPERATURE STRAT (NYQUIST)		$\leq 10^4$	
HORIZ. GRAV. WAVE (ELIASSEN) $\quad \Delta x > 2 V_H \Delta t \quad V_H \approx 10^3 \text{ m sec}^{-1}$	$> 2(10)^3 \Delta t$		
VERT. GRAV. WAVE $\quad V_Z \sim 0.01 V_H$		$> 20 \Delta t$	
SPECTRAL DISTRIBUTION			$< 10^2$
COMPUTATIONAL STABILITY $\quad \Delta x > \sqrt{2\sigma \Delta t} \quad \sigma = \frac{\lambda}{C_V} \geq 3.75 \times 10^{-8} \text{ m}^2 \text{sec}^{-1}$	$> 2.7(10)^{-4} \sqrt{\Delta t}$		
LIMITS FOR $\Delta t = 10$ sec	$> 2(10)^4$	$200 \leq \Delta Z \leq 10^4$	10
TRIAL VALUES - COMPLETE SIM.	$(10)^6$	$7(10)^3$	10
TRIAL VALUES - MIN. SIM.	$(10)^6$	$(10)^4$	10^2

TABLE 10. VARIABLE POINTS FOR UPPER ATMOSPHERE SIMULATION

	ALTITUDE RANGE (KM)				
	0-20	20-50	50-90	90-130	150-200
INDEPENDENT VARIABLES	4 (r,θ,λ,t)	4 (r,θ,λ,t)	4 (r,θ,λ,t)	4 (r,θ,λ,t)	4 (r,θ,λ,t)
NUMBER, POINTS IN HORIZ. GRID (10^3 km or 9 deg spacing)	800	800	800	800	800
NUMBER, POINTS IN VERT. GRID (7 km spacing)	3	4	6	9	7
DEPENDENT VARIABLES PER POINT	10 (U,V,W,N,p n_{CO_2}, n_{H_2O}, q_{H_2O}, q_{CO_2}, q_{SURF})	40 (U,V,W,N,p n_N, n_{N_2}, n_{O3P}, n_{O1D}, n_{O_2}, n_{O_3}, n_{OH}, n_H, n_{H_2O}, n_{HeO_2}, n_{HO_2}, n_{NO}, n_{NO_2} + 6 q's + 13 K's)	40 (U,V,W,N,p n_{N_1}, n_{N_2}, n_{O3P}, n_{O1D}, n_{O_2}, n_{O_3}, n_{OH}, n_H, n_{H_2O}, n_{HeO_2}, n_{HO_2}, n_{NO}, n_{NO_2} + 6 q's + 13 K's)	20 (U,V,W,N,p n_{N_2}, n_N, n_{O3P}, n_{O1D}, n_{O_2} + 3 q's + 5 K's)	20 (U,V,W,N,p n_{N_2}, n_N, n_{O3P}, n_{O1D}, n_{O_2} + 3 q's + 5 K's)
DEPENDENT VARIABLES $6(10)^5$	$24(10)^3$	$128(10)^3$	$192(10)^3$	$144(10)^3$	$112(10)^3$

point in the altitude range from 0-200 km is approximately 6×10^5. On the basis of the data given in Table 10, there are shown in Table 11 estimates of computer requirements for both the complete simulation and for a minimum simulation of a more restricted nature. By comparison are analogous estimates for current simulations (NAS-NRS Publication 1350, 1966) of turbulence, convection, tropospheric circulation, and ocean circulation. On the assumption that no one can justify 830 days of computer time to simulate 100 days of upper atmosphere circulation, it is plain from Table 11 that current computers, represented by the CDC-6600 which has an operation time of 600 nsec per operation, are clearly inadequate for the purposes of simulating the global upper atmosphere. Such computers as indicated by the circle require approximately 390 hr of computer simulation time for each 100 days of tropospheric weather simulated.

TABLE 11. ESTIMATES OF COMPUTER REQUIREMENTS

FILTERING APPROX	UPPER ATMOS. SIMUL.		CURRENT SIMULATIONS (NAS-NRC PUBL. 1350 1966)			
	COMPLETE SIMULATION	MINIMUM SIMULATION	TURBULENCE	CONVECTION	TROPO. CIRC.	OCEAN CIRC.
FILTERING APPROX	FOURIER	FOURIER	BOUSSINESQ	BOUSSINESQ	HYDROSTATIC	GEOSTROPHIC
DIMENSIONALITY	4	4	4	4	4	4
DEP. VARIABLES	10 – 40	15	$4(u,v,w,r)$	$5(u,v,w,T,r)$	$4(u,v,T,r)$	$4(u,v,T,s)$
NUMBER, VERTICAL LEVELS	30 (7 KM)	20 (10 KM)	30	100	10	10
NUMBER, HORIZ. POINTS	$600(10^3$ KM)	$800 (10^3$ KM)	10^4	10^4	10^4	10^4
TIME STEP (sec)	10	10^2	0.001	5	300 (5 MIN)	$1.8(10)^4$ (5 Hr)
SIMULATED EXP. TIME (sec)	10^7(100d)	10^7(100d)	10	$3.6(10)^4$ (5 Hr)	10^7(100d)	10^9 (30 Yr)
DEP. VER. PER TIME STEP	$6(10)^5$	$2.4(10)^5$	10^6	$5(10)^6$	$4(10)^5$	$4(10)^5$
TIME STEP PER EXP.	10^6	10^5	10^4	$2(10)^3$	$3(10)^4$	$6(10)^4$
DEP. VAR PER EXP.	$6(10)^{11}$	$2.4(10)^{10}$	10^{10}	10^{10}	$1.2(10)^{10}$	$2.4(10)^{10}$
COMP. OPER. PER EXP. (200 OPER/DEP. VAR)	$1.2(10)^{14}$	$4.8(10)^{12}$	$2(10)^{12}$	$2(10)^{12}$	$2.4(10)^{12}$	$4.8(10)^{12}$
COMP. TIME-CDC6600 (600 nsec PER OPER)	$7.2(10)^7$ ($2(10)^4$ H) (830d)	$2.9(10)^6$ (810H)	$1.2(10)^6$ (330H)	$1.2(10)^6$ (330H)	$1.4(10)^6$ (390H)	$2.9(10)^6$ (810H)
COMP. TIME-ILIAC (sec) (1.2 nsec PER OPER)	$1.4(10)^5$ (39 H)	$5.8(10)^3$ (1.6 H)	$2.4(10)^3$ (40 MIN)	$2.4(10)^3$ (40 MIN)	$2.9(10)^3$ (48 MIN)	$5.8(10)^3$ (1.6 Hr)

The next generation of computers, however, such as the ILIAC IV, expected to be operational in the early 1970's and 500 times as fast, may require only 48 min for a simulation of global tropospheric circulation of 100 days duration. It would also be capable of simulating 100 days of upper atmosphere circulation in 39 hr of computer time commensurate with present-day allocations to other problems.

Smaller scale computations than considered in this estimate are also possible. For example, calculations over a restricted volume, either vertically or horizontally, may be of interest in some applications. In such a case the scope of the computation is reduced, though at the moment, knowledge of the energy transfer rates is insufficient to enable prediction time to be related to the volume of the atmosphere that is simulated.

Alternative numerical methods of solving the equations perhaps should also be considered and a particularly attractive approach from the point of view of the aliasing and sub-grid scale energy spectrum effects is the use of wave number rather than physical space. In such a method a large wave number cut-off, corresponding to the maximum resolvability of the finite difference grid mesh, can be easily applied, thereby avoiding some of the confusion that results with the methods used to date. Prior to the advent of the fast Fourier transform technique such a scheme would have implied excessive computational time, but this now appears no longer to be the case.

Mention should also be made of a different variety of computer simulation that could be considered. This is the problem of analysis, i.e., the estimation of current atmospheric conditions from a limited set of observations, in contrast to prediction, with which the prior discussions in this section have been concerned. Although common in daily meteorological work, it appears that little thought has been given to dealing with this question using numerical methods and the fluid dynamic equations. This question appears to be of potential importance for the upper atmosphere, in which for some applications we may think of current satellite information on atmospheric data being

114

analyzed by computer to give an instantaneous picture of the complete state of the atmosphere. Limitation to analysis, rather than prediction, eases the problem from the point of view of computer capacity requirements and eliminates some of the difficult questions of the propagation of sub-grid scale effects into the synoptic scales.

As was just stated, little attention has been given to this approach, and here we shall just point out a gross difference in the numerical calculation task from that for the prognostic problem. Thus in "Typical Wave Motions" of Volume IV, it was shown that the equations governing the spatial domain could be of a hyperbolic, parabolic or elliptic variety, depending on the region of wave motion involved (inertial, gravitational and acoustic). Thus, assuming these considerations are transferable to the non-linear equations, the solution techniques have to be adjusted according to the domain of solution, and this is quite different from the forecasting problem, in which a straightforward marching technique is always used. Further elaboration and study of the use of this type of analysis need further attention, since it appears to be of potential significance.

To Summarize:

The implicit determination of winds by computational simulation appears to have potential. The justifiable degree of complication in such simulation is questionable requiring further investigation. Certainly the extensive use of computers for the analysis of weather data is amply justified. The analysis of the entire global atmosphere up to an altitude of 200 km seems feasible from the standpoint of the capability of next generation computers which would require no more computer time than the exercise of current problems. Accomplishment may be slowed by the fact that present knowledge of the physics of the upper atmosphere is incomplete.

BIBLIOGRAPHY

Bain, W.C. and M.C.W. Sanford, 1966: "Light Scatter From A Laser Beam at Heights above 40 km," J. of Atmos. and Terres. Physics, Vol. 28, pp. 543-552.

Billik, B., "Survey of Current Literature on Satellite Lifetimes," J. of Amer. Rocket Soc., November 1962.

Bolin, B., ed., "Report of the Study Conference on the Global Atmospheric Research Programme (GARP), ICSU/IUGG-Committee on Atmospheric Sciences and COSPAR and World Meteorological Organization, Stockholm, 28 June-11 July, 1967.

Chubb, T.A. and H. Friedman, "Photon Counters for the Far Ultraviolet," Rev. Science Institute, Vol. 26, p. 493, May 1955.

Champion, K.S.W., "Properties of the Lower Thermosphere: Recent Progress," Paper presented at the Twelfth COSPAR Meeting, 11-24 May 1969 in Prague.

Champion, K.S.W., F.A. Marcos and J.P. McIsaac, "Atmospheric Density Measurements by Research Satellite OV1-15," Paper presented at the Twelfth COSPAR Meeting, 11-24 May 1969 in Prague.

Champion, K.S.W., F.A. Marcos and R.A. Schweinfurth, "Measurements by the Low Altitude Density Satellite OV1-16," Paper presented at the Twelfth COSPAR Meeting, 11-24 May 1969 in Prague.

Champion, K.S.W., personal communication, 1969.

Clemesha, B.R. et al., 1966: "Laser Probing the Lower Atmosphere," Nature, Vol. 209, pp. 184-185.

Clemesha, B.R., G.S. Kent and R.W.H. Wright, 1967: "Optical Radar Evidence for Atmospheric Dust Layers Around 85 km Altitude," Nature, Vol. 214, pp. 261-262.

Clemesha, B.R., G.S. Kent, R.W.H. Wright, "A Laser Radar for Atmospheric Studies," J. App. Meteor, Vol. 6, pp. 386-395, 1967.

Collis, R.T.H., and M.G.H. Ligda, "Note on Lidar Observations on Particulate Matter in the Stratosphere," Journal of Atmos. Sciences, Vol. 23, pp. 255-257, 1966.

Cook, G.E., "Satellite Drag Coefficients," Planetary and Space Science, Vol. 13, No. 10, October 1965.

Courant, R., K.O. Friedrichs and H. Levy, Über die partiellen Differenzengleichungen der mathematischen Physik, Math. Ann., Vol. 100, p. 32, 1928.

DeBra, Danl ; B., "A Comparison of Satellite Drag Measurement Techniques," Second International Conference on Space Engineering, May 1969 (Venice, Italy).

Fiocco, G., and L.D. Smullin, 1963: "Detection of Scattering Layers in the Upper Atmosphere (60-140 km) by Optical Radar," Nature, Vol. 199, pp. 1275-1276.

Fiocco, G., and G. Grams, 1964a: "Observations of the Aerosol Layer at 20 km by Optical Radar," J. Atmos. Science, Vol. 21, pp. 323-324.

Fiocco, G., and C. Columbo, 1964b: "Optical Radar Results and Meteoric Fragmentation," J. Geophysical Research, Vol. 69, pp. 1795-1803.

Fiocco, G., 1965: "Optical Radar Results and Ionospheric Sporadic," E. J. Geophysical Research, Vol. 70, pp. 2213-2215.

Fjelbo, G., and V.R. Eshleman, "The Atmosphere of Mars Analyzed by Integral Inversion of the Mariner IV Occultation Data," Planetary and Space Science, Vol. 16, pp. 1035-1059, 1968.

Fujita, Tetsuya T., "Meteorological Applications of Geostationary Satellites," Outline of Lectures on Satellite Meteorology, Univ. of California Extension Center, May 1969.

Fujita, T., D.L. Bradbury, C. Murmo, and L. Hull. "A Study of Mesoscale Cloud Motions Computed From ATS-1 and Terrestrial Photographs," Univ. of Chicago, Dept. of Meteorology Satellite and Mesometeorology, Research Paper No. 71, March 1968.

Gille, J.C., "On the Possibility of Estimating Diurnal Temperature Variation at the Stratopause from Horizon Radiance Measurements," J. of Geophysical Research, Vol. 73, pp. 1863-1868, 1968.

Gille, J.C., "Inversion of Radiometric Measurements," Bull. of Amer. Meteor. Soc., Vol. 49, pp. 903-012, 1968.

Goody, R.M., Atmospheric Radiation, Clarendon Press, 1964.

Goyer, G.G., and R.D. Watson, "Laser Techniques for Observing the Upper Atmosphere," Bull. Amer. Meteor. Soc., Vol. 49, pp. 890-897, 1968.

Grobecker, A.J., "Ion Chambers for Detection of Ultraviolet," North American Aviation, Inc. Report NAA-SD 66-1338-7, June 1967.

Grobecker, A.J., "Ion Chambers for Detection of Soft X Rays," North American Aviation, Inc. Report NAA-SD 66-1338-8, July 1967.

Grobecker, A.J., unpublished material, now in preparation for publication, 1969.

Hall, L.A., K.F. Damon, and H.E. Hinteregger, "Solar Extreme Ultraviolet Photon Flux Measurements in the Upper Atmosphere of August 1961," Space Research III, Proc. of the 3rd International Space Science Symposium, North-Holland Publishing Co., Amsterdam, 1962.

Hall, R.T., "Analysis of Cloud Cover Over the USSR," ETAC Project 5713, Dept. of Air Force (AFSC), 1968.

Herman, R.M., and P.M. Yarger, "Estimating the Vertical Atmospheric Ozone Distribution by Inverting the Radiative Transfer Equation for Pure Molecular Scattering," J. of Atmos. Sciences, Vol. 26, pp. 153-162, 1969.

Herzberg, G., "Molecular Spectra and Molecular Structure: I Spectra of Diatomic Molecules," D. Van Nostrand Co., New York, 1964.

Hinteregger, H.E., L.A. Hall, and G. Schmidtke, "Solar XUV Radiation and Neutral Particle Distribution in July 1963 Thermosphere," Space Research V, North-Holland Publishing Co., Amsterdam, 1964.

Holmstrom, I., "On a Method for Parametric Representation of State of the Atmosphere," Tellus, Vol. 15, pp. 127-149, 1963.

Hubert, L.F. and L. Whitney Jr., American Meteorological Society Meeting, New York City, N.Y., 22 January 1969.

Johnson, Michael H., "A Photogrammetric Technique for Finding Winds from Satellite Photos," Annual Report-1967, Dept. of Meteorology, The University of Wisconsin, May 1968.

Kent, G.S. et al., 1967: "High Altitude Atmospheric Scattering of Light from a Laser Beam," J. Atm. Terr. Phys., Vol. 29, pp. 169-181.

King, J.I.F., "Scientific Uses of Earth Satellites," J.A. Van Allen, ed., Vol. 2, p. 133, University of Wisconsin Press, 1956.

Kliore, A. et al., "Occultation Experiment Results of the First Direct Measurements of Mars' Atmosphere and Ionosphere," Science, Vol. 149, pp. 1243-1248, 1965.

Kliore, A. et al., "Atmosphere and Ionosphere of Venus from the Mariner V S-Band Radio Occultation Measurement," Science, Vol. 158, pp. 1665-1690, 1967.

Lusignan, B. et al., SPINMAP Final Report, Stanford University, School of Engineering, Palo Alto, California, June 1966.

Lusignan, B. et al., "Sensing the Earth's Atmosphere with Occultation Satellites," Proc. IEEE, Vol. 57, pp. 458-467, 1969.

McCormick, P.D. et al., 1966: "Backscattering from the Upper Atmosphere (75-160 km) Detected by Optical Radar," Nature, Vol. 209, pp. 798-799.

McCulloch, A.W., and W.L. Smith, "Proposal for a High Resolution Temperature Sounder for NIMBUS F," NASA (GSFC) Proposal, January 1969.

McKee, T.B., R.I. Whitman, and J.J. Lambiotte, Jr., "A Technique to Infer Atmospheric Temperature from Horizon Radiance Profiles," NASA TN D-5058, 1969.

Murgatroyd, A.J., "General Circulation of the Mesosphere," personal communication, Meteorological Office, England, University of Illinois, Third Conference, Meteorological and Chemical Factors in D-Region Aeronomy, 23-26 September 1968.

Nishikori, et al., 1965, "On Observations of the Upper Atmosphere by Ruby Laser," J. Radio Research Lab., Vol. 12, pp. 213-222.

Oort, A.H., and A. Taylor, "On the Energy Spectrum Near the Ground," Monthly Weather Rev., Vol. 97, No. 9, p. 623, September 1969.

Owens, J.C., "Optical Doppler Measurement of Microscale and Velocity," Proc. IEEE, Vol. 57, pp. 530-536, 1969.

Phillips, N.A., "An Example of Non-Linear Computational Instability," in The Atmosphere and the Sea in Motion, Ed: B. Bolin, Rockefeller Inst. Press, p. 501, 1957.

Phinney, R.A., and D.L. Anderson, "On the Radio Occultation Method of Studying Planetary Atmospheres," JGR, Vol. 73, pp. 1819-1827, 1968.

Sandford, M.C.W., "Optical Radar Performance in Atmospheric Scattering," J. of Atmos. and Terres. Phys., Vol. 29, pp. 1651-1657, 1966.

Schotland, R.M. et al., "Optical Sounding II, Final Report - Part I. Study of Active Probing of Water Vapor Profiles and Results of Experiments," New York University, School of Engineering and Science, 1965.

Smith, W.L., "Statistical Estimation of the Atmosphere's Pressure Height Distribution from Satellite Radiation Measurements," Paper presented to IUGG/WMO Symposium on Radiation, including Satellite Techniques, Bergen, Norway, August 1968.

Suomi, V.E., personal communication, 1969.

Suomi, V.E., and T.H. Vonder Haar, Third Quarterly Report, Contract NAS 5-11542, 1 December 1968-28 February 1969. Space Science and Engineering Center, the University of Wisconsin.

Swider, W., Jr., "The Determination of the Optical Depth at Large Solar Zenith Angles," Planetary and Space Science, Vol. 12, pp. 761-782, Pergamon Press, New York, 1964.

Twomey, S., "On the Deduction of the Vertical Distribution of Ozone by Ultraviolet Spectral Measurements from a Satellite," J. of Geophysical Research, Vol. 66, pp. 2153-2162, 1961.

Vonder Haar, T.H., "Meteorological Applications of Reflected Radiance Measurements from ATS I and ATS III," 49th Annual Meeting of the American Meteorological Society, New York, January 1969.

Wark, D.Q., and H.E. Fleming, "Indirect Measurements of Atmospheric Temperature Profiles from Satellites: I. Introduction," Monthly Weather Review, Vol. 94, pp. 351-362, 1966.

APPENDIX A

REVIEW OF RECENT U.S. EFFORTS TO MEASURE ATMOSPHERIC
PARAMETERS IN GLOBAL AND NEAR REAL-TIME SCALES
AT LOW ALTITUDES IN THE ATMOSPHERE

CONTENTS

APPENDIX A

1. Introduction

The capability of achieving a refined knowledge of the variations
of atmospheric conditions on a global scale and near real-time is
within the grasp of modern civilization through the use of meteoro-
logical satellites and high speed computers. Such refined knowledge
in the above space and time scales would be derived from a process that
involves two phases: (1) intermittent global measurements in near
real-time of atmospheric conditions from mainly π erological satel-
lites,* and (2) subsequent predictions of the variations of the atmos-
pheric parameters in the lower atmosphere (i.e., the troposphere or
altitudes up to about 8 nmi) during a time that appears to be limited
to about three weeks (Refs. 1,2). The overall economical reward from a
refined knowledge of atmospheric conditions that would allow even a one
week weather prediction has been estimated in billions of dollars as a
consequence of improved management of water resources, agriculture,
surface transportation, retail marketing, the lumber industry, etc.
(Ref. 3).

The need for global measurements becomes clear from the rather
straightforward formulation of the air motion within the troposphere,
i.e., the motion of air on a rotating earth receiving shortwave radia-
tion from the sun and returning longwave radiation to space. The
dependent variables of the problem are the three components of the air
velocity (i.e., wind), the pressure, temperature, air density, and
water vapor. The independent variables are given by the three space

---

*Meteorological satellites can reach otherwise inaccessible areas of
the oceans.

coordinates: longitude, latitude, and altitude and the time.* The seven dependent variables are determinable as a function of the four independent variables from the use of seven equations obtained as follows: three momentum equations, the conservation of energy within a nonadiabatic troposphere, the conservation of mass, the equation of state for a real gas with a molecular weight of air, and the diffusion equation for the concentration of water vapor within the troposphere coupled with the partial pressure of water vapor as a function of pressure and temperature. This set of partial differential equations requires initial conditions** for each of the seven variables and boundary conditions** that take into account the energy exchange at the surface of the earth (between the atmosphere and both the ground and the oceans), the orographic effects on the air velocity vector, and the energy exchange at the top of the troposphere. While this set of partial differential equations is difficult to solve even by numerical methods, the feasibility of obtaining numerical solutions from them has already been demonstrated under somewhat restricted conditions (Refs. 2,4 to 7). This feasibility of solution is further demonstrated from the proven success in a somewhat similar numerical situation, i.e., the numerical solution of a quasi-steady flow within laminar hypersonic boundary layers with mass injection from the receding surface of an ablating intercontinental ballistic missile (Refs. 8, 9).

The need for near real-time processing of the global measurements stems from the relative magnitude of the force terms in the momentum equations for the two horizontal components of the air velocity vector, i.e., the time dependent term (which is essential for time predictions) or air acceleration is given by the difference of two nearly equal forces, namely the pressure gradient and Coriolis forces. This fact, together with inherent errors of both experimental and analytical

---

*The pressure and altitude are usually interchanged as the independent and dependent variable, respectively. This result stems from the direct coupling of these two variables through the hydrostatic equation.

**As deduced from satellite and other available data.

nature,[*] puts a limit to the length of time for accurate predictions, i.e., the predicted behavior of atmospheric parameters as derived from initial global measurements. The subsequent use of the equations of motion is estimated to be accurate during a time that is no longer than about three weeks after the measurements (Refs. 1, 2). Hence, the perishable data for the initial and boundary conditions must be utilized in the numerical integrations of the equations of motion in near real-time in order for its utility to be maximized for the prediction of the behavior of the atmospheric parameters during a rather short subsequent time.

While the development of numerical techniques to describe the air motion in different scales within the troposphere is a subject of great interest, the subsequent treatment is limited to the development of meteorological satellites and sensor subsystems for the remote measurement of the initial and boundary conditions in the global and near real-time scales; that is to say, meteorological satellites operating in medium altitude orbits (e.g., in the range from 400 to 800 nmi) and in geosynchronous orbits at 19,300 nmi.

The subjects of interest here include the following: (a) feasibility of remote measurements of the initial and boundary conditions within the required degree of accuracy in a global and real-time scale; (b) chronological developments of U.S. meteorological satellites and sensor subsystems; (c) current projections for the development of sensor subsystems for U.S. meteorological satellites during the forthcoming decade; (d) brief description of the international GARP (Global Atmospheric Research Program) and WWW (World Weather Watch) programs, and (e) conceptual techniques for potential measurements from satellites.

---

[*]Errors in the measurement of initial conditions as well as truncation of the difference equations and rounding off during the numerical integration.

2. Feasibility of Remote Measurements With Appropriate Accuracies

The remote measurement of the initial conditions in a global scale and real-time involve the following variables: geopotential altitude (h) of a given pressure level (p, ir millibars),[*] temperature (T), density (ρ), water vapor (ω), and the three components of the velocity vector (u, v, w in the longitude, latitude, and vertical directions, respectively). Since the density is related to the pressure and temperature through the equation of state for a real gas,[**] the density becomes determined from the pressure and temperature distributions. Likewise, the determination of the three velocity components requires determination of the magnitude of the velocity vector (V), i.e., as fixed by both the magnitude and the direction of the wind vector. The accuracy for the measurement of the initial conditions has been specified by the 1967 GARP study conference as follows (Ref. 11):[+]

a. h(x, y, t), as fixed by a reference pressure with an r.m.s. error of 2 percent.

b. T(x, y, p, t), with an r.m.s. error of $\pm$ 1°C.

c. ω(x, y, p, t), with an r.m.s. error of 10 percent.

d. V(x, y, p, t), with an r.m.s. error of $\pm$ 3 m/sec.

where x denotes the latitude, y the longitude, and t the time. The horizontal resolution of these global measurements was specified at a typical value of about 400 km ($\sim$200 nmi), while the vertical resolution was set at 200 mb in an altitude range corresponding up to 10 mb.[++]

The remote measurements of the boundary conditions involve measurements of the energy exchange at the interface between the

---

[*]As consequence of the interchange of pressure and altitude as the independent and dependent variables, respectively.

[**]The gas constant can be made to include the effect of water vapor in the troposphere, which is at most of the order of 4 percent (Ref. 10).

[+]See Ref. 11 to identify the outstanding membership of this study.

[++]Since one bar or 1000 mb is approximately the standard atmospheric pressure at the surface of the earth, the altitude range extends from the surface of the earth to about 100,000 ft or 16.5 nmi, approximately.

atmosphere and oceans as well as the global radiation balance (i.e., including cloud cover).

It is shown below that the geopotential altitude (h) and the distribution of the temperature (T) within the troposphere are determinable to the desired scales and degree of accuracy from the following two sets of data: (1) radiance measurements from high-resolution infrared sensors on meteorological satellites operating at medium altitude orbits, and (2) on updated statistical sample of data for the geopotential altitude and temperature applicable to the local region of interest. Similarly, the distribution of water vapor (ω) through the lower troposphere is also determinable from remote radiance measurements in the infrared. Potential techniques for the determination of the wind vector are as follows: (a) detecting the motion of cloud elements that move with the wind in the lower troposphere, as observed from geosynchronous meteorological satellites; and (b) using a world-wide network of constant-density balloons distributed at different pressure (i.e., altitude) levels in the upper cloudless troposphere, and tracking the balloons from meteorological satellites.*

3. R.M.S. Errors in the Geopotential Height

It has been shown that the geopotential height or altitude profile is uniquely related to the temperature distribution in the atmosphere by the following mathematical relationships (Ref. 12).

a. The hydrostatic equation, which relates the local drop in pressure with increasing altitude to the local density;

b. The equation of state for a real gas, which relates the local pressure to the local density and temperature;

c. The _empirical_ orthogonal functions (Refs. 13, 14), which indicate that they are statistically stable in that they are nearly invariant with respect to the latitude, longitude, and time.

---

*Potential techniques to measure the wind vector over the oceans involve determination of the sea surface conditions from either microwave measurements or the solar glitter.

127

Thus, subject to the validity of the empirical orthogonal functions as derived from the statistical behavior of the atmosphere, the geopotential height can be specified solely from the temperature profile; which as treated subsequently is determined from radiance measurements from medium altitude orbits.

The above method has been tested by using extensive radiosonde data for four consecutive days. The first three days provided 299 sets of observations, which were used as the required statistical or dependent sample of observations. The fourth day provided data in the form of actual temperature profiles and calculated radiance to be used as postulated measurements; the latter ones were then used in the procedure outlined above to determine calculated temperature profiles. Figure A-1 compares the r.m.s. differences between the radiosonde and calculated values for the geopotential height under clear and cloudy conditions for two assumed values of the random errors in the measurements, i.e., $\sigma_e = 10^{-2}$ and $\sigma_e = 1/4$ ergs/cm^2-sec-strdn-cm^{-1}.* The standard deviation of the errors of the earth's surface radiance observations under cloudy conditions was assumed to be 2 ergs/cm^2-sec-strdn-cm (Ref. 12). Figure A-1 shows that for the most ideal conditions (i.e., clear conditions, availability of ground pressure data, and the smaller σ_e value) the r.m.s. height differences are no more than 20 ft even at the 10 mb pressure; while for the worst conditions (i.e., cloudy and unconstrained or using only statistical considerations) the r.m.s. height differences are no more than 60 ft even at 10 mb. It is of interest to note that for clear conditions, the geopotential height estimates show a significant improvement even for the larger σ_e value when using surface measurements, i.e., the r.m.s. error is reduced to no more than 20 ft at the 200 mb pressure level.

---

*The smaller value represents an unrealistically small value, and is used to illustrate a limit for the degree of accuracy that can be achieved from satellite radiance observations. The high value is only a factor of two smaller from the value that leads to results which do not meet the requirements of meteorology (Ref. 15).
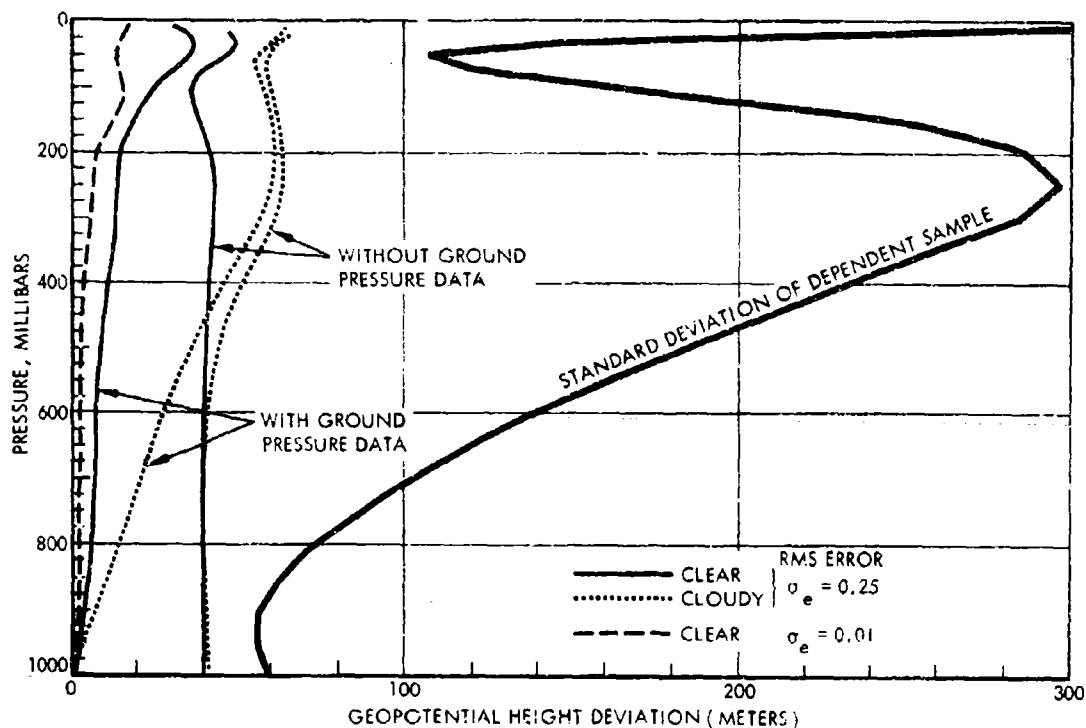
FIGURE A-1. Altitude Deviation of Atmospheric Pressure Levels (in milibars) Derived from Statistical Properties of the Geopotential Height and Satellite-like Radiance Measurements. The altitude deviation is given for clear and cloudy conditions, and the RMS difference between radiosonde observed and radiance calculated values (i.e., σ_e, ergs/cm^2-sec-stdn-cm^{-1}). The smaller value of 10^{-2} for clear conditions defines a limit for the accuracy obtainable from satellite radiance observations, while the larger value ($\sigma_e = 1/4$) is the expected typical value for the SIRS observations (Ref. 12).

4. R.M.S. Errors in the Temperature Distribution

The accurate determination on a global and real-time scales of the temperature distribution in the troposphere from remote radiance measurements in the infrared region of the electromagnetic spectrum has already been shown to be feasible (Refs. 15 to 27) because of the following five factors:

a. The existence of atmospheric "windows" where gaseous absorption is minimal. These windows become useful for the determination of surface temperatures and cloud conditions over

the local regions of interest. Two windows of consequence to the subsequent description of radiometers are one in the interval from 3.5 to 4.1μ, and another one in the 8.0 to 12.5μ range.

b. The presence in the atmosphere of gaseous tracers (i.e., water vapor and carbon dioxide) that are well mixed with the air (with a rather constant mixing ratio) in the altitude range from the earth's surface to the mesopause.

c. The molecular absorption bands (i.e., vibration-rotation and rotational) in the infrared spectrum of the above gaseous tracers. The principal infrared absorber in the atmosphere is water vapor with strong vibration-rotation bands centered near 1.1μ, 1.38μ, 1.87μ, 2.7μ, and 6.3μ as well as rotational bands from 12 to about 65μ. A second gaseous absorber of importance is carbon dioxide with strong vibration-rotation bands centered near 2.7μ, 4.3μ, and 15μ.

d. The sampling of different depths in the atmosphere by using different absorption bands and different zenith angles, i.e., as illustrated in Fig. A-2 for the 15μ carbon dioxide interval for zero and 60 deg zenith angles. This figure shows that as the frequency increases from 695 cm^{-1} (i.e., 14.4μ) to 747 cm^{-1} (13.4μ) the maximum relative atmospheric contribution to radiance measurements take place at approximately the 100 mb, 400 mb, 700 mb, and the earth's surface. A measurement made at a frequency for which atmospheric absorption is intense (e.g., 695 cm^{-1}) records radiation only from the upper part of the atmosphere; the radiation coming from lower down is strongly attenuated and does not reach satellite altitudes. Thus the radiance received at this frequency contains information about the upper regions of the atmosphere. Conversely, measurements made at a frequency of small absorption (e.g., 747 cm^{-1}) detects radiation coming near or at the surface of the earth. The data in Fig. A-2 also indicate the following: (1) a given altitude usually contributes radiation to more than one frequency; because of this inherent redundancy, it is

reasonable to expect that there is a limit on the amount of
information that can be obtained from increases in the spectral
resolution (i.e., the number of frequencies); (2) no informa-
tion can be obtained for altitudes that do not make a reason-
able contribution to the radiance at any frequency; and (3) the
outgoing radiance from a particular frequency is predominantly
from a layer approximately 10 km (~5 nmi) thick, which fixes
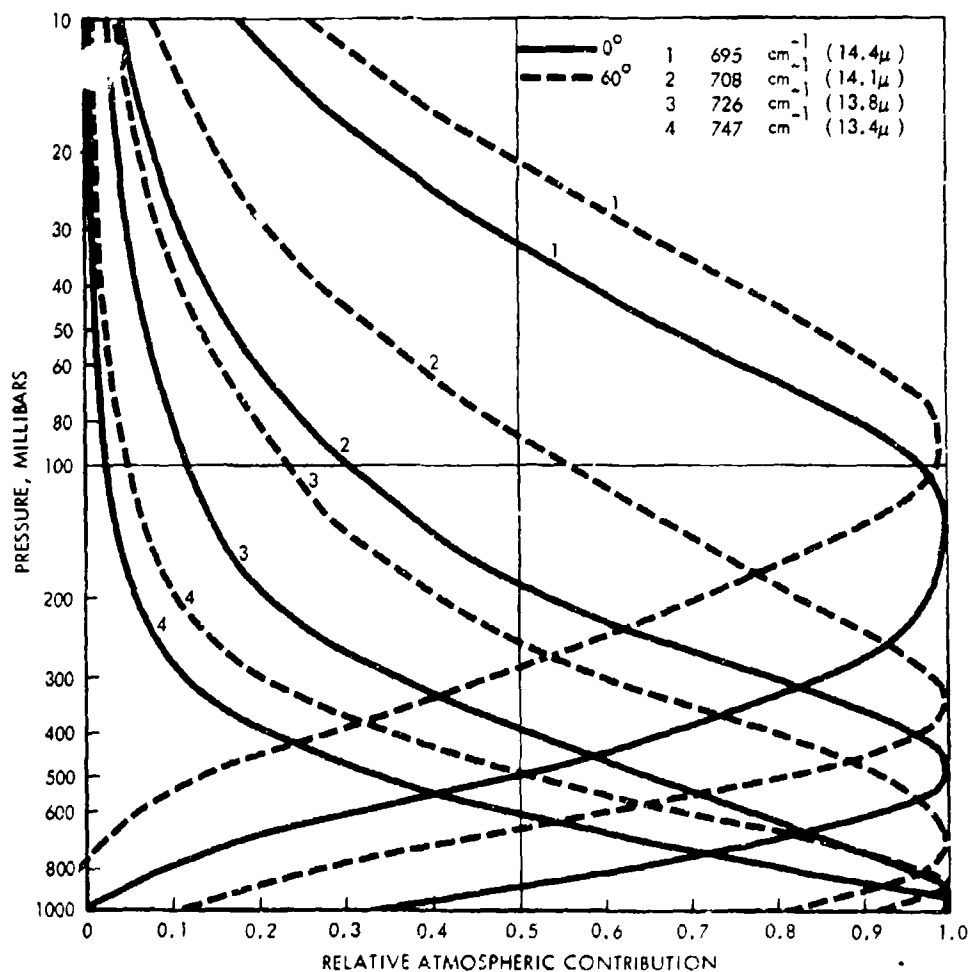the vertical resolution of the deduced temperature distribution
to about this value.

FIGURE A-2. Weighting Functions for the Chosen 15μ CO_2 Spectral Intervals
for Two Different Zenith Angles (Ref. 17)

e. The scanning of radiometers with small fields of view (~10 m
    rad); which allows an increase in the spatial resolution of
    the measurements, and therefore increases the probability for
    radiance measurements through broken clouds. The unique
    advantages of deriving atmospheric temperature profiles
    utilizing data from a High Resolution Infrared R ation
    Sounder (HIRS) are as follows: (1) clouds will   generally
    prohibit accurate profiles to be obtained for the troposphere
    except in the central region of storm systems, and (2) the
    greater number of accurate independent measurements over a
    given area will increase the accuracy of the temperature pro-
    file for that area. A proposed HIRS subsystem for the Nimbus
    F satellite would utilize six different spectral intervals:
    four in the 15μ carbon dioxide band, one in the 6.3μ water
    vapor band, and one in the 11μ window region. The angular
    resolution of the instrument would be 8 m rad, which provides
    a linear resolution on the earth of about 5 nmi at the nadir
    from a spacecraft altitude of 600 nmi. This field of view is
    sufficient for resolving clear cloud interstices as needed for
    deriving accurate tropospheric temperature profiles. The
    radiometer would scan ± 35 deg of nadir angle, to each side of
    the orbital track (Ref. 17). The areas completely free of
    clouds would be identified from a statistical frequency
    analysis of the "window" observations obtained over a rela-
    tively large area (i.e., 150 nmi^2), a method that is based on
    the following factors: (1) the major variations of the window
    radiance measured within such an area would be the result of
    variations of the properties of any clouds within the field of
    view (i.e., amounts, altitude, opacities), and (2) the magni-
    tude of the radiance observations through the clear holes in
    the clouds will be in general higher than those through the
    clouds; as illustrated in Fig. A-3. The figure illustrates a
    frequency histogram of the Nimbus II HRIR (High Resolution
    Infrared) radiance observations (in units of brightness
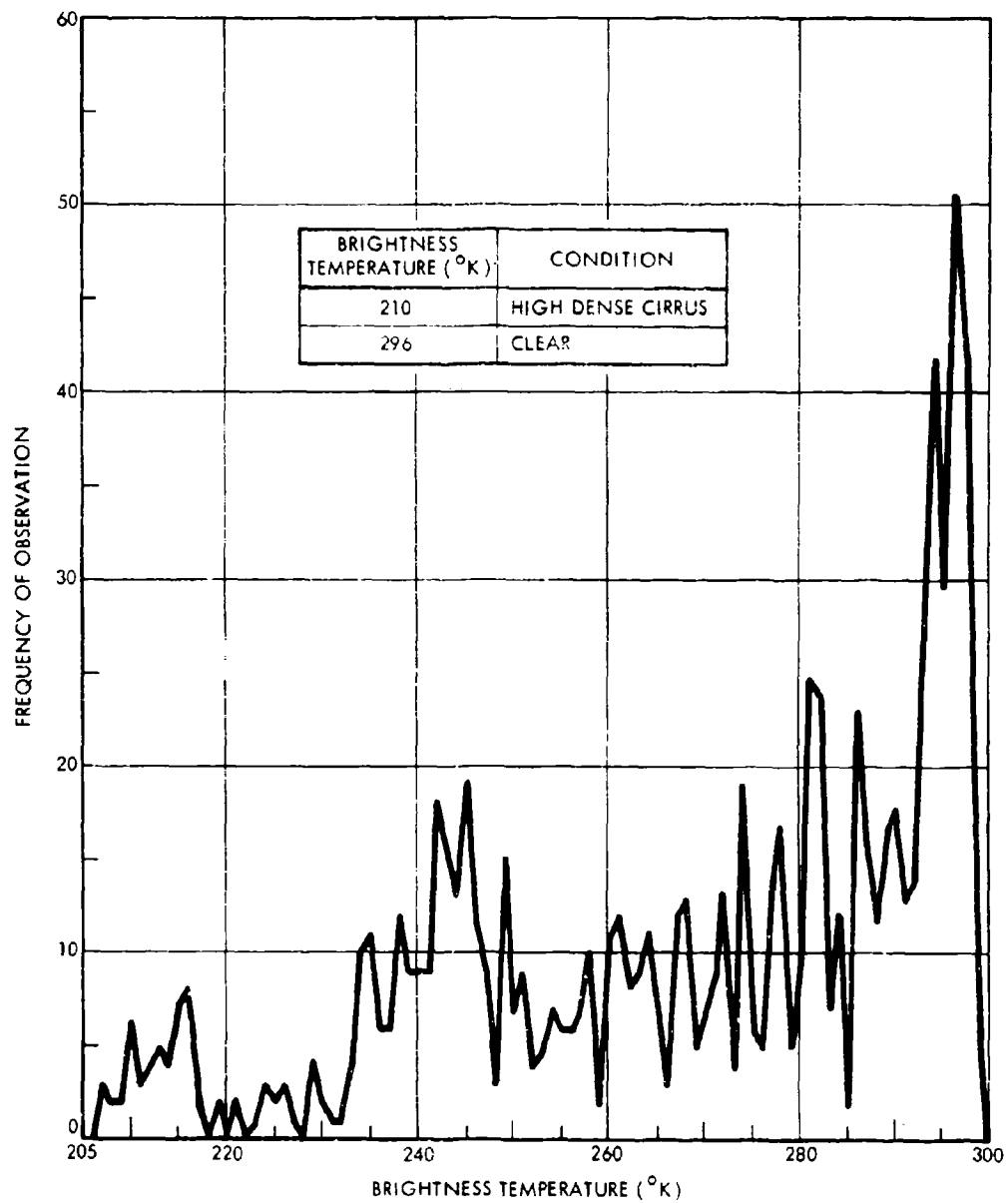
FIGURE A-3. Frequency Histogram of Nimbus II HR IR Observations Over an Area of About 150 nmi sq (Ref. 17)

133

temperature*) obtained over an area of 150 nmi^2 and in the
immediate vicinity of a tropical storm (Ref. 17). The range
in the brightness temperature includes the extremes of high
density cirrus (210°K) and clear (300°K) conditions. The
observational frequency peak at 296°K is associated with clear
conditions, which is recognizable by the following factors:
(i) the magnitude and repeatability of this radiance observa-
tion, and (ii) the standard deviation of the distribution on
the high radiance side of this distinct mode is close to the
r.m.s. error of measurement (about 1.5°K for the HRIR obser-
vations). The amount of dispersion on the high radiance side
of the frequency mode associated with the highest radiance
values can be used to discriminate between a mode associated
with totally clear observations and one associated with either
thin overcast or low dense overcast cloud conditions. This is
due to the fact that even for these cloud conditions, the dis-
persion will tend to be significantly greater than that ex-
pected from surface temperature variations (at least over
water) and random errors of measurements (Ref. 17).

The reduction of radiance data from a given column (or volume) of
the atmosphere to a temperature profile within that column of air in-
volves the solution of a Fredholm integral equation of the first kind
which may be written as (Ref. 15)

$$R(m) \approx \int_0^\infty K(m,\mathfrak{z}) \, f(\mathfrak{z}) \, d\mathfrak{z}$$

where R is the measured radiance, m the parameter of measurement
(either frequency or nadir angle, Fig. A-2), f($\mathfrak{z}$) the atmospheric
parameter to be deduced from the R measurement (e.g., temperature or
water vapor concentration), $\mathfrak{z}$ the altitude, and K a known kernel or
weighing function (e.g., like Fig. A-2). Since the inversion procedure

---

*The brightness temperature is defined by the product of the emissivity
and the absolute temperature.

involved requires a model of the temperature profile, available results indicate the following: (1) methods that utilize statistical functions to model temperature profiles in terms of infrared radiances from the earth's atmosphere will yield the most accurate results when using relatively few spectrally independent radiance measurements (e.g., as those proposed for HIRS); (2) an inversion method recently developed by Chahine (Ref. 18), enables the temperature profile to be derived with comparable accuracy from a relatively large number of spectrally independent radiances without the use of atmospheric statistical functions; (3) the r.m.s. errors in the temperature profile for clear and cloudy conditions are as indicated in Fig. A-4 (Ref. 12). These results are obtained from the conditions and statistical procedure used for Fig. A-1. This figure indicates that an accuracy of $\pm$ 3°C is achievable even at the high altitudes; (4) typical results of the inversion method are shown by the solid lines in Figs. A-5 and A-5a (Ref. 15), which are also compared with the dashed lines obtained from radiosonde soundings. The infrared temperature profiles (solid lines) are based on data obtained from a high altitude balloon, and measurements made in seven narrow spectral intervals (six in the 15μ band and one in 10μ window). Figure A-5 indicates mean deviations of 2^{O}K from the radiosonde soundings; but the errors are mainly near the tropopause, which is systematically placed too low because of instrument problems. Thus, an important result which holds for all inversion schemes is that the accuracy of the inverted temperature profile depends on the accuracy of the measurements rather than in the number of frequencies used in the measurements. Figure A-5a shows that infrared inversion provides no information below the top of a cloud deck, as indicated between the 300 and 200 mb pressure levels; and (5) the vertical resolution and accuracy of the temperature profiles cannot be improved significantly by increasing the spectral resolution (bandwidth), i.e., Fig. A-6 shows that the r.m.s. errors in the temperature profile deduced from radiance measurements in the 15μ CO$_2$ spectral region are somewhat insensitive for half-bandwidths less than 20 cm^{-1}. This result is apparently due to the high interlevel autocorrelation of temperature that exists for the earth's atmosphere; even though the radiances sensed in the narrower spectral regions

originate from slightly smaller vertical layers of the atmosphere, the
high correlation between the temperatures within adjacent layers pre-
vent improvements in the vertical resolution of the temperature pro-
files from increases in the spectral resolution (Ref. 17).

The above considerations have emphasized the infrared region be-
cause such has been the case during the first decade in the developments
of meteorological satellites. Although the use of microwave techniques
is also promising for the minimization of the effect of clouds on the
inferred temperature profiles, such techniques become of increasing
interest for the potential inference of the wind vector over the oceans
from measurements of the sea surface conditions.
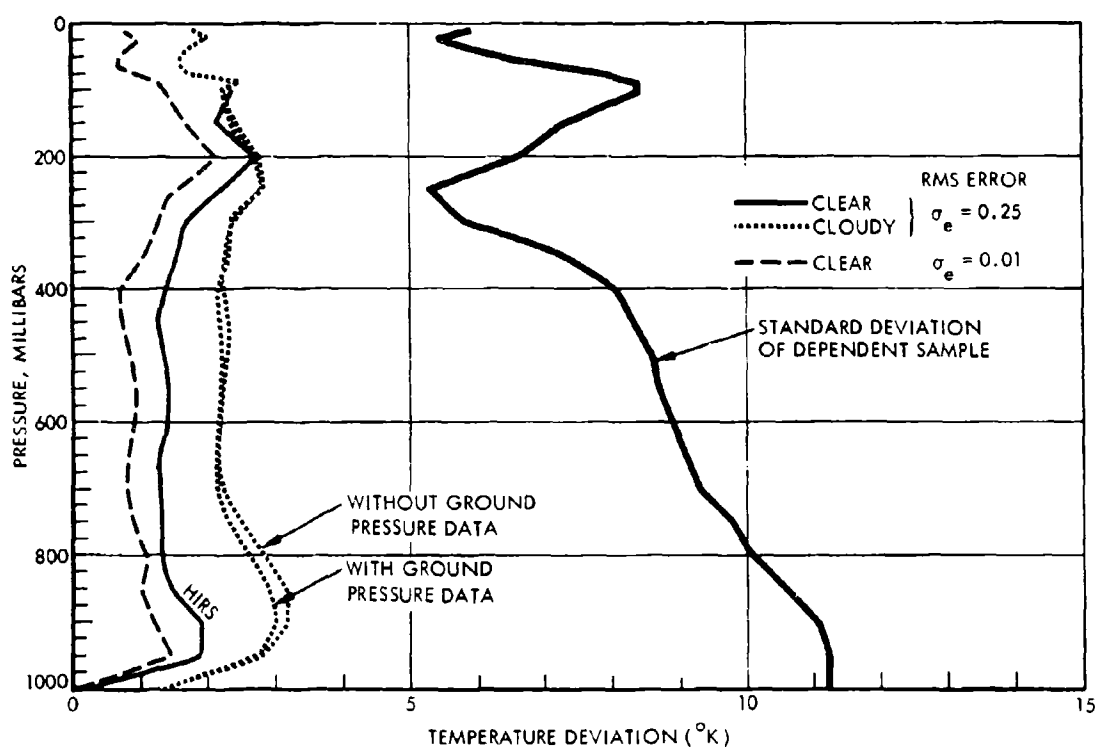
FIGURE A-4. Temperature Deviation of Atmospheric Pressure Levels (in milibars) Derived
from Statistical Properties of the Geopotential Height and Satellite-like
Radiance Measurements. The temperature deviation is given for clear and
cloudy conditions, and the RMS difference between radiosonde observed
and radiance calculated values (See Fig. A-1). The clear conditions cor-
respond to those of the proposed HIRS, i.e., with a field of view small
enough to make observations through broken clouds (Ref. 12).
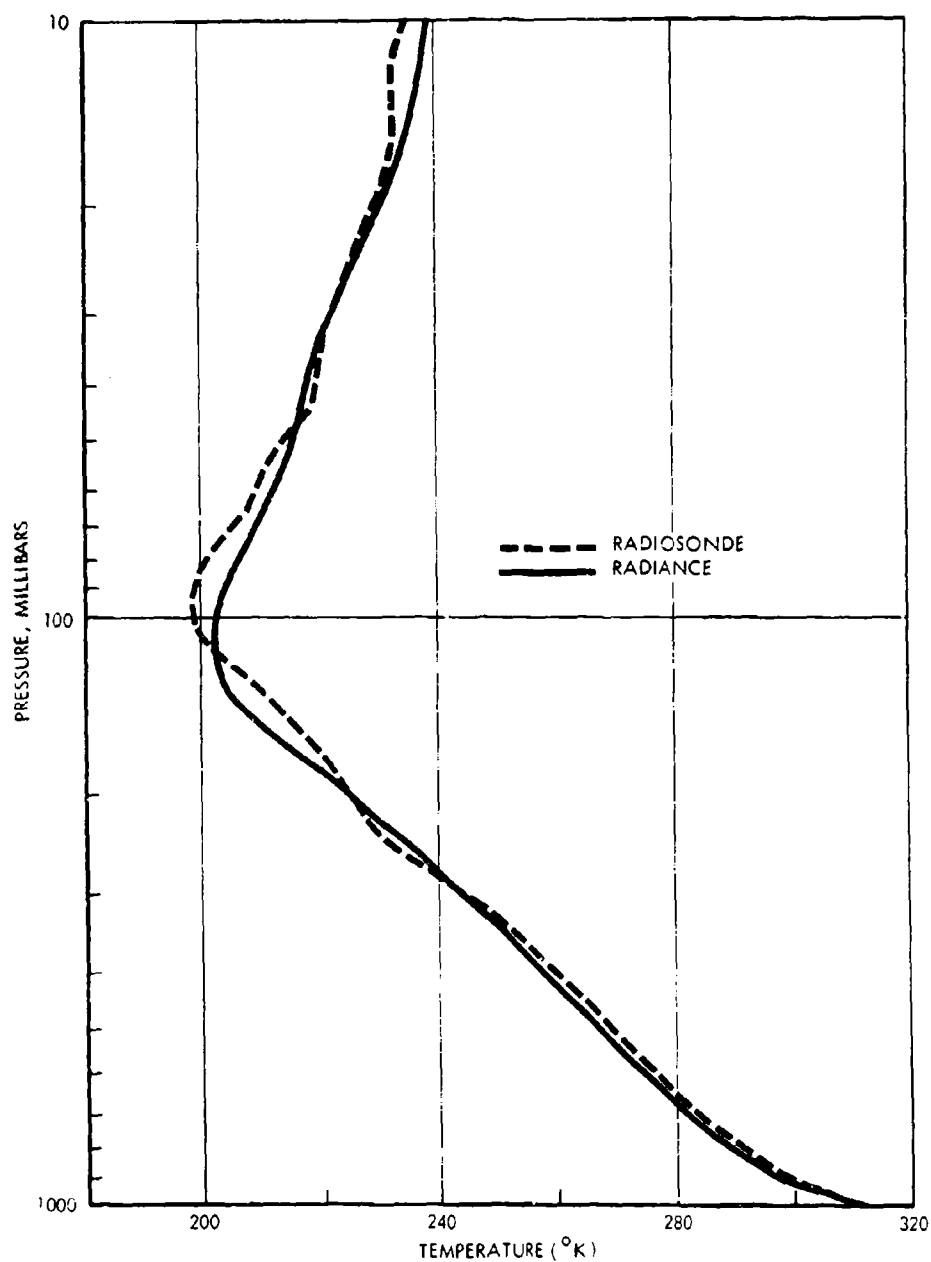
FIGURE A-5. Comparison of the Temperature Profile Deduced from Remote
Radiance Measurements (in six spectral intervals in the 15μ
band) under clear sky conditions from a high altitude balloon
over Texas at 7:57 a.m. (solid lines) and the temperature
profile corresponding to the noon Fort Worth radiosonde values
(dashed lines) (Ref. 15)
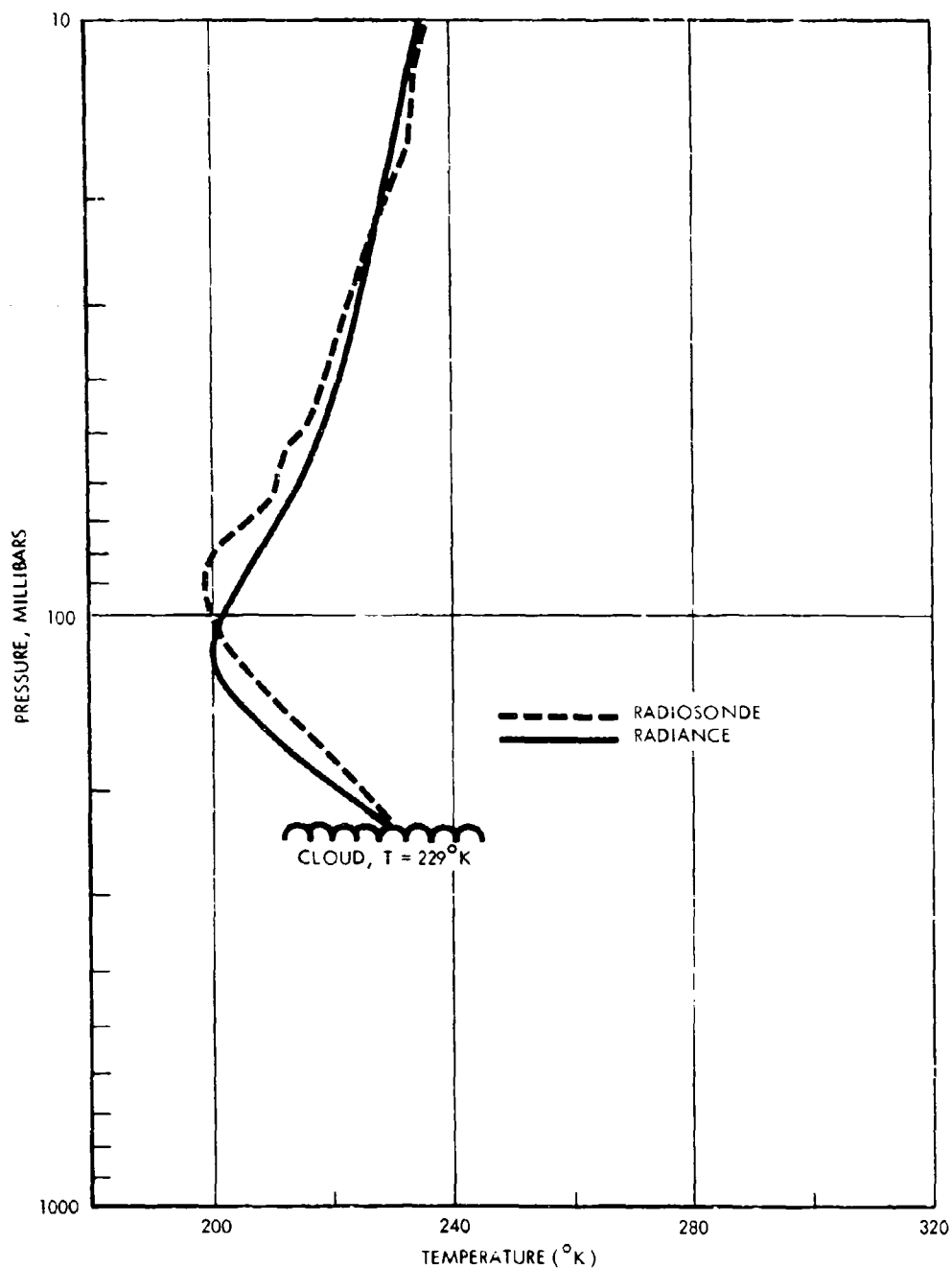
FIGURE A-5a . Comparison of the Temperature Profile Deduced from Remote Radiance Measurements (in six spectral intervals in the 15μ band) under cloudy conditions from a high altitude balloon over Texas at 12:17 and the temperature profile corresponding to the noon Forth Worth radiosonde values (dashed lines) (Ref. 15)
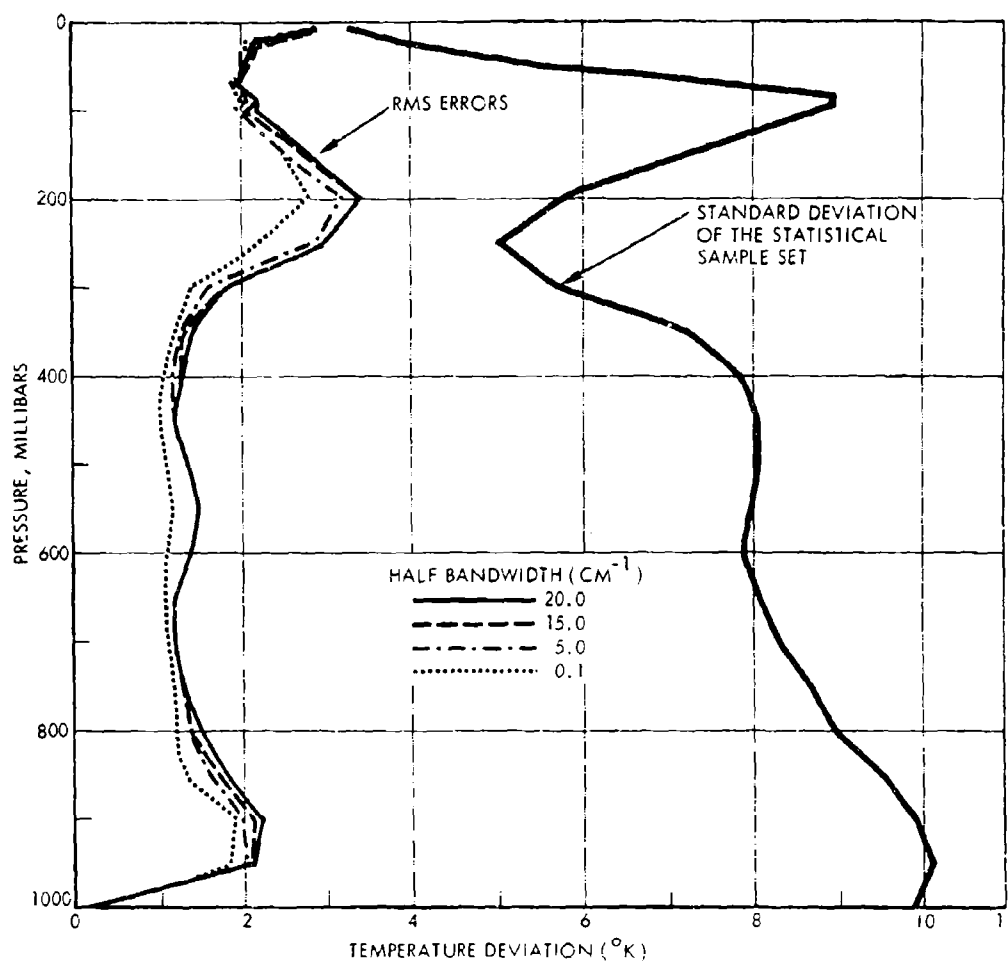
FIGURE A-6 . RMS Temperature Error Calculations for Different Bandwidths and Standard Deviation of Temperature of Statistical Sample. These Results are Derived from the Procedure Used in Figs. 1 and 4 (Ref. 17)

5. R.M.S. Errors in the Water Vapor Distribution

The meteorological parameters that can be inferred from measurements of the radiation reflected or emitted by the earth's atmosphere

(e.g., R, in the previous equation) are as follows: temperature pro-
files in the atmosphere including surface temperatures,* water vapor
distributions including surface values,* ozone distributions, and
aerosols as well as cloud characteristics. Although the required
transmission or kernel functions (K's) for carbon dioxide are known
with barely adequate precision, those for water vapor need further
attention, while the lack of adequate data for ozone is a major ob-
stacle at present (Ref. 15).
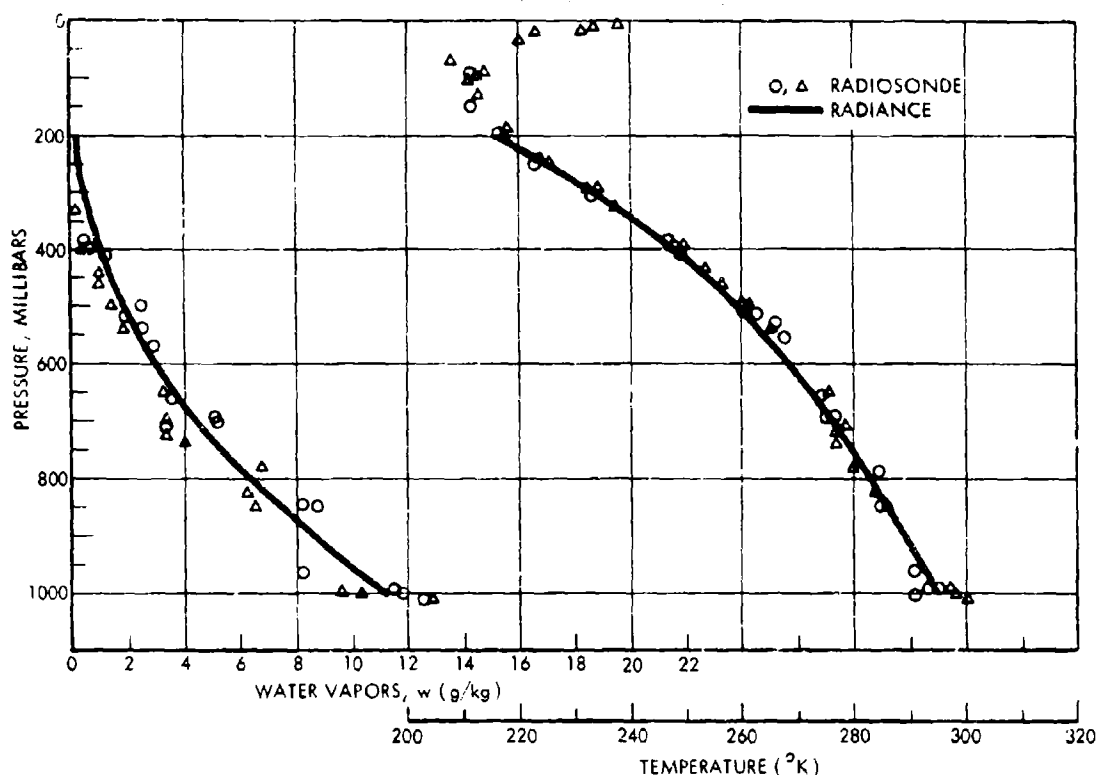
FIGURE A-7. Comparison of Water Vapor (mixing ratio) and Temperature Profiles
Deduced from Remote Radiance Measurements (using an inter-
ferometer spectrometer) under Clear Sky Conditions from a High-
Altitude Balloon over Texas at 9:06 a.m. (solid lines) and Corre-
sponding Profiles Derived from Nearby Radiosonde Ascents
(circles and triangles) (Ref. 15)

*For clear or broken cloud conditions.

140

Figure A-7 illustrates the water mixing ratio (in g/kg) and the temperature profiles inferred from the interferometer spectrometer data of Chaney (Ref. 28) taken from a high altitude balloon when no clouds were present. The circles and triangles are results from nearby radio-sonde ascents while the solid lines give the inferred values. This figure shows good agreement of the inferred water vapor profiles with the radiosonde soundings. Similar results have been found for conditions when there were broken clouds below the balloon (Ref. 29). Thus, it appears that the current state-of-the-art allows the use of infrared data to infer the total amount and at least one or two lapse rates of the water vapor profile in the atmosphere (Ref. 15).

6. R.M.S. Errors in the Wind Field

Since the influence of the wi· ` and pressure on the radiation field is very small, the velocity vector of the air motion (i.e., magnitude and direction) is not inferable from radiation measurements in the infrared. The development of techniques to measure the wind field from satellites is still in a very early stage of development. The early GARP program for the 1970s (circa 1973) plans to measure the wind field by using the following two independent but complementary techniques (Ref. 11):

a. About 900 constant-density level balloons, used as tracers for the horizontal air motion in a global scale, are tracked by radio from meteorological satellites operating at medium altitude orbits.* The proposed system would distribute 600 balloons on a nearly world-wide basis at the 150 to 200 mb pressure level, where the average speed is high (about 30 m/sec). This system would also make use of 300 balloons at the 850 mb level in the tropics, where the average wind speed in the lower troposphere is about 10 m/sec. The deployment of balloons at additional levels in the mid-troposphere is constrained by

*The balloons may also contain temperature and pressure sensors as well as radio altimeters to measure the altitude. Additional balloons may be required to correct for a nonuniform distribution of the balloons over the globe during the estimated 30 to 40 days lifetime of each balloon.

present balloon limitations, i.e., icing at night or within clouds and orographic obstacles. Thus, this constant density level balloon system will yield only 1 or 2 deg of freedom of the wind in the vertical, instead of the required four or five levels. The accuracy of the wind measurements will be well within the desired limit of ± 3 m/sec, since the balloon location can be determined accurately by using on the balloons either two-way transponders or stable transmitters. The two-way transponders (EOLE type) allows a very accurate (1 to 2 km) location of the balloon as well as individual interrogation and command capability, while the stable transmitter allows reasonable location accuracies of about 10 to 20 km. Thus, observations of the balloon displacement in one orbital period (i.e., about 90 min) of the meteorological satellite at medium altitude orbit would yield average winds with an error as low as 0.15 to 0.30 m/sec.

b. Using small scale cloud elements as tracers for the horizontal wind field, and tracking such cloud elements from meteorological satellites operating at geosynchronous altitudes (Ref. 30). An advantage of geosynchronous meteorological satellites is that they remain fixed relative to the motion of the weather in a global scale. Proposals for the early GARP program would utilize two kinds of high resolution instruments for the observation of the cloud elements: (1) an optical scanner similar to the spin-scan cameras used in the NASA ATS-1 and ATS-3 satellites; it would provide daytime cloud tracking with a horizontal resolution of 2 to 3 km with an accuracy for horizontal displacement of about 1 km; (2) a scanning infrared radiometer operating in the 8 to 12μ window region; it would provide the altitude of cloud tops with an accuracy of ± 0.5 km (assuming a temperature profile and uniform and opaque cloud), a horizontal resolution of 8 to 12 km with an accuracy for horizontal displacement of about 5 km. This IR radiometer would provide pictures with a spatial resolution range (at nadir) of about 8 x 8 to 16 x 16 km (depending on the optics)

of the disc of the earth, with a full picture available every
30 min. This system would yield daytime wind data from cloud
elements that are larger than 8 to 12 km, but which have a
detectable structure of smaller scale. Since the nighttime
wind data will not be as good, this system is limited to day-
time and cloudy conditions.

7. Chronological Development of U.S. Meteorological Satellites

A perspective of the current and future potential state-of-the-art
in the remote measurement of atmospheric parameters from satellites can
best be established from a brief review of the chronological develop-
ment of U.S. meteorological satellites and their sensor subsystems.

The RDT&E phase* of U.S. meteorological satellites has consisted
of three steps TIROS, NIMBUS, and ATS. Ten TIROS (Television Infra-
red Observational Satellites) were launched into medium altitude orbits
between April 1, 1960, and July 2, 1965, by NASA (Refs. 31, 32, 33).
This TIROS series was then followed by the TIROS Operational Satellites
(TOS), which began to carry out global cloud photography operationally
and routinely for the Environmental Sciences Services Administration
(ESSA). The six NIMBUS satellites were launched into medium altitude
orbits between 1964 and 1971. The NIMBUS series was set up to develop
sensors and technology for a "second generation" operational system.
The Advanced Technology Satellites (ATS) were launched into geo-
synchronous altitude orbit. A chronological description of the main
TIROS and NIMBUS series launched to date is shown in Table 1, while
Fig. A-8 includes also the ATS launchings. Each of these three RDT&E
series as well as the ESSA operational phase is described below.

_____

*The RDT&E phase of a new program involves the research, development,
test, and evaluation of a prototype system for the subsequent opera-
tional phase of the program.

TABLE A-1. TIROS AND NIMBUS RDT&E METEOROLOGICAL SATELLITES*

PRELAUNCH DESIGNATION	IN ORBIT DESIGNATION	LAUNCH DATE	ORBIT INCLINATION (deg)	ORBIT ALTITUDE (nmi)	SUBSYSTEMS	REMARKS
TIROS A-1	TIROS I	APR 1 '60	48	400	2 ½" vid (1W+1N lens)	First meteorological satellite
TIROS A-2	TIROS II	NOV 23 '60	48	400	2 ½" vid (1W+1N lens) 1 MRIR 1 wide-angle cone rad	First IR
TIROS A-3	TIROS III	JULY 12 '61	48	400	2 ½" vid (2W lens) 1 MRIR 1 wide angle cone rad 1 omnidir. rad	
TIROS D	TIROS IV	FEB 8 '62	48	400	2 ½" vid (1W+1M lens) 1 MRIR 1 wide angle cone rad 1 omnidir. rad.	
TIROS E	TIROS V	JUNE 19 '62	58	400	2 ½" vid (1W+1M lens)	
TIROS F	TIROS VI	SEP 18 '62	58	400	2 ½" vid (1W+1M lens)	
TIROS G	TIROS VII	JUNE 19 '63	58	400	2 ½" vid (2 W lens) 1 MRIR 1 Omnidir. rad	
TIROS H	TIROS VIII	DEC 21 '63	58	400	1 APT 1 ½" vid (W lens)	First APT
NIMBUS A	NIMBUS I	AUG 28 '64	Sun-sync.	600	1 Trimetrogen AVCS 1 APT 1 HRIR (S&LR)	First HRIR
TIROS I	TIROS IX	JAN 22 '65	Sun-sync.	400/ 1600	2 ½" vid (2 W lens)	1st worldwide coverage--1st cartwheel mode
TIROS (OT-1)	TIROS X	JULY 2 '65	Sun-sync.	400	2 ½" vid (2 W lens)	Axial mode
NIMBUS C	NIMBUS II	MAY 15 '66	Sun-sync.	600	1 Trimetrogen AVCS 1 MRIR 1 HRIR (S&LR)	

* The TIROS satellite is an 18-sided right cylinder, 22½" high, 42" in diameter, and weight about 300 lbs (Ref. 34). The NIMBUS satellite is described in Fig. 9 and weighs about 700 lbs.
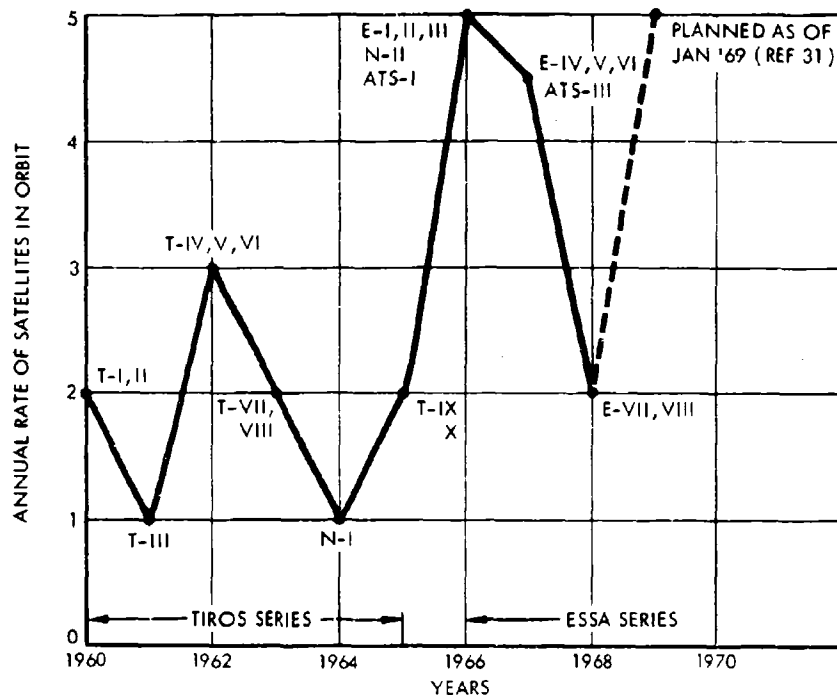
U.S. METEOROLOGICAL SATELLITES PLACED IN ORBIT

FIGURE A-8 . RDT&E and Operational U.S. Meteorological Satellites Placed
in Orbit during Nearly a Decade. Note that ten TIROS (T) and
one NIMBUS (N) RDT&E Satellites were utilized during the first
half of the decade, while eight ESSA (E) account for most of
the successful launchings so far in the second half of the decade

The TIROS series was devoted to the identification and tracking
on a world-wide and synoptic basis of weather phenomena such as cloud
cover mapping, storm tracking (e.g., frontal systems, hurricanes, etc.),
radiation balance, cloud top heights, surface temperatures, tropo-
spheric water vapor, and stratospheric temperature and circulations.
Observations consisted initially of photographing cloud patterns with
television cameras in daytime, which were supplemented later by infra-
red radiometers to make cloud observations at night. The first satel-
lite in this series (TIROS I) was placed in a circular orbit at an
altitude of 400 nmi and inclination of 48 deg to the equator. The
sensor subsystem consisted of two television (1/2 in. vidicon) cameras;
one with a wide angle lens of 104 deg, and the other with a narrow

angle lens of 12.7 deg. The second meteorological satellite (TIROS II) launched in the same year added to the camera system the first infrared sensors,* which consisted of a Medium Resolution Infrared Radiometer (MRIR) and one wide-angle cone radiometer. The MRIR provided a 5 deg field of view, a ground resolution of 30 nmi from 400 nmi orbit altitude, and scanning channels in the following spectral bands: 0.55 to 0.75μ, 0.2 to 6μ, 6 to 6.5μ, and 8 to 12μ. The wide-angle cone had a 50 deg field of view, a ground resolution of 350 nmi, and was used to measure the equivalent local blackbody temperature and albedo of the earth. The third meteorological satellite (TIROS III) was launched in the subsequent year (July 1961), and its sensor subsystems added an omnidirectional radiometer to measure long and shortwave radiation over the entire earth's disc. It also modified the camera system to use both cameras with wide angle lens. TIROS IV, V, and VI were launched during 1962 and used the same type of sensor subsystems as in the previous satellites, except that the two-camera system was modified to use one wide-angle lens (104 deg) and one medium-angle lens (78 deg). Likewise, TIROS VII and VIII were launched in 1963 with the same type of sensor subsystems, except that the two-camera subsystem of TIROS VIII utilized one camera with wide lens, and one Automatic Picture Transmission (APT) 1 in. vidicon camera. The TIROS series concluded with the launchings of TIROS IX and X during 1965.

The NIMBUS series of six RDT&E meteorological satellites started with the launching of NIMBUS I (August 28, 1964) and NIMBUS II (May 15, 1966) into a sun-synchronous orbit at an altitude of 600 nmi.** The remainder of the series consists of NIMBUS III (launched on April 14,

---

*The satellite Explorer VII had carried earlier a rather simple array of hemispheric, omnidirectional sensors to measure the radiation balance of the earth.

**A sun synchronous orbit at this altitude allows at least two observations every 24 hr of practically all points on the globe and at the same local time. The orbit plane is inclined to the equator 98.7 deg and precesses around the center of the earth at a rate that is synchronous with the revolution of the earth around the sun.

1969 and described in Fig. A-9),* NIMBUS IV (to be launched in 1970),
NIMBUS V and NIMBUS VI (both being planned for 1971). The basic NIMBUS
satellite is a system defined by the following characteristics: (1) a
structure designed to accommodate a maximum number of experiments, (2)
about 200 watts of electrical power for experiments, (3) pointing of the
instruments at the earth at all times with an accuracy of about 1 deg,
(4) a stable and moderate thermal environment required by many instruments,
and (5) a data subsystem that can acquire and store in the order of 10^9 to
10^{12} bits per orbit, and transmit these data to the ground while passing
over Alaska. The missions of NIMBUS I and NIMBUS II included the
following objectives: (a) demonstrate improvements in making high
resolution daytime cloud observations, (b) demonstrate the feasibility
of high resolution nighttime cloud mapping, (c) transmit both day and
nighttime cloud images to local receivers, and (c) map emitted telluric
radiation as well as reflected solar radiation in various spectral
bands. The three subsystems of NIMBUS I consisted of the following: a
set of three television cameras and a tape recorder called the Advanced
Vidicon Camera System (AVCS) for daytime cloud photography, an addi-
tional television camera to transmit daytime cloud pictures via the APT
to simple receivers, and the first scanning High Resolution Infrared
Radiometer (HRIR) with Stored and Local Readout (S&LR) capability. The
HRIR provided a 0.46 deg field of view, and a ground resolution of 5 nmi
in the spectral band from 3.5 to 4.1μ. The subsystems on NIMBUS II con-
sisted of the AVCS, the HRIR (S&LR), and a Medium Resolution Infrared
Radiometer (MRIR) with fixed channels to map and image thermal radiation
emitted by (a) atmospheric water vapor or cirrus clouds (6.4 to 6.9μ),
(b) carbon dioxide (14 to 16μ), (c) cloud tops or the earth's atmosphere
(5 to 30μ), and (e) reflected solar radiation (0.2 to 4.0μ). The HRIR
demonstrated that cloud formations can be observed globally at night
with a spatial resolution of about 4 nmi, and that their heights are
inferable from the measured cloud top temperatures. Thus, the HRIR
produced at night three dimensional cloud maps in a global scale, which

---

*The NIMBUS III satellite was placed in an orbit defined by a perigee
of 582 nmi, apogee of 613 nmi, and inclination of 99.9 deg.

are unattainable with television cameras. The 10.5 to 11.5μ channel
of the MRIR produced cloud cover and neight maps for day and nighttime
conditions with a considerable lower spatial resolution (~25 nmi).
Based on these results, the ESSA's TOS will incorporate the use of a
high resolution 11μ scanning radiometer for day and night cloud mapping.
Other significant results from NIMBUS I and NIMBUS II are as follows:
(a) determination of temperatures of the earth's surface with suffi-
cient accuracy to allow for the tracking of ocean currents (as mapped
by the HRIR in cloud free areas); (b) improved insight of the global
distribution of the net radiative energy flux through the upper
boundary of the atmosphere (Ref. 35); and (c) better understanding of
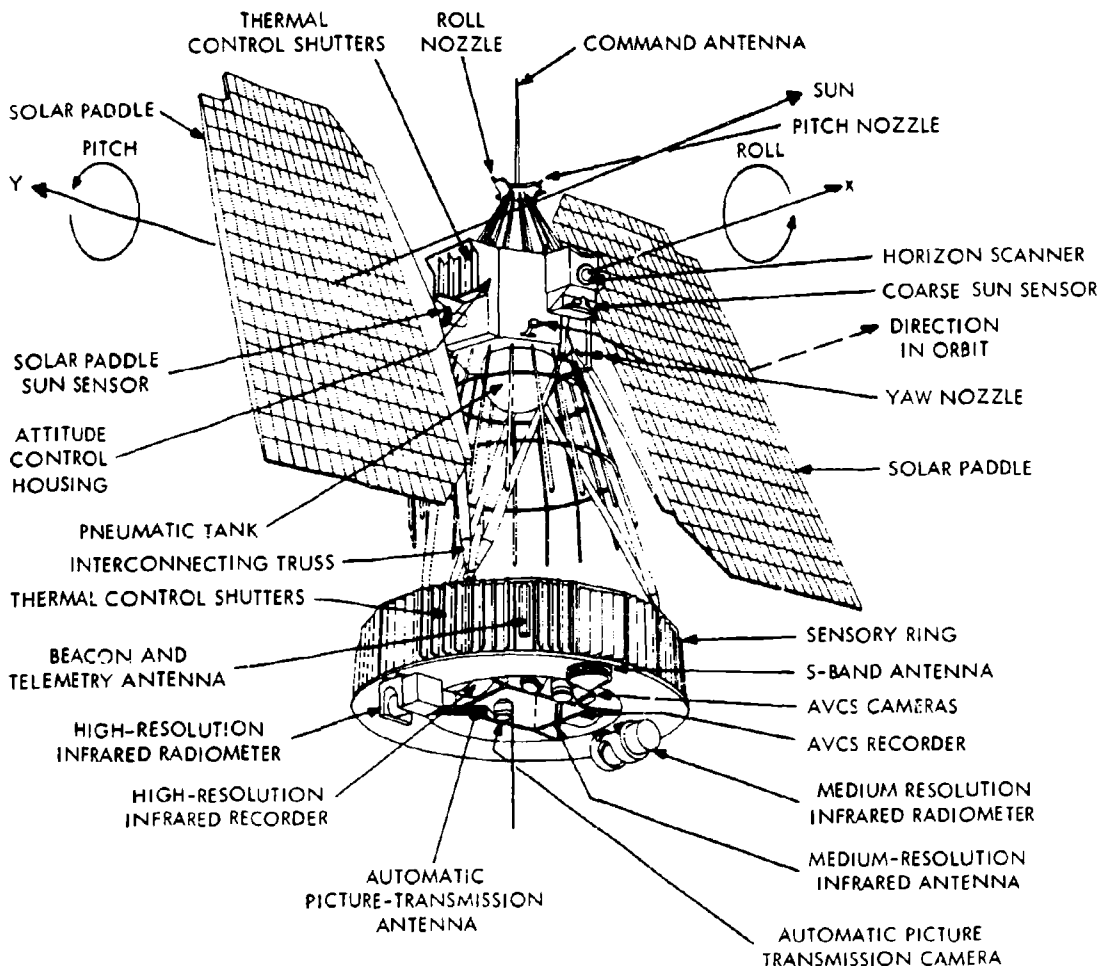the morphology of the circulation in the lower stratosphere (Ref. 36).

FIGURE A-9 . The NIMBUS III Spacecraft

Besides the two main series of RDT&E meteorological satellites (TIROS and NIMBUS) in medium altitude orbit, a third RDT&E phase involves three NASA Application Technology Satellites (ATS) for operation in geosynchronous orbit.[*] Meteorological satellites in synchronous altitude will allow nearly continuous observations of the same areas of the earth, since the meteorological application of the ATS observations in the form of time lapse movies have already shown the weather in motion over a given geographical area.[**] While the infrared signals become very low at geosynchronous altitude, the ATS system allows the observation of the development of local, short-time scale meteorological phenomena (e.g., growth of severe storms, the tracking of small cloud elements for wind measure events, etc.). The first ATS system (ATS-I) was launched into geosynchronous orbit on December 7, 1966, the second one (ATS-III) on November 5, 1967, and a third one (ATS-E) is planned for launch in August 1969 (Ref. 31).[+] The characteristics and performance of the meteorological sensor subsystem on ATS-I and III are summarized in Table 2 (Ref. 37). The sensor subsystem of ATS-I consisted of a spin scan cloud camera in black and white for the Spin Scan Cloud Cover Experiment (SSCEE). This instrument is really a scanning telescopic photometer with a field of view of 0.1 milliradian, which utilizes the spin of the satellite to scan the scene from west to east, and which tilts the telescope slowly through a small angle to scan the scene from north to south. The transmission of the pictures was accomplished by satellite facsimile or Weather Facsimile (WEFAX). The ATS-III utilized a spin scan cloud camera using three in-line pinholes to generate three color components: red, blue, and green. Fiber optics are used to carry the color information to three separate photomultipliers. The first tube is equipped with a green filter, the

---

[*]The ATS systems are nonmeteorological satellites that have allowed limited experiments to detect mainly cloud motions.

[**]The time lapse technique speeds up the motion of the weather, i.e., one can see what took place in 18 hr of a day (time for the sun to go from horizon to horizon) in about 3 or 4 sec (Ref. 30).

[+]Two other ATS launch attempts took place on April 6, 1967 (ATS-II), and August 10, 1968 (ATS-IV).

second with a red filter, and the third with a blue filter. The signals thus generated are transmitted to the ground. The information is sent in groups of four signals. The first signal carries information concerning the intensity of green, the next signal represents red, and the third one blue. The last signal in the sequence is a fixed reference signal to help balance the colors when all the signals are integrated into a complete picture at the receiving stations. The ATS-III also included one Image Dissector Camera System (IDCS) and used WEFAX and Omega Position Location Equipment (OPLE) for the transmission and collection of data from remote sensors. The use of WEFAX through the ATS-I and ATS-III satellites has demonstrated the practicality of transmitting data collected and analyzed at a central location to users in remote locations.

TABLE A-2. SPIN-SCAN SYSTEM CHARACTERISTICS AND PERFORMANCE

Spacecraft	ATS-I	ATS-III
Size, in.	7 x 11 x 10	7 x 11 x 12
Weight, lb	<16	23.5
Primary Power	-24 vdc, 0.6 A	-24 vdc, 0.9 A
Resolution	0.1 m rad (2 mi)	0.1 m rad (2 mi)
Dynamic Range	>400:1	>400:1
Scan Lines	2000	2400
Earth Coverage	~50 deg N to 50 deg S	Full earth
Scan Rate	100 lines/min	100 lines/min
Picture Time	20 min	24 min
Retrace Time	2 min	2 min
IFOV[a] Dwell Time	9.6μ sec	9.6μ sec
Video Bandwidth	100 KHz	100 KHz/channel
Total Bandwidth	100 KHz	4 MHz
Spectral Response	0.48-0.63μ	Blue 0.38-0.48μ Green 0.48-0.58μ Red 0.55-0.63μ

[a]Instantaneous Field of View.

The operation phase to date of meteorological satellites consists of eight ESSA satellites launched into medium altitude orbit between February 3, 1966, and December 15, 1968. The ESSA satellites have utilized sensor subsystems developed in the earlier NASA TIROS series; except for the use of a Flat Plate Radiometer (FPR), which is a variation of the omnidirectional radiometer for measurements of longwave emission of radiation. The ESSA meteorological satellites have been launched at the approximate average rate of three satellites each year (Table A-3).

8. Current Projections for the Development of Meteorological Satellite Subsystems

The subsystems on the meteorological satellites flown to date were designed to map cloud cover by using visual and radiometric sensors, and to map telluric and reflected solar radiation in the various spectral bands. Most of the sensors being developed for future use represent improvements of present sensors to provide better spatial and spectral resolution. Some sensors will provide observations in several spectral bands so as to allow inference of temperature distributions and water vapor profiles through the troposphere. A precise perspective of the current projections for the development of meteorological satellite subsystems is best derived from a brief review of the experiments planned for the research satellites NIMBUS III (or NIMBUS B-2, launched on April 14, 1969) and NIMBUS IV (or NIMBUS D, to be launched in March 1970).*

The experiments on NIMBUS I and II were devoted exclusively to improving the synoptic mapping of meteorological phenomena or to making atmospheric measurements of general scientific interest from medium altitude orbit (600 nmi). The experiments on NIMBUS III and IV put emphasis on the development of subsystems for the determination from medium altitude orbit (600 nmi) of initial and boundary conditions for the numerical integration of the equations of motion, i.e., the

---

*The subsystems for the remaining two NIMBUS satellites (i.e., NIMBUS E and F) are as yet unspecified.

TABLE A-3. ESSA OPERATIONAL METEOROLOGICAL SATELLITES

PRELAUNCH DESIGNATION	IN ORBIT DESIGNATION	LAUNCH DATE	ORBIT INCLINATION (deg)	ORBIT ALTITUDE (nmi)	SENSORS SUBSYSTEMS	REMARKS
TIROS (OT-3)	ESSA I	FEB 3 '66	SUN-SYNC	400	2 ½" vid (W-lens)	First operational system
TIROS (OT-2)	ESSA II	FEB 28 '66	SUN-SYNC	750	2 APT	
TOS A	ESSA III	OCT 2 '66	SUN-SYNC	750	2 AVCS 1 FPR	
TOS B	ESSA IV	JAN 26 '67	SUN-SYNC	750	2 APT	
TOS C	ESSA V	APR 20 '67	SUN-SYNC	750	2 AVCS 1 FPR	
TOS D	ESSA VI	NOV 10 '67	SUN-SYNC	750	2 APT	
TOS E	ESSA VII	APR 16 '68	SUN-SYNC	750	2 AVCS 1 FPR	
TOS F	ESSA VIII	DEC 15 '68	SUN-SYNC	750	2 APT	

measurement of temperature and water vapor profiles through the troposphere, the measurement of wind fields by tracking free floating balloons distributed globally at various height levels, and the real-time recovery of surface data from buoys.*

The NIMBUS III carried out seven experiments,** three of which put emphasis on the requirements for the numerical integrations of the equations of motion, one is for scientific investigations, and three continue the mapping observations of NIMBUS I and II. The first group of three experiments consists of two spectrometer experiments to yield data for the determination of temperature and water vapor profiles in the troposphere and one experiment capable of tracking balloons and relaying measurements from automatic stations. These experiments are as follows:

a. One spectrometer is a Michelson Interferometer called Infra-Red Interferometer Spectrometer (IRIS), which operates between 6 and 20μ at a relative spectral distribution of 1:200. Included within this spectral interval are the water vapor absorption band centered at 6.3μ, the 9.6μ ozone band, and the 15μ carbon dioxide band.

b. The second spectrometer is a modified Fastie-Ebert grating spectrometer called Satellite Infra-Red Spectrometer (SIRS). Radiant energy is detected in seven spectral intervals of the 15μ carbon dioxide band. The spectral intervals are 5 cm^{-1} wide. An eighth channel senses radiation in the atmospheric window centered at 11.1μ.

c. The data relay and balloon tracking experiment consists of a satellite borne transmitter, receiver, and computer. This experiment is called Interrogation, Recording, and Location System (IRLS). By using communication with a given automatic

---

*An operational system of meteorological satellites operating at medium altitude orbit will require several satellites to yield global coverage in real-time.

**These experiments were described in August 1968 (Ref. 33) and, therefore, exclude possible subsequent changes prior to the actual flight.

ground station, the IRLS can determine the location of a
station within about 1 nmi, and can also interrogate a set of
sensors (such as a thermistor) contained in the station. This
IRLS experiment is an engineering test of a system involving
observations of six balloons over the United States and utiliz-
ing 20 ground stations.

The scientific experiment consists of a Monitor of Ultraviolet
Solar Energy (MUSE), which will expand the capability of NIMBUS to
perform scientific investigations relevent to meteorology. MUSE will
measure solar radiation in five spectral intervals (each 100 A wide)
ranging from 1200 A to 2600 A. The three experiments that will continue
the mapping observations of NIMBUS I and II are as follows: The HRIR
(S&LR) with day and night capability, the MRIR, and the Image Dissector
Camera System (IDCS).

The NIMBUS IV plans to carry out nine experiments, five of which
emphasize the requirements for mathematical prediction models, two will
make basic scientific investigations, and the remaining two are for the
mapping of horizontal fields. The first group of five experiments con-
sists of four experiments to yield temperature (all four of them) and
water vapor (three of them) profiles in the troposphere, and one
experiment for the tracking of balloons. These experiments are as
follows:

a. The IRIS experiment (as in NIMBUS III) with its spectral range
    extended to the range between 8 and 40μ.

b. The SIRS experiment (as in NIMBUS III) with the addition of
    six spectral intervals, mostly in the rotational water vapor
    bands between 18 and 30μ.

c. A Filter Wedge Spectrometer (FWS) operating between 1.2 and
    6.4μ.

d. A Selective Chopper Radiometer (SCR) operating in the 15μ
    carbon dioxide band, which is expected to achieve a very high
    spectral resolution by filtering the radiation through carbon
    dioxide absorption cells.

e. The IRLS experiment (as in NIMBUS III) will be expanded to be
    capable of interrogating hundreds of stations instead of 20 on
    NIMBUS III. Also a balloon experiment will be performed to
    measure the wind field over a large area (such as the tropics)
    within at least one height level.

The two scientific investigations will use the MUSE experiment (as
in NIMBUS III) and a Backscatter Ultraviolet (BUV) spectrometer to
measure the intensity of solar radiation reflected by the atmosphere in
14 intervals (each 10 A wide) over the spectral range from 2500 to
3400 A. The BUV experiment will yield the global vertical distribution
of ozone between 7 and 25 nmi, approximately. The two experiments for
the mapping of the horizontal fields consists of the IDCS experiment
(as in NIMBUS III) to provide television pictures, and a scanning
Temperature and Humidity Infrared Radiometer (THIR) operating in the
6.3μ water vapor and the 11μ window bands with a spatial resolution of
the HRIR. The THIR experiment will yield measurements of the horizontal
water vapor and cloud fields.

Besides the main projected RDT&E activities of the NIMBUS II and
NIMBUS III satellites, it is also of interest to review the development
of three radiometers for the new ESSA Improved TIROS Operational System
(ITOS) as well as a proposed very high resolution radiometer for
synchronous satellites.* The three radiometers for the ITOS are as
follows:

a. ITOS high resolution radiometer with two channels in the 10.5
    to 12.5μ and 0.52 to 0.73μ intervals. The field of view of
    these channels are 0.30 deg and 0.16 deg, respectively, and
    yield corresponding ground resolutions from the nominal orbit

---

*The projected activities for 1969 of the operational ESSA series in-
volve two additional launchings of the current TOS (TIROS Operational
System), and a subsequent shift to the new ITOS. Four projected ITOS
launchings (TIROS M, ITOS A, B, and C) will utilize the following
eight subsystems: two AVCS, two APT, two HRIR (S&LR), one FPR, and
one SPM (Solar Proton Monitor). The SPM will measure the flux of
protons in the 10.30 and 60 M-ev range, and electrons in the 100 ard
750 E-ev range.

altitude of the ITOS (775 nmi) of 3.7 and 2 nmi. Because of this high spatial resolution, the quality of the photo-images should approach that of television cameras. Some other advantages of this radiometer are: (1) its capability to measure surface temperatures in the 10.5 to 12.5μ interval equally well during day and nighttime conditions, (b) the identification of cloud free areas in the daytime by means of the coordinated visible channel measurements, and (c) its adaptation to the APT system to yield a Direct Readout of InfraRed (DRIR) system. The DRIR system will operate during the entire orbit, reading out infrared imagery to APT stations all over the world in the daytime (when the infrared data will be interleaved with the standard APT pictures) as well as in the nighttime.

b. ITOS Vertical Temperature Profile Radiometer (VTPR) with eight channels, six of which will be in the 15μ carbon dioxide band, one in the rotation water vapor band, and one in the 11μ window. The spectral resolution for all channels will be about 5 cm^{-1}. The VTPR is intended solely for the probing of the temperature profile from operational meteorological satellites, and it takes advantage of the latest advances in technology, i.e., the weight (10 lb) and power (2 watts) are significantly smaller than those of earlier instruments designed for vertical temperature probing (e.g., SIRS: 92 lb and 20 watts; IRIS: 29 lb and 12 watts).

c. ITOS Very High Resolution Radiometer (VHRR) with two channels in the 10.5 to 12.5μ and 0.6 to 0.7μ intervals. The field of view of each channel is 0.034 deg, which yields a ground resolution of 0.4 nmi from the nominal altitude orbit. Thus, the ground resolution of the VHRR represents an order of magnitude improvement over that of the NIMBUS HRIR and ITOS High Resolution Radiometer, and nearly two orders of magnitude improvement over that of the TIROS and NIMBUS medium resolution radiometers. As such, the resolution of the VHRR is comparable to that of television systems currently flown on meteorological

156

satellites. This level of resolution is achieved by using a
mercury-cadmium-telluride detector cooled radiatively to 80°K.
This high resolution will allow the study of smaller scale
phenomena such as the three-dimensional structure of cloud
patterns and frontal systems. Since the bit rate of the in-
strument exceeds the capacity of any available tape recorder
system, it may be necessary to readout the data directly via
a relay geosynchronous satellite (e.g., see Ref. 38).

The proposed Very High Resolution Radiometer for Geosynchronous
Altitude (not yet approved) with one channel in the 10.5 to 12.5µ
interval has a detector similar to the VHRR. The field of view of this
instrument is 0.023 deg, which yields a ground resolution of 8 nmi from
geosynchronous altitude. The advantages or a very high resolution
radiometer over a camera that senses visible radiation are as follows:
(1) the radiometer system will take "full earth" pictures continuously
and independently of the position of the terminator. The familiar
"full earth" pictures made with the ATS cameras can only be taken during
a small fraction of the day, since pictures taken during a 24 hr period
show varying smaller portions of the earth (depending on the location of
the terminator); and (2) unlike the camera system, the radiometer has a
potential for temperature measurements; which can in turn be used to
infer cloud top heights, sea surface temperature variations (in cloud-
free regions), and the altitude of winds deduced from time lapse move-
ments of cloud patterns.

Table A-4 shows a summary of the main characteristics of all the
radiometric instruments that have been developed during the last decade
for the remote probing of the troposphere and stratosphere from meteoro-
logical satellites.* The first 13 instruments in this table have been
either flown or approved for the RDT&E (i.e., TIROS and NIMBUS NASA
series) and operational (TOS and ITOS, ESSA series) programs, while the
last two have been proposed for future RDT&E meteorological satellites

---

*The mechanical details of the first 14 instruments are described in
Ref. 32 (and the references thereto), while the proposed HIRS design
is treated in some detail in Ref. 17.

TABLE A-4. SUMMARY OF RADIOMETRIC INSTRUMENTS FOR REMOTE PROBING OF THE TROPOSPHERE
AND STRATOSPHERE FROM SATELLITES IN MEDIUM ALTITUDE ORBIT

NUMBER	RADIOMETRIC INSTRUMENT	CHANNELS	DETECTOR(S)	INSTRUMENT FIELD OF VIEW	LINEAR RESOLUTION (at Nadir & Nominal Altitude)	SATELLITE	APPLICATION
1.	Wide Field Sensors	1) Black-long and short wave radiation 2) White-long wave radiation.	Hemispheres or Flat Plates Thermistor Bolometers	Entire Earths' Disc.	50%	Explorer VII TIROS III,IV VII ESSA III,V, Etc.(incl. new ITOS series)	Radiation Balance (Long wave emission albedo)
2.	Two Cone Low Resolution Radiometer	As (1) above	Thermistor Bolometers	50 deg	350 nmi	TIROS II, III, IV	Radiation Balance
3.	Medium Resolution Radiometer (Scanning)	1) 6.0-6.5μ (TIROS II, III, IV) 14.8-15.5μ (TIROS VII) 2) 8.0-12.0μ 3) 0.2-6.0μ 4) 8.0-30.0μ (not TIROS IV) 5) 0.55-0.75μ	Thermistor Bolometers	5 deg	30 nmi	TIROS II, III, IV, VII	Cloud Cover Mapping Storm Tracking Surf. Temp. Cloud Top Height Radiation Balance Water Vapor

TABLE A-4. SUMMARY OF RADIOMETRIC INSTRUMENTS FOR REMOTE PROBING OF THE TROPOSPHERE
(CONT'D)   AND STRATOSPHERE, FROM SATELLITES IN MEDIUM ORBIT

NUMBER	RADIOMETRIC INSTRUMENT	CHANNELS	DETECTOR(S)	INSTRUMENT FIELD OF VIEW	LINEAR RESOLUTION (at Nadir & Nominal Altitude)	SATELLITE	APPLICATION
4	High Resolution InfraRed Radiometer HRIR (scanning)	1) 3.5-4.1μ NIMBUS I,II 2) 3.5-4.1μ 0.7-1.3μ NIMBUS III	Pb St Single-stage Radiactively Cooled to 200° K	0.46 deg	5 nmi	NIMBUS I, II, III	Cloud Cover Mapping Storm Tracking Surf. Temp. Cloud Top Height (nighttime)
5	Medium Resolution InfraRed Radiometer MRIR (scanning)	1) 6.4-6,9μ 2) 10.0-11.0μ 3) 14.0-16.0μ NIMBUS II 14.5-15.5μ NIMBUS III 4) 5.0-30.0μ NIMBUS II 20.0-23.0μ NIMBUS III 5) 0.2-4.0μ	Thermistor Bolometers	2.9 deg	30 nmi	NIMBUS II, III	As Above
6.	InfraRed Interfero- meter Spectrometer (IRIS)	1) 5-20μ Spectral Scanning Resolution 5 cm^{-1}	Thermistor Bolometers	8 deg	80 nmi	NIMBUS III	Vertical Profiles (Temp,H_2O)
6a.	InfraRed Interfero- meter Spectrometer (IRIS)	1) 6.3-50μ Spectral Scanning Resolution 3 cm^{-1}	Thermistor Bolometers	5 deg	50 nmi	NIMBUS IV	Vertical Profiles (Temp,H_2O)

TABLE A-4. SUMMARY OF RADIOMETRIC INSTRUMENTS FOR REMOTE PROBING OF THE TROPOSPHERE
(CONT'D)   AND STRATOSPHERE FROM SATELLITES IN MEDIUM ALTITUDE ORBIT

NUMBER	RADIOMETRIC INSTRUMENT	CHANNELS	DETECTOR(S)	INSTRUMENT FIELD OF VIEW	LINEAR RESOLUTION (at Nadir & Nominal Altitude)	SATELLITE	APPLICATION
7	Satellite InfraRed Spectrometer (SIRS)	8 Channels: 7 in 15μ CO_2 Band 1 in 11μ Window Resolution 5 cm^{-1}	Thermistor Bolometers	12 deg	120 nmi	NIMBUS III	Vertical Temp. Profile
7a.	Satellite InfraRed Spectrometer (SIRS)	14 Channels: 7 in 15μ CO_2 Band 6 in rot. H_2O Band 1 in 11μ Window Resolution 5 cm^{-1}	Thermistor Bolometers	12 deg	120 nmi	NIMBUS IV	Vertical Profiles (Temp,H_2O)
8.	Filter Wedge Spectrometer (FWS)	1) 1.2-2.4μ 3.2-6.4μ	Pb St Single Stage Radiatively Cooled to 160° K	2 deg	20 nmi	NIMBUS IV	Vertical Profiles (Temp.,H_2O) Water or ice content in clouds.
9.	Selective Chopper Radiometer (SCR)	6 Channels: all in 15μ CO_2 band One switchable to 11μ window	Thermistor Bolometers	10 deg	100 nmi	NIMBUS IV	Vertical Temp. Profile

TABLE A-4. SUMMARY OF RADIOMETRIC INSTRUMENTS FOR REMOTE PROBING OF THE TROPOSPHERE
(CONT'D) AND STRATOSPHERE FROM SATELLITES IN MEDIUM ALTITUDE ORBIT

NUMBER	RADIOMETRIC INSTRUMENT	CHANNELS	DETECTOR(S)	INSTRUMENT FIELD OF VIEW	LINEAR RESOLUTION (at Nadir & Nominal Altitude)	SATELLITE	APPLICATION
10.	Temperature Humidity InfraRed Radiometer (THIR)	1)10.5-12.5µ 2) 6.5-7.0µ	Thermistor Bolometers	0.40 deg 1.20 deg	4 nmi 12 nmi	NIMBUS IV	Cloud cover mapping Storm Tracking Surf. Temp Cloud top heights Jet stream & Vertical motion
11.	ITOS High Resolution Radiometer (scanning)	1)10.5-12.5µ 2) 0.52-0.73µ	Thermistor Bolometers Silicon Cell	0.30 deg 0.16 deg	3.7 nmi 2 nmi	TIROS M ITOS A,B,C	Cloud cover mapping Storm Tracking Surf. temp. Cloud top heights Albedo
12.	ITOS Vertical Temp. Profile Radiometer (VTPR)	8 Channels: 6 in 15µ CO_2 Band 1 in rot. H_2O Band 1 in 11µ window	Thermistor Bolometer (Filter wheel in front of one detector)	2 deg	25 nmi	ITOS (ESSAs, 1970s)	Vertical Temp Profile

TABLE A-4. SUMMARY OF RADIOMETRIC INSTRUMENTS FOR REMOTE PROBING OF THE TROPOSPHERE
(CONT'D) AND STRATOSPHERE FROM SATELLITES IN MEDIUM ALTITUDE ORBIT

NUMBER	RADIOMETRIC INSTRUMENT	CHANNELS	DETECTOR(S)	INSTRUMENT FIELD OF VIEW	LINEAR RESOLUTION (at Nadir & Nominal Altitude)	SATELLITE	APPLICATION
13.	ITOS Very High Resolution Radiometer VHRR (Scanning)	1) 10.5-12.5μ 2) 0.6-0.7μ	Hg Cd Te 2 Stage Radiatively cooled to 80° K Photodiode	0.034 deg	0.4 nmi	ITOS (ESSAs, 1970s)	Cloud cover mapping Storm tracking Surf. temp. Cloud top heights Albedo
14.	Very High Radiometer for Synchronous Altitude (scanning)	1) 10.5-12.5μ	Hg Cd Te Cryogenically cooled to 80° K	0.023 deg	8 nmi	ATS (planning only)	Cloud cover mapping Storm Development tracking Surf. Temp. Cloud top heights Upper level winds
15.	High resolution InfraRed Radiation Sounder (HIRS) (Scanning)	6 channels: 4 in 15μ CO$_2$ Band 1 in 6.3μ H$_2$O Band 1 in 11μ window	5 element array photoconductive Radiatively Cooled to 80° K	0.46 deg	5 nmi	NIMBUS VI(F) (planning only)	Vertical Profiles thru broken clouds (Temp,H$_2$O) Surf. Temp.

operating either at geosynchronous (ATS) or medium (NIMBUS F) altitude orbits. The characteristics of these 15 instruments indicate the following two trends during the first decade of remote probing of the lower atmosphere from meteorological satellites: (1) an exclusive emphasis on the development of radiometric instruments in the infrared, and (2) an evolution process toward improved spectral and spatial resolutions. The improved spectral resolutions yield temperature and water vapor vertical profiles through the troposphere, including the surface values for cloudless conditions; while the simultaneous use of high spectral and spatial resolutions (i.e., HIRS) will allow the determination of the complete temperature and water vapor vertical profiles over a large area under broken cloud conditions.

9. The Global Atmospheric Research and World Weather Watch Program

A brief outline of the international Global Atmospheric Research and World Weather Watch Programs (GARP and WWW, respectively) is necessary in order to gain a complete perspective of the planned activities for the next decade concerning efforts for the prediction of the global variations of atmospheric parameters mainly within the troposphere.

The GARP program is essentially the international RDT&E phase for an eventual operational WWW in a global scale. The GARP program was proposed in 1967 jointly by relevant committees of the International Council of Scientific Unions (ICSU) and the World Meteorological Organization (WMO) of the United Nations. The main objective of GARP is to provide research and development efforts directed toward an experiment that will measure the large scale motions of the entire lower atmosphere for a limited period of time (Refs. 11, 39, 40). This plan set 1972 as the year for intensive observations on a global scale,* and outlines problems such as relevant scientific areas (e.g., energy transfer-motions of the tropical troposphere, interactions at the earth's surface, the dynamics of the boundary layer, etc.) as well as new methods of observation and data handling. Since the ICSU has no

---

*Current estimates indicate now that 1975-1976 is a more realistic date for such effort.

resources to fund such a program, the tempo of activities in GARP will be set by voluntary efforts within the world community. Besides the theoretical efforts concerning the conceptual design of an RDT&E global system (Ref. 11), some major experiments compatible with GARP are as follows: (a) the RDT&E meteorological satellites such as the NIMBUS and ATS series described above; (b) the U.S. GHOST (Global Horizontal Sounding Technique) project, which has demonstrated the capability for constant-density balloons to fly in the stratosphere for average periods of six months;* and (c) the French EOLE balloon project, which will utilize a satellite for the interrogation of balloons.

The World Weather Watch program was approved in 1967 by the World Meteorological Organization (a specialized agency of the United Nations). The main objective of the WWW program is data collection on a global scale to be processed in world and regional weather centers. The data collection would utilize conventional observing techniques, meteorological satellites, coordinated meteorological rocket soundings, telemetering ocean buoys and automatic land stations, telemetering free-flying constant density balloons, radir ndes launched from merchant ships, and other observations from commercial aircraft. The data so obtained would be handled by an augmented meteorological communications network, including geosynchronous satellites with sensor and relay sub-systems. Again, since the WMO cannot fund such programs, the tempo of activities in the WWW program will be set by the voluntary efforts of the individual Member States. The significant activities within the WWW program are: (a) a four year suggested program for 1968-1971 adopted by the Fifth World Meteorological Congress in 1967 for a Global Observing System. This program includes the use of meteorological satellites, the establishment of a large number of new upper air stations, expanded programs of observations at existing stations, an increased number of selected ships for making surface observations over the oceans, and between five and ten additional ocean weather stations (Ref. 41); (b) a plan for the addition of Regional Meteorological Centers to the World

---

*The life of the GHOST balloons in the troposphere is too short to be useful.

Centers in Melbourne, Moscow, and Washington; and (c) the role of the WWW through the following four main aspects: (1) serving as a catalytic and coordinating body in such matters as standardization of methods and hours of global observation, international coding procedures, merchant ship voluntary observing system, telecommunications systems for the international exchange of meteorological data, etc.; (2) providing direct assistance to needy countries regarding meteorological equipment and training; (3) providing the machinery for continuous planning; and (4) providing a link at the governmental level with the United Nations on such programs.

10. Conceptual Techniques for Potential Measurements from Meteorological Satellites

A potential technique for the global measurement (in near real-time) of the boundary condition involving the wind field over the oceans consists in the measuring of the thermal radiation emitted by the oceans in the microwave region of the electromagnetic spectrum. This use of passive microwave measurements would also yield the temperature and water vapor vertical profiles over oceans under cloudy conditions, which would be important to supplement the measurements by high resolution radiometers in the infrared such as HIRS (Table A-4). For these reasons, a brief review is given below of the following two topics: (1) a preliminary microwave experiment involving remote measurements from an aircraft at altitudes up to about 6 nmi of the radiation emitted by the ocean at a wavelength of 1.55 cm (Ref. 42); and (2) the feasibility of inferring temperature and water vapor vertical profiles over the oceans under cloudy conditions by passive microwave measurements from meteorological satellites at medium altitude orbits.*

---

*A contrast must now be made between sensor subsystems for the global-passive (remote) measurements from satellites and those for local-active (remote) measurements from the ground, e.g., (1) ultrasensitive radars to measure winds (Ref. 43), (2) doppler radar to measure atmospheric motions in virtually all scales (Ref. 43), (3) LIDAR (Light Detection and Ranging) to map aerosol distributions (Refs. 44,45), etc.

The microwave experiment from the aircraft is planned to demonstrate the feasibility of such measurement from the NIMBUS E meteorological RDT&E satellite (Refs. 15, 42). It utilizes an electrically scanning radiometer that consists of the following three elements. A phased-array antenna accepts radiation in a beam about 2.8 deg wide. The beam electrically scans in a direction perpendicular to the aircraft's flight direction and through an angle ± 50 deg from nadir. A receiver measures the detected radiation with an accuracy corresponding to about ± 1°C of the equivalent brightness temperature. Associated calibration and recording equipment are used. Since the spectral intensity of the radiation emitted at 1.55 cm is proportional to the brightness temperature (i.e., the product of the emissivity and temperature of the water surface), the radiometer was calibrated with reference to the radiation source with a known brightness temperature. In addition to the microwave radiometer, the experiment utilized an MRIR radiometer in the 10.5 to 11.5μ spectral range to measure the equivalent blackbody temperature of the sea surface. Wind speeds over the ocean surface were obtained from aircraft drift measurements and estimates of the wave heights. Some results of pertinent interest from these experiments are shown in Fig. A-10, where the brightness temperature is plotted as a function of the angle from nadir for smooth (i.e., negligible wind of less than 3 m/sec) and rough (i.e., a wind speed of about 15 m/sec) sea surface conditions. This figure also shows similar theoretical results as derived by Stogryon (Ref. 46). The experimental results show a higher brightness temperature (by about 20 deg) for the rough sea condition regardless of the angle from nadir in the vertical plane of observation, a result that stems from the increase in the emissivity from (a) an increase in the roughness scale (i.e., foam, spray, white caps, and heavy swells), and (b) a decrease in the water temperature of the rough relative to the smooth surface. The theoretical lines in Fig. A-10 indicate good agreement with the experimental data only for the smooth sea condition, a result that is a consequence of the rather poor understanding of the relationship between the roughness scale and emissivity. This effect of sea surface roughness on the brightness temperature of microwave
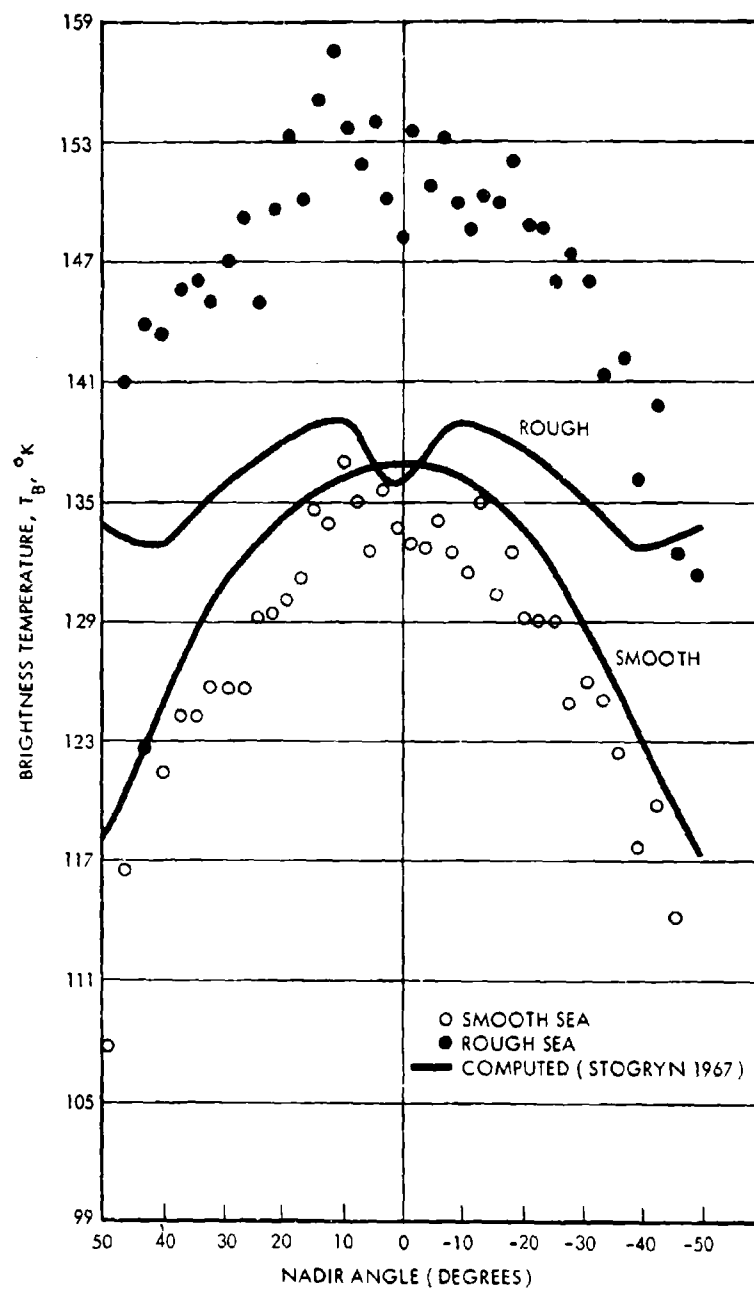
FIGURE A-10. Sea Surface Brightness Temperature as a Function of the NADIR
Angle from Aircraft (at about 5000 ft altitude) and the Roughness
of the Sea Surface (Ref. 42)

emission was also verified by the HRIR radiometer, which measured
higher radiances for the rough sea surface relative to those for the
smooth sea surface. These results then indicate that measurements of
microwave radiation emitted at 1.55 cm can be interpreted in terms of
sea surface roughness. Since the roughness scale of the sea surface
is intimately related to the prevailing winds, these results indicate
that a worldwide mapping of the sea state from meteorological satel-
lites can yield the global wind field over the oceans.*

The inversion of temperature and water vapor profiles from
measurements of emitted radiation in the microwave region of the
electromagnetic spectrum depends on two factors: (1) the brightness
temperature of the earth's surface, and (2) the transparency of the
atmosphere (Ref. 15). Atmospheric emissions in the microwave spectrum
(e.g., the weak resonance of water vapor at 1.35 cm wavelength, and
the strong complex of oxygen resonances at 0.5 cm) can be measured with
microwave radiometers, which yield the received radiance in terms of
the brightness temperature (e.g., Fig. A-10). A microwave radiometer
looking down at the surface of the earth can, therefore, distinguish
between atmospheric and surface emissions only when the brightness
temperature of the surface is low (i.e., over the water, where the
emissivity is low) relative to the atmospheric temperature. The trans-
parence of the atmosphere allows then inversion of temperature profiles
in the nearly opaque regions of the spectrum (in a manner exactly
analogous to that in the infrared spectral region), and of water vapor
profiles in the nearly transparent regions in some circumstances. Since
microwave measurements from meteorological satellites could be used to
infer temperature profiles below clouds, microwave techniques offer the
potential to yield global wind fields over the oceans and complete
temperature profiles over the major water fraction of the earth's
surface.

---

*Scanning microwave measurements from meteorological satellites at
medium altitude orbit would be made at wavelengths longer than 3 cm to
minimize the effect of cloud interference, provided, of course, that
the effect of roughness on the brightness temperature (i.e., Fig.
A-10) persists at these wavelengths.

11. Concluding Remarks

A review of the RDT&E activities over nearly the last decade concerning satellite measurements of atmospheric parameters indicates that, in general, the use of meteorological satellites operating in medium altitude (e.g., 400 to 750 nmi) and geosynchronous (19,300 nmi) orbits can provide remote measurements with adequate accuracy in a global and near real-time scales of the atmospheric parameters that are required for the numerical, long-range prediction (maximum of about 3 to 5 weeks) of the global atmospheric circulation within mainly the troposphere (up to about 7 to 10 nmi).

Some specific results concerning the satellite measurement of atmospheric parameters are as follows:

1. Radiance measurements in the infrared region of the electromagnetic spectrum from meteorological satellites operating in medium altitude orbit can determine the geopotential height and vertical temperature profile to within 60 meters and 3°K, respectively, in an altitude range up to about 10 mb, or approximately 16.5 nmi (Figs. A-1, A-4). The advent of high-spatial-resolution scanning radiometers (e.g., HIRS) would provide even higher accuracies in the geopotential height and vertical temperature distribution (Fig. A-4) over most of the globe. These results are based on (a) the use of updated statistical data for the geopotential height and temperature in the troposphere and lower stratosphere, and (b) the solution of the inversion problem to deduce the temperature profile from radiance measurements in different spectral bands (Fig. A-2) through the use of an iterative method that utilizes statistical atmospheric temperature profiles.

2. The main emphasis in the RDT&E of sensor subsystems for meteorological satellites over nearly the last decade and for the near future (Tables A-1, A-2, A-4) has been toward the development of high-spatial-resolution scanning radiometers; i.e., sensor subsystems that would yield accurate determination of the geopotential height and vertical temperature

distributions to sea level altitude over most of the globe (Fig. A-4).

3. Radiance measurements in the infrared region of the electromagnetic spectrum from meteorological satellites operating in medium altitude orbit can also yield the vertical temperature profile through the troposphere (Fig. A-7).

4. Potential techniques for measuring the velocity vector of the air motion or wind within troposphere in a global and near real-time scales are as follows: (1) microwave measurements from meteorological satellites operating at medium altitude orbit of the thermal radiation emitted by the oceans to provide data of brightness temperature as a function of the sea surface condition (Fig. A-10), which is controlled by the magnitude of the wind over the sea surface; (2) the use of meteorological satellites in geosynchronous altitude (e.g., ATS-I and ATS-III satellites provided with a spin-scan camera subsystem as indicated in Table A-2) to provide data on the motion of cloud elements over fixed geographical locations. A correlation of the motion of certain cloud elements with wind measurements would yield the wind vector in cloudy areas; and (3) the tracking of a worldwide network of constant density balloons from meteorological satellites would yield the wind vector over geographical areas and atmospheric levels without clouds.

REFERENCES

1. E. H. Lorenz, "Three Approaches to Atmospheric Predictability", 49th Annual Meeting of the American Meteorological Society, January 20-23, 1969, New York, New York.

2. J. Smagorinsky, Wexler Memorial Lecture, 49th Annual Meeting of the American Meteorological Society, January 20-23, 1969, New York, N. Y.

3. Economic Benefits from Oceanographic Research, Committee on Oceanography, Publication 1228, National Academy of Sciences, National Research Council, Washington D. C., 1964.

4. Philip D. Thompson, Numerical Weather Analysis and Prediction, The MacMillan Company, New York.

5. C. E. Leith, "Numerical Simulation of the Earth's Atmosphere" Lawrence Radiation Laboratory, University of California, Livermore, California.

6. Akio Arakawa, "Computational Design for Long-Term Numerical Integration of the Equations of Fluid Motion", Journal of Computational Physics, Vol. 1, No. 1, 1966.

7. Yale Mintz, "Very Long-Term Global Integration of the Primitive Equations of Atmospheric Motion", University of California, Los Angeles. World Meteorological Organization Technical Note No. 66, WMO-No 162, TP 79, 1965.

8. Henry Hidalgo, "Ablation of Glassy Materials Around Blunt Bodies of Revolution", Journal of the American Rocket Society, 30 March 1961.

9. Adriane Pallone, "Non-similar Solutions of Laminar Hypersonic Boundary Layers", AVCO, Wilmington, Mass. Personal Communication, 1960.

10. H. C. Willett and F. Sanders, "Descriptive Meteorology", Academic Press Inc., New York, N. Y., 1959.

11. Report by COSPAR Working Group VI, London 9-15 October, 1968. Members of this group are as follows: W. Böhme (GDR), R. Frith (UK), K. Gambo (Japan), R. Garcia (JOC), I. Haupt (FRG), D.S. Johnson (USA), E. Knighting (UK), Y. Mintz (USA), F. Möller (FRG), P. Morel (France), W. Nordberg (USA), S. Ruttenberg (USA), K. Sekihara (Japan), V. Suomi (USA), M.G. Tarakanov (WMO), M. Tepper (USA).

12. W.L. Smith, "Statistical Estimation of the Atmosphere's Pressure - Height Distribution From Satellite Radiation Measurements", IUGG/WMO Symposium on Radiation, Including Satellite Techniques, Bergen, Norway 22-28 August 1968. ESSA National Environmental Satellite Center, Washington, D.C.

13. A.M. Obukhov, "The Statistical Orthogonal Expansion of Empirical Functions" Izvestiya, Seriya Geofizicheskaya, Akademiya Nauk, SSSR No. 3, 432-439 (1960). (English translation by the American Geophysical Union, 288-291, November 1960).

14. I. Holmström, "On a Method for Parametric Representation of the State of the Atmosphere", Tellus, 15, 127-149 (1963).

15. J.C. Gille, "Inversion of Radiometric Measurements", Bulletin of the American Meteorological Society, Vol. 49, No. 9, September 1968.

16. D.Q. Wark and H.E. Fleming, "Indirect Measurements of Atmospheric Temperature Profiles from Satellites", Monthly Weather Review 94, 351-362.

17. A.W. McCulloch and W.L. Smith, "Proposal for a High Resolution Temperature Sounder for Nimbus F", January 1969, Goddard Space Flight Center, Greenbelt, Maryland.

18. M.T. Chahine, "Determination of the Temperature Profile in an Atmosphere from its Outgoing Radiation". Submitted for publication in the Journal of the Optical Society of America, December 1968.

19. J.I.F. King, "Meteorological Inferences from Satellite Radiometry", Journal of the Atmospheric Sciences, Vol. 20, No. 4, July 1963.

20. J.I.F. King, "Inversion by Slabs of Varying Thickness", Journal of the Atmospheric Sciences, Vol. 21, No. 3, May 1964.

21. L.D. Kaplan, "Inference of Atmospheric Structure from Remote Radiation Measurements", Journal of the Optical Society of America, Vol. 49, No. 10, October 1959.

22. G. Yamamoto, "Numerical Method of Estimating the Stratospheric Temperature Distribution from Satellite Measurements in the CO_2 Band", Journal of Meteorology, Vol. 18, No. 5, October 1961.

23. C.D. Rodgers, "Satellite Infrared Radiometer; A Discussion of Inversion Methods, University of Oxford Clarendon Laboratory Memorandum No. 66.13, 1966.

24. W.L. Smith, "On the Statistical Estimation of the Atmosphere's Pressure - Height Distribution from Satellite Radiation Measurements", ESSA Technical Report NESC-48 National Environmental Satellite Center, Washington, D.C., February 1969.

25. B.J. Conrath, "On the Estimation of Relative Humidity Profiles from Medium Resolution Infrared Spectra Obtained from a Satellite", NASA Report X-622-68-225, Goddard Space Flight Center, June 1968.

26. D.Q. Wark, F. Saiedy, and D.G. James, "Indirect Measurements of Atmospheric Temperatures Profiles from Satellites: VI High-Altitude Balloon Testing", Monthly Weather Review, Vol. 95, No. 7, July 1967.

27. F.B. House, E.T. Florance, R. Harrison and J.I.F. King, "Meteorological Inferences from Radiance Measurements", GCA Technical Report GCA-TR-68-18-G, GCA Corporation, Bedford, Massachusetts, September 1968.

28. L.W. Chaney, S.R. Drayson, and C. Young, "Fourier Transform Spectrometer - Radiative Measurements and Temperature Inversion", Applied Optics, 6, 1967.

29. W.L. Smith, "An Improved Method for Calculating Tropospheric Temperature and Moisture from Satellite Radiometer Measurements", Monthly Weather Review, 96, 1968.

30. V.E. Suomi and T.H. Vonder.Haar,"Geosynchronous Meteorological Satellite", AIAA Paper No. 68-1094, AIAA 5th Annual Meeting and Technical Display, Philadelphia, Pa., October 21-24, 1968.

31. R.M. Rados, "Atmospheric Measurements from Satellites", AIAA Paper No. 69-158, AIAA 7th Aerospace Sciences Meeting, New York, N.Y., January 20-22, 1969.

32. W.R. Bandeen, "Experimental Approaches to Remote Atmospheric Probing in the Infrared from Satellites", NASA TM X-63188, May 1968.

33. W. Nordberg, "Development of Meteorological Satellites in the United States", NASA TMX-63313, August 1968.

34. S. Fritz, "Pictures from Meteorological Satellites and Their Interpretation", Space Science Review 3 (1964).

35. E. Raschke, P. Musa, "The Global Radiation Balance of the Earth·- Atmosphere System Obtained from Radiation Data of the Meteorological Satellite NIMBUS II", Space Research VIII, North Holland Publishing Company, Amsterdam.

36. G. Warnecke, A. W. McCulloch, "Stratospheric Temperature Patterns Derived from NIMBUS II Measurements", Space Research VIII, North Holland Publishing Company, Amsterdam.

37. William L. Exner, Spin-Scan Camera Systems, 3 May 1969, Space Systems, Division Hughes Aircraft Company, Los Angeles.

38. J. Goldhammer, et. al. "Relay Satellites-Space-Craft Systems", Institute for Defense Analyses Research Paper P-421, July 1968, Arlington, Virginia.

39. G. D. Robinson, "Some Current Projects for Global Meteorological Observation and Experiment", Quarterly Journal of the Royal Meteorological Society, Vol. 93, No. 398, October, 1967.

40. T. F. Malone, "New Dimensions of International Cooperation in Weather Analysis and Prediciton", Bulletin of the American Meteorological Society, Vol. 49, No. 12, December 1968.

41. O. M. Ashford, "Status of the World Weather Watch Plan", Symposium on Meteorological Observations and Instrumentation of the American Meteorological Society", February 10-14, 1969, Washington, D. C.

42. W. Nordberg, J. Conaway and P. Thaddeus, "Microwave Observations of Sea State from Aircraft", Submitted for Publication to Quarterly Journal of the Royal Meteorological Society. Goddard Space Flight Center, Greenbelt, Maryland.

43. David Atlas, "An Overview of Remote Probing Techniques", 49th Annual Meeting of the American Meteorological Society, January 20-23, 1969. New York, N.Y., Department of the Geophysical Sciences, The University of Chicago, Chicago, Illinois.

44. J. A. Reagan, "Lidar Probing of the Atmosphere", 49th Annual Meeting of the American Meteorological Society, January 20-23, 1969, New York, N.Y. Engineering Experiment Station, College of Engineering, The University of Arizona, Tucson, Arizona.

45. R. M. Schotland, "Some Aspects of Remote Atmospheric Sensing by Laser Radar", 49th Annual Meeting of the American Meteorological Society, January 20-23, 1969, New York, N.Y. Contribution No. 62 of the Geophysical Sciences Laboratory, Department of Meteorology and Oceanography, New York University, New York, N.Y.

46. A. Stogryn, "The Apparent Temperature of the Sea State at Microwave Frequencies", IEEE Transactions on Antennas and Propagation, AP-15, No. 2, 1967.

DOCUMENT CONTROL DATA - R & D

(Security classification of title, body of abstract and indexing annotation must be entered when the overall report is classified)

1. ORIGINATING ACTIVITY (Corporate author)	2a. REPORT SECURITY CLASSIFICATION
Institute for Defense Analyses	FOR OFFICIAL USE ONLY
	2b. GROUP --

3. REPORT TITLE Determination of Winds and Other Atmospheric Parameters by Satellite Techniques   Volume III: Techniques for Determining Winds and Other Atmospheric Parameters

4. DESCRIPTIVE NOTES (Type of report and inclusive dates)
Study S-341 - December 1969

5. AUTHOR(S) (First name, middle initial, last name)

Alan J. Grobecker, Henry Hidalgo, John A. Laurmann

6. REPORT DATE	7a. TOTAL NO. OF PAGES	7b. NO. OF REFS
December 1969	175	46

8a. CONTRACT OR GRANT NO	9a. ORIGINATOR'S REPORT NUMBER(S)
DAHC15 67 C C011	
b. PROJECT NO	S-341
Task T-58	9b. OTHER REPORT NO(S) (Any other numbers that may be assigned this report) None

10. DISTRIBUTION STATEMENT

None

11. SUPPLEMENTARY NOTES	12. SPONSORING MILITARY ACTIVITY
None	Advanced Research Projects Agency Washington, D.C.

13. ABSTRACT

Techniques which have potential use for explicit determination of atmospheric parameters by observations from satellites are evaluated for inherent accuracy of measurement. The discussion describes the instrumental techniques for measuring densities of air and its constituents by atmospheric emission, atmospheric absorption of solar radiation, deceleration of low altitude satellites, occultation satellite-to-satellite microwave transmissions, backscatter by dust of pulsed laser signals and wind by the motion of clouds determined by time-sequenced pictures from satellites and the displacement of balloons tracked in position by satellites. The principle of operation, uncertainty of measurement, coverage in volume, and status of development of each of the techniques considered are detailed.
In addition to the methods for explicit measurement of atmospheric parameters, and implicit method of determining winds at all altitudes by machine computation of the equations of continuity of momentum, mass and energy, using satellite derived inputs of densities, temperature and heating, is suggested. Experience in application of the method for purposes of numerical prediction of weather for more than a day ahead is described. Special problems in extrapolating the experience in tropospheric simulation for the determination of winds of the upper atmosphere, for which input data are potentially available by measurements from satellites, are named. Estimates are given indicating that the upper atmosphere simulation is within the expected capacity of next-generation computers such as ILLIAC IV.

KEY WORDS	LINK A		LINK B		LINK C	
	ROLE	WT	ROLE	WT	ROLE	WT